Co-electrolysis of Water and Carbon Dioxide by Gadolinia Doped Ceria using Electrochemical Perturbations and Differential Frequency Resolved Mass Spectrometry

Jonathan M. Witt

A dissertation

submitted in partial fulfillment of the

requirements for the degree of

Doctor of Philosophy

University of Washington

2021

Reading Committee:

Eric Stuve, Co-Chair

Stuart Adler, Co-Chair

Daniel Schwartz

Program Authorized to Offer Degree:

Chemical Engineering

University of Washington

Abstract

Co-electrolysis of Water and Carbon Dioxide by Gadolinia Doped Ceria using Electrochemical
Perturbations and Differential Frequency Resolved Mass Spectrometry

Jonathan Michael Witt

Chairs of the Supervisory Committee:
Prof. Stuart Adler
Prof. Eric Stuve
Chemical Engineering

Co-electrolysis of steam and CO_2 provides a route to producing fuel for seasonal energy storage or commodity chemicals via Fischer-Tropsch reaction from renewable energy. High temperature co-electrolysis with solid oxide electrolyzer cells (SOEC) is one of the most efficient and economically viable technological options. SOECs are not in widespread use thanks to a myriad of challenges, one of which is the development of a stable catalyst.

Ni mixed with yttria stabilized zirconia (Ni-YSZ) is the standard catalyst for co-electrolysis but faces deactivation from carbon deposition, redox cycle oxidation, poisoning, and agglomeration. Alternatives to Ni-YSZ have been explored, particularly mixed ionic and electronic conductors (MIEC) such as gadolinium doped ceria (GDC). Regardless of catalyst, there exists a lack of understanding surrounding the degree to which steam and CO_2 are simultaneously electrochemically reduced or if much of the CO_2 is reduced by the chemical reverse water gas shift reaction (RWGS).

The current toolset of electrochemical and chemical analysis tools may be insufficient to resolve the discrepancy due to the complexity of thermodynamics, geometry, flow rates, inlet gas compositions, temperature, and multiple reaction pathways available. An additional complexity is current distribution. This effect was studied using CO_2 electrolysis on MIEC 10% doped GDC (GDC10) with and without a gold porous current collecting layer. Results, complemented with COMSOL modeling, show that relying on metal meshes for current distribution risks misinterpretation of electrochemical impedance spectra.

Finally, the new tool presented here is frequency resolved mass spectrometry (FRMS). FRMS applies voltage or current perturbations to an electrode in a low vacuum environment while collecting the perturbations of the gaseous species with a mass spectrometer. FRMS has the potential to provide new insights into the relationships between current, voltage, and gas species by isolating phenomena at different timescales to be analyzed in the mass spectrum. The data presented here suggests that co-electrolysis occurs while RWGS is negligible under the conditions studied.

TABLE OF CONTENTS

LIST OF FIGURES

LIST OF TABLES

ACKNOWLEDGEMENTS

Funding was provided by NSF, CBET Program: Grant number 1509117. I would like to also thanks the CEI Fellowship which funded this research for a quarter. I would like to thank Dr. Brian Gerwe for assistance with software development of data collection software for LabView and frxas.py. I would like to thank Kameron Harmon, Facilities Manager at UW Chemical Engineering, for helping construct part of the vacuum apparatus. I would like to thank Peter Hirtle, of the UW Physics Machine Lab, for custom welding the metal piece of the vacuum reactor together.

Chapter 1. INTRODUCTION

1.1 GLOBAL MOTIVATION

This work is motivated by the risks to global human health from the warming of the land and oceans because of anthropomorphic emissions of greenhouse gases (GHG) as detailed in the most recent report of the International Panel of Climate Change (IPCC)[1]. The IPCC AR5 Synthesis Report presents these risks, such as food and water shortages, increased displacement of people, coastal flooding, and increased poverty, as a function of total global carbon emissions. The IPCC suggests keeping global temperature increases to less than 2 ºC to mitigate the worst of these risks. The global carbon budget to meet that goal is 2900 $GtCO_2$ as measured since 1870; as of 2011, 65% of this carbon budget has been used. As of 2010, the energy sector, the largest contributor, and transportation sector accounted for 35% and 14% of global GHG emissions, respectively. The work here directly contributes to efforts dedicated to mitigating these risks and GHG gas emissions, mostly within the transportation and energy sectors, via electrochemistry[1].

1.2 NATIONAL, REGIONAL, AND LOCAL MOTIVATION

As of 2019, the US energy portfolio by consumption consisted of 37% petroleum, 32% natural gas, 11% renewable, 11% coal, and 8% nuclear[2]. The transportation sector is by far the largest consumer of petroleum, making up 70% of petroleum use. It also accounts for 28% of the US carbon dioxide equivalent emissions (2018)[3]. Transportation is the largest emitter of carbon dioxide equivalents, and the largest consumer of energy in the US, yet transportation trails both the industrial (35% of energy use) and residential (12% of energy use) sectors in the measure of renewable energy penetration into their respective sectors.

Focusing locally, as of 2018 Washington State (WA) transportation accounted for 44.9% of total emissions in WA, representing a need for WA state to prioritize minimizing transportation emissions[4]. Much of that is owed to a rich abundance of hydro power, yet that is limited by geography. There exists an urgent need to curb transportation related emissions by increasing the amount of renewable energy powering the transportation sector.

The status quo answer is to electrify transportation, with some to little effort to expand the use of hydrogen powered vehicles as well. To exemplify this, within the US, the only state with much hydrogen policy, incentives, infrastructure, and regulations is California[5], however electrification efforts nationwide are dominant. The dominance can be exemplified by the vast gap between hydrogen fueling stations and electric charging stations. As of 2018, there were 39 public hydrogen fueling stations[6] in the US compared to about 47,000 public charging stations for electric vehicles in the US [7].

Decarbonization of the US electric grid is challenging without energy storage. First, electricity generation accounts for 27% of US carbon equivalent emissions, only 1% behind transportation. While it is good news that 56% of renewable energy is entering the electric power sector, natural gas peaker plants are on standby to account for the unpredictable temporal nature of wind and solar. As penetration of renewables into the market increases, more polluting fossil fuel plants must be on standby and curtail electricity to prepare for the predictable ramp in electricity demand as the sun sets[8]. Typically, this phenomenon is illustrated by the Duck Curve[9]. This curve shows a large solar penetration during the daylight and then a collapse of renewable energy into the evening hours. The steeper the collapse, the larger the ramp of electricity is needed. The intuitive alternative solution to this problem is energy storage to store excess renewable energy for times it is in deficit.

While batteries are the most common solution, power to gas is a complementary and alternative approach. Power to gas is the production of gaseous fuel, i.e. hydrogen, *via* electrolysis to be used for energy storage when supply exceeds demand. An advantage of power to gas is that it can use the existing natural gas grid to transport hydrogen, methane, or combinations of the two from electrolysis products[9]. Electrolysis products can be directly used for many sectors such as heating, fuel cell vehicles, natural gas vehicles, industrial chemical production, and electricity regeneration. Locally, the reverse of electrolyzers, fuel cells, is being explored by Microsoft to power data centers using natural gas. Fuel cells offer DC power that is needed for server racks. A pipeline and fuel cell replaces miles of expensive copper and electrical equipment necessary to appropriately preprocess and deliver electricity for the servers[10].

An alternative method for energy storage, Li-ion batteries, has the advantage of high roundtrip efficiencies of typically 83% as compared to 30% for a reversible electrolyzer.[11] Notably though, round-trip efficiencies in grid storage applications have shown battery storage systems achieving 50-55%.[8] Additionally, batteries have fixed power to energy ratios, whereas in an electrolyzer, power and energy are separated. In an electrolyzer system, more energy storage means storing more fuel in larger tanks. Storage with batteries means buying more batteries, even if more power were not needed for the application. The type of electrolyzer studied here is a solid oxide electrolyzer cell (SOEC), which offers better thermodynamics and kinetics than lower temperature electrolyzers (alkaline and polymer electrolyte membrane) due to its high temperature operation[12].

1.3 SOLID OXIDE ELECTROLYZERS

As shown in Figure 1.1, an SOEC uses electrical energy to convert oxidized species into reduced species, i.e. fuel. When operating in reverse, an SOEC becomes an SOFC that converts fuel, such as hydrogen, into electricity by oxidizing that fuel. A solid electrolyte, typically yttria stabilized zirconia (YSZ), conducts oxygen anions while blocking the flow of electrons. SOECs and SOFCs are operated at high temperature in the range of 600-900 ºC to achieve sufficient oxygen anion conductivity in the YSZ electrolyte[12–14]. The porous cathode is commonly a cermet of Ni and YSZ (Ni-YSZ). The porous anode is commonly perovskite LaSrMnO$_{3-\delta}$[15].

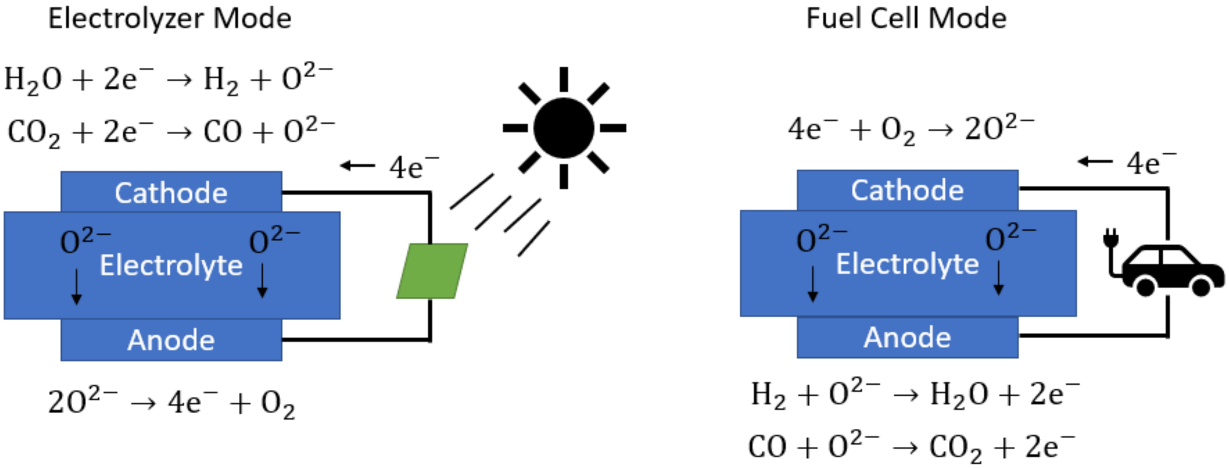

Figure 1.1. Diagram of an SOEC and SOFC.

SOECs were first demonstrated in the 1980s, particularly for NASA space exploration[16]. The motivation was to recycle CO_2 and water into fuel and oxygen. Today, the SOEC is studied from the nanoscale to the macro-scale and from the electrode to the stack level involving planar and tubular geometries. At this moment, SOECs have advanced from R&D to pilot plant operation[12]. SOECs require less voltage for the same current output as alkaline and PEM electrolyzers, but they are currently more costly per kg of H_2 produced[12].

Much has improved for SOECs over the last two decades. The degradation rate has slowed from 40%/1000 hours to 0.4%/1000 hours. Efficiencies have increased by a factor of 2.5 as well for steam electrolysis. These improvements stem from thinner electrolytes, increased active surface area, increased ceramic strength, and replacement of the oxygen electrode with mixed ionic and electronic conductors (MIEC). However, most of the degradation that still exists for an SOEC is associated with the fuel electrode and merits prioritized investment.[12]

The standard fuel electrode, Ni-YSZ, has an advantage of being earth abundant. Despite the improvement in SOEC performance with Ni-YSZ, there remain challenges[17]. Silica containing oxides leach into and deactivate active Ni sites. It is susceptible to poisoning by sulfur, carbon deposition, and unstable unit cell contraction and expansion in redox environments[13,18]. Historically, performance suffers from Ni migration, and reportedly still does[19]. Higher temperatures, which offer favorable kinetics, result in particle agglomeration[13]. There are opportunities for a more robust alternative with equally favorable kinetics to take Ni-YSZ's place.

1.4 MIXED IONIC AND ELECTRONIC CONDUCTOR: GADOLINIUM DOPED CERIA

Mixed ionic and electronic conductors simultaneously allow transport of oxygen anions and electrons. Unlike Ni-YSZ, MIECs are not limited to a triple phase boundary (TPB) where electronically conducting, ionically conducting, and gas phases meet. All of the surface area of an MIEC contains active sites. Even if an MIEC is half as active as Ni-YSZ, it could easily contain double the number of active sites. Additionally, MIECs offer more stability and tolerance to poisons like sulfur and carbon deposition as compared with Ni and other metal candidates for fuel electrodes[17,20]. Many types of MIECs have been studied including perovskites, double perovskites, Ruddlesden-popper phases, and doped ceria[17]. Gomez and Hotza provide a review of these materials as oxygen electrodes in SOFCs[17].

Among the doped ceria electrodes, gadolinium doped ceria ($Gd_xCe_{1-x}O_{2-\delta}$ or GDC) is chosen for this research. The dopant amount is represented by x and the oxygen non-stoichiometry introduced by the dopant is δ. Cerium comprises 0.0046 wt% of the Earth's crust, the most common among rare earth elements[21]. As shown in Figure 1.2, cerium is 30% more abundant than Ni, mitigating the risk of supply chain issues. In fact, ceria was first employed by Ford as an oxygen storage material for car converters[21], highlighting its historical use and well established supply chain. Gd is 6% as abundant as Ni in the earth upper continental crust[21], which does present supply chain issues. This may be mitigated by the reality that doping as little as 10% by Gd on the ceria sites may be required for good catalytic activity.

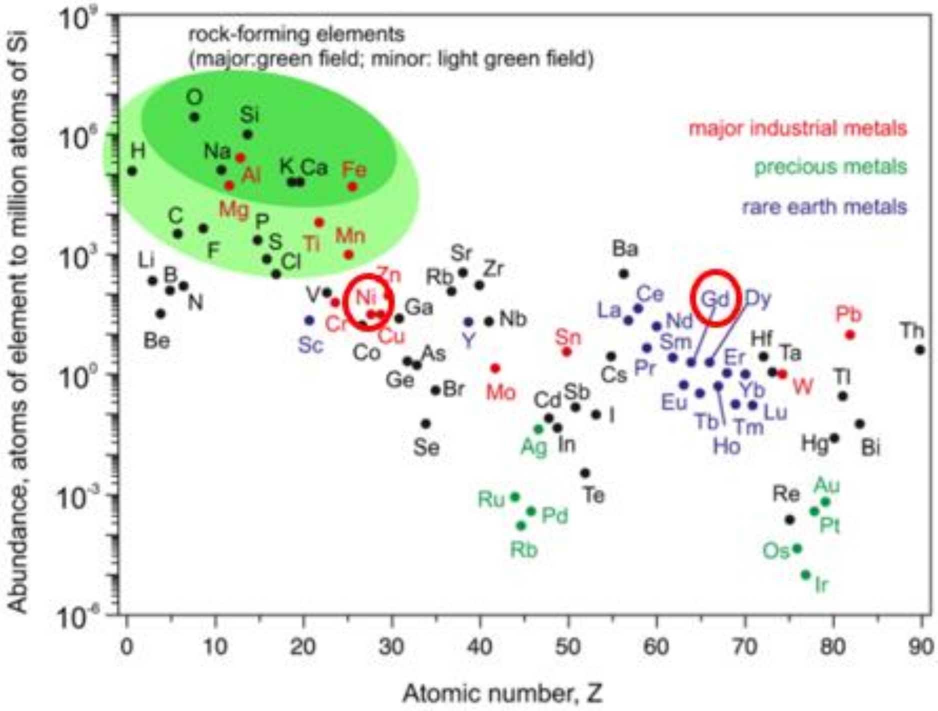

Figure 1.2. Distribution of abundance of elements in Earth's upper continental crust. Gd and Ni are circled. Adapted from source[21]

GDC has been typically studied as an electrolyte because of its high ionic conductivity, especially compared to YSZ at low temperatures such as 600 ºC[22–24]. It is often used with YSZ as a blocking layer to prevent detrimental interaction of YSZ and oxygen electrode materials[12]. CeO_2 and its doped versions have a cubic fluorite structure[25,26], which has a large tolerance for disorder, whether due to doping, reduction, or oxidation[24]. At least up to 20 mole % doping $(CeO_2)_{0.8}(LnO_{1.5})_{0.2}$ (Ln = rate earth oxide) does not change the diffraction pattern between doped ceria and non-doped ceria[26]. The lattice structure of GDC is shown in Figure 1.3.

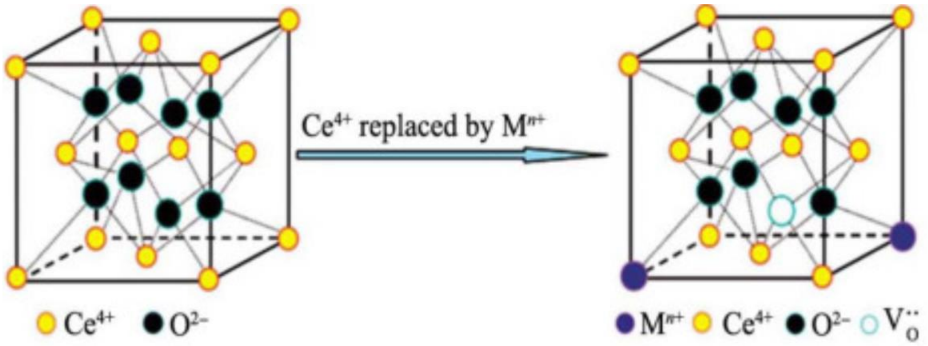

Figure 1.3. CeO_2 unit cell and transformation from doping with metal M^+. Reproduced from source[27].

Doping is a mechanism by which to introduce ionic conductivity. Insertion of Gd, with an oxidation state of III, to replace Ce(IV) introduces vacancies by expelling oxygen from their lattice sites to maintain charge neutrality[26]. Oxygen vacancies created by the dopant provide a route for O^{2-} anions to be transported through the solid. Figure 1.4 shows that oxygen non-stoichiometry (δ) also grows with the reduction of p_{O_2}. Additionally, GDC is an *n*-type conductor and thus the lower the partial pressure of oxygen, the more electrons it can conduct[28]. Figure 1.5 shows that the total electrical conductivity, the combination of electronic and ionic conductivity, of GDC10 increases as the partial pressure of oxygen (p_{O_2}) decreases at 800 ºC. Growth in δ contributes to a larger ionic conductivity, but as Figure 1.6 shows, the ionic transference number approach zero at lower p_{O_2}. The ionic and electrical conductivities are additionally a function of dopant concentration and temperature[25].

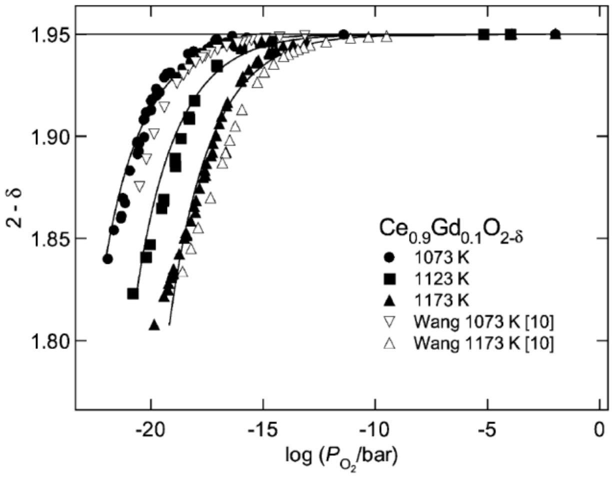

Figure 1.4. Oxygen nonstoichiometry of $Gd_{0.1}Ce_{0.9}O_{2-\delta}$ as a function of oxygen partial pressure at temperatures of 1073, 1123, and 1173 K. Filled data and solid lines (a fit) are from Yashiro and co-workers[29], and open symbols are from Wang and co-workers[30]. Reproduced from source[29]

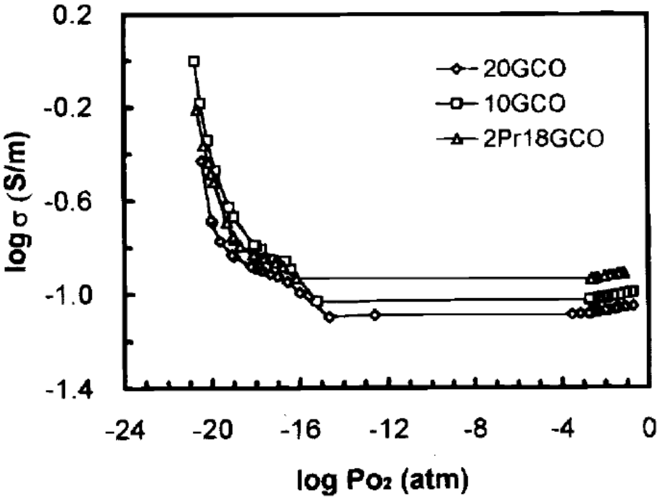

Figure 1.5. Total electrical conductivity of GDC10 (squares), GDC20 (diamonds), and 2Pr18GDC as a function of oxygen partial pressure at 1073 K. Reproduced from source[28].

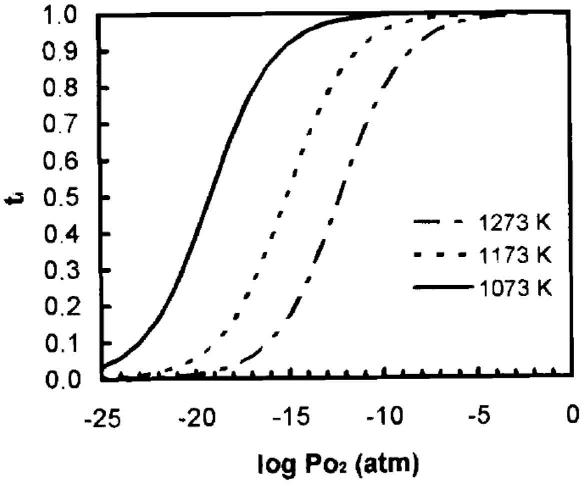

Figure 1.6. Ionic transport number for GDC10 at temperatures of 1273, 1173, and 1073 K. Reproduced from source[28].

Samarium and gadolinium are good candidates for dissolving in ceria because their ionic radii closely match that of Ce(IV). While Sm and Gd both have an oxidation state of (III)[21,26], Sm has a slightly larger ionic conductivity. Among doped ceria, samarium doped ceria (SDC) and GDC are more likely to be electrocatalytically active. $CeO_{2-\delta}$ can decompose to multiple phases after the O molar fraction decreases to 0.67[21]. The solubility limit of oxides with similar cationic radius as Ce(IV) is typically 15-25% of substitution[21]. Given that SDC and GDC are both good candidates, GDC is studied here because of its previous use within the research group. Uncertainty in phase transformations is minimized by using 10% Gd doped ceria (GDC10).

1.5 EQUILIBRIUM POTENTIALS

The equilibrium potential of an oxygen sensor is determined by the Nernst equation,

$$E = \frac{RT}{nF} \ln\left(\frac{P_{O_{2\mathrm{I}}}}{P_{O_{2\mathrm{II}}}}\right) \tag{1.1}$$

Where $E = E_I - E_{II}$ is the potential difference of the sensor, E_I is the potential at electrode I, E_{II} is the potential at electrode II, R is the gas constant, T is temperature, n is moles of electrons per mole of O_2, *F* is Faraday's constant, $P_{O_{2_I}}$ is oxygen partial pressure electrode I, and $P_{O_{2_{II}}}$ is the oxygen partial pressure at electrode II. In an oxygen sensor, which is used in the present work, the gas composition at one electrode is usually air, while that of the other is the gas composition of interest. In practice, the partial pressure of oxygen on the air electrode is known, the temperature is controlled, and the open circuit voltage (OCV) is measured; then the partial pressure of oxygen is determined for the other electrode.

If performing water or carbon dioxide electrolysis, this measurement helps determine the ratio of hydrogen to water entering, within, or exiting a reactor, depending on the position of the oxygen sensor. The Nernst potential for water electrolysis is

$$E = \frac{RT}{nF}\ln\left(\frac{P_{O_2}^{I}}{\left[\exp\left(-\frac{\Delta G^{o}}{RT}\right)\left(\frac{p_{H_2O}}{p_{H_2}}\right)\right]^2}\right) \tag{1.2}$$

where ΔG^o is the Gibbs free energy of formation of water at temperature *T* and unit activity of all species, $p_{O_{2_I}}$ is the oxygen partial pressure at the anode, p_{H_2O} is water partial pressure at the cathode, and p_{H_2} is hydrogen partial pressure at the cathode. Similarly, for the electrolysis of CO_2, the Nernst equation is

$$E = \frac{RT}{nF}\ln\left(\frac{P_{O_2}^{I}}{\left[\exp\left(-\frac{\Delta G^{o}}{RT}\right)\left(\frac{p_{CO_2}}{p_{CO}}\right)\right]^2}\right) \tag{1.3}$$

where ΔG^o is the Gibbs free energy of formation of water at temperature *T* and unit activity of all species, $p_{O_{2_I}}$ is the oxygen partial pressure at the anode, p_{CO_2} is CO_2 partial pressure at the cathode, and p_{CO} is CO partial pressure at the cathode.

1.5.1 *Characteristics of CO_2 Electrolysis, H_2O Electrolysis, and RWGS*

Figure 1.1 shows an electrochemical cell undergoing co-electrolysis of water and CO_2. Additionally, the reverse water gas shift (RWGS) contributes to the cell performance. Co-electrolysis, written below in Kröger-Vink notation, involves one bulk vacancy ($V_{\ddot{O}}$) and two electrons (e') per reaction, and consumes oxygen in water or CO_2 to produce two occupied oxygen sites (O_O^x)

$$\mathrm{H_2O + 2e' + V_{\ddot{O}} \rightarrow O_O^x} \tag{1.4}$$

$$\mathrm{CO_2 + 2e' + V_{\ddot{O}} \rightarrow O_O^x} \tag{1.5}$$

The RWGS reaction involves the consumption of hydrogen and carbon dioxide to produce water and carbon monoxide.

$$\mathrm{CO_2 + H_2 \rightleftarrows H_2O + CO} \tag{1.6}$$

Figure 1.7 shows the thermodynamics of co-electrolysis and RWGS along with associated voltages. The interception of the Gibbs free energies of CO_2 electrolysis and RWGS is indicated with a line at 827 ºC. All the work presented in this dissertation is at 800 ºC.

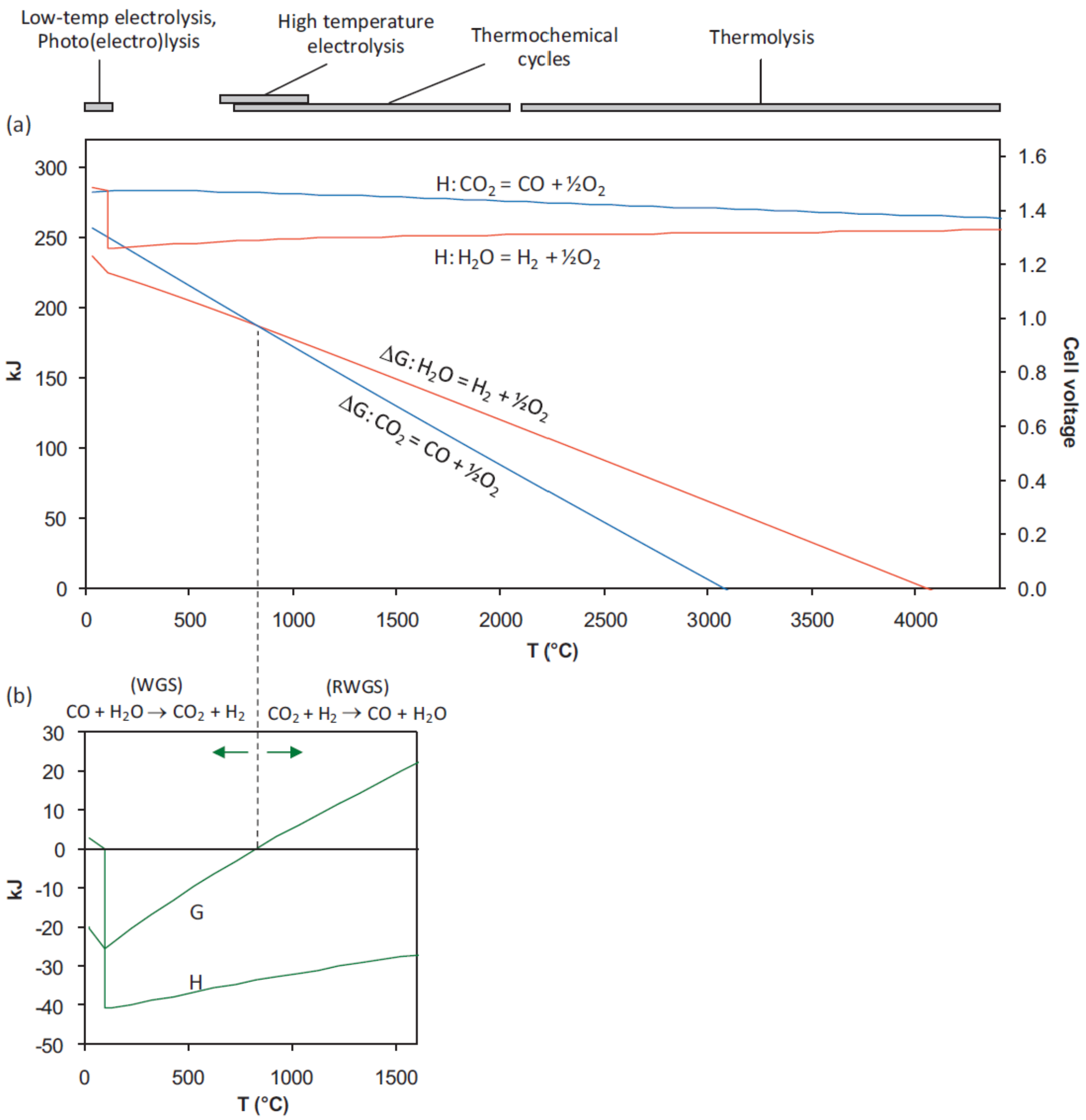

Figure 1.7. (a) The free energies and enthalpies of CO_2 and H_2O reduction as a function of temperature. Calculated values from FactSage 5.5 software. Cell voltage is shown on the right. The dotted line shows that, at 827 ºC, the reactions are equally favorable. Methods of accomplishing these reactions are labeled at the top of the figure. (b) Shows RWGS and WGS thermodynamics. Reproduced from source[13]

.

The RWGS reaction is known to reach a kinetically fast equilibrium above 800 ºC in the presence of Ni catalysts[31]. Water electrolysis is known to be more favorable than CO_2 electrolysis in SOEC as indicated by its lower area specific resistance (ASR)[32–35] compared to that of CO_2 electrolysis. Similarly, at 800 ºC, H_2 oxidation is found to be 2.5 times faster than CO oxidation in fuel cells[36]. The rate of RWGS is commonly expressed in the gas phase as[36]

$$R_{\mathrm{RWGS}} = k_{\mathrm{sf}}\left(p_{\mathrm{H_2O}}p_{\mathrm{CO}} - \frac{p_{\mathrm{H_2}}p_{\mathrm{CO_2}}}{K_{\mathrm{ps}}}\right) \tag{1.7}$$

$$k_{\mathrm{sf}} = 0.0171\exp\left(-\frac{103191}{RT}\right)\ (\mathrm{mol\ m^{-3}\ Pa^{-2}\ s^{-1}}) \tag{1.8}$$

$$K_{\mathrm{ps}} = \exp(-0.2935Z^3 + 0.6351Z^2 + 4.1788Z + 0.3169) \tag{1.9}$$

$$Z = \frac{1000}{T(K)} - 1 \tag{1.10}$$

1.6 ELECTROCHEMICAL IMPEDANCE SPECTROSCOPY

Electrochemical impedance spectroscopy (EIS) is a common technique used to characterize electrochemical performance. The technique consists of measuring the first order impedance of a cell as a function of applied frequency at a specific voltage or current perturbation amplitude. The impedance is a complex function and is found *via* the ratio of the complex voltage to the current. EIS is often conducted with small enough voltages, such as 10 mV (root mean square), to maintain the assumption of linearity while probing a cell. This technique allows for the isolation of rate-determining phenomena that occur at times scales of 1/frequency.

Figure 1.8 shows a typical EIS set-up for SOFC and SOEC button cells. A cell is perturbed at a specific voltage and frequency for some number of waveforms, and the responding current is measured. After a sweep of frequency, the impedance can be plotted on a Nyquist plot. The electrolyte resistance is usually associated with the high frequency intercept (the intercept closest to the origin). The difference between the high frequency and low frequency intercept, for one arc features, is often associated with the rate limiting phenomena’s characteristic resistance for that electrode. The peak frequency is related to the time constant for the rate limiting phenomena. If modeled as an RC circuit, that peak frequency is related to the characteristic resistance and capacitance *via*

$$f_{peak} = \frac{1}{2\pi R_c C} \tag{1.11}$$

The shape of the Nyquist plot gives an indication of the rate limiting phenomena at those time constants. If a 45-degree angle is present at high frequency, then the cell is often considered co-limited by mass transport and kinetics. This shape is a Gerischer-impedance. However, if the shape is only semi-circular, then the electrode is kinetically limited. If the shape is a depressed semi-circle or Gerischer shape, that is an indication of a distribution of relaxation time constants within the cell. This can be caused by non-uniformity of geometric parameters like thickness or thermodynamic properties within the material.

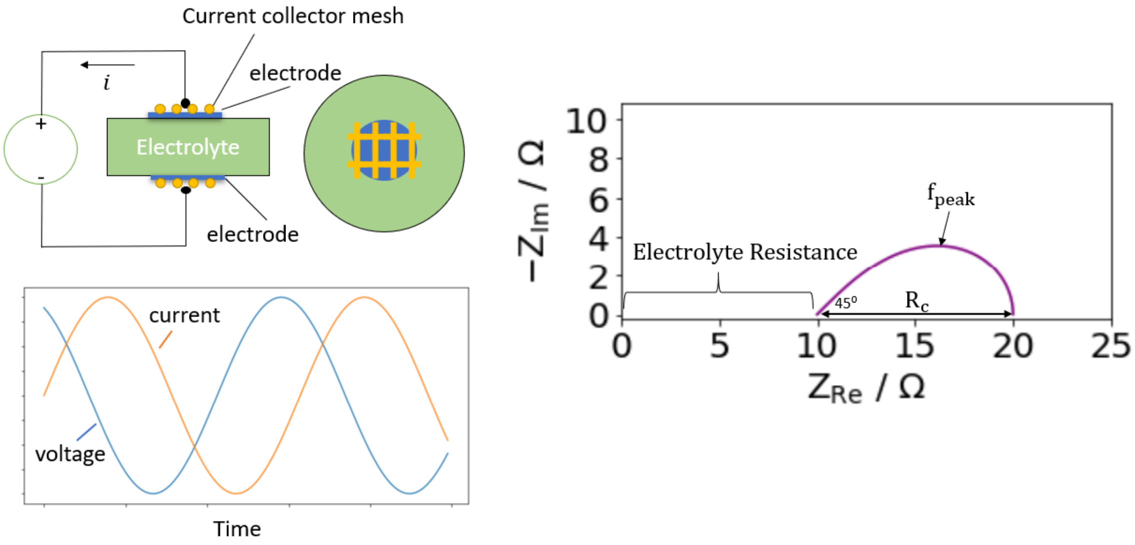

Figure 1.8. Diagram of a typical EIS button cell measurement. Shown are voltage and current time perturbations and a resulting Nyquist plot with a Gerischer-impedance indicative of co-limitations from kinetics and transport. Key features like the characteristic resistance (R_C), peak frequency (f_{peak}), and electrolyte resistance are noted.

The downside of EIS is that it linearizes the responses and thus eliminates the non-linear, or higher order, thermodynamics and kinetics associated with the electrochemical process. Higher order harmonics can offer distinguishing responses for otherwise linearized thermodynamics and rate laws. These higher order harmonics can be obtained and analyzed using non-linear EIS, however that topic is outside of the scope of this dissertation. It is common to use EIS as a complementary technique with other methods of characterization, such as gas chromatography or mass spectrometry with co-electrolysis studies in SOEC.

1.7 MASS SPECTROMETRY

Mass spectrometry is a method in which the gas composition of a flow or chamber is determined by measuring the ratio of the mass-to-electric (m/e) charge of a molecule or atom. Mass spectra are measured within a chamber of total pressure less than 1×10^{-4} Torr. Molecules are ionized, focused, fed through a mass separator such as a quadrupole, and then detected as current in either a Faraday cup or electron multiplier. Quadrupoles separate masses by focusing the ionized gas flow through the center of a set of four metal poles. Two poles are positive and opposite from one another. The other two (negative) poles are opposite to each other and displaced 90º relative to the positive poles. DC and AC voltages are used at different frequencies to allow only certain mass to charge ratios to pass through to the detector. The magnitude of the current at the detector is related to the partial pressure of that species in the vacuum chamber.

All species create a fragmentation pattern when they are ionized. The fragmentation patterns of species of interest to this present work are shown in Appendix A of Chapter 3, which includes H_2O, O_2, N_2, Ar, H_2, CO_2, and CO. These fragmentation patterns are well known and predictable. The relative sizes of the peaks in the fragmentation patterns are used to calculate the gas compositions. Nearly every vacuum system will have detectable amounts of H_2, water, CO, and CO_2. The presence of nitrogen, argon, or oxygen often indicates a leak into the system.

When using fragmentation patterns to do quantitative analysis, it is assumed that the total mass spectrum is a linear combination of all the species of the mixture being analyzed. The height (h_{Mg}) of a specific mass peak (M) for one species (g) is related to the partial pressure by the fragmentation factor (α_{Mg}) and the RGA pressure sensitivity factor for gas g (S_g $[\frac{\mathrm{amp}}{\mathrm{Torr}}]$),

$$h_{Mg} = \alpha_{Mg} S_g P_g \qquad (1.12)$$

For strict quantitative analysis, the sensitivity factor and fragmentation patterns should be determined for pure gases under operating conditions expected for experiments. Both can change based on operating parameters, such as emission current and mass filter settings. Regarding accuracy, the slower the scan speed, the better signal to noise ratio is achieved for quantitative analysis. Scans can also be averaged to increase signal to noise ratio[37].

1.8 VACUUM FLOW

A vacuum system consists of a vacuum pump, vacuum chamber, and pipes that connect the chamber to the pump. The mean free path (λ) between molecular collisions of gases is a function of the gas density (n) and the diameter of the molecule (d_o),

$$\lambda = \frac{1}{2^{\frac{1}{2}} \pi d_o^2 n} \qquad (1.13)$$

For example, at 760 Torr, the mean free path of air at 22 °C is 6.5×10^{-8} m, whereas at 0.75 Torr, it is 6.6×10^{-5} m. The Knudsen number is defined as the ratio of λ to a characteristic dimension of the system (d),

$$Kn = \frac{\lambda}{d} \qquad (1.14)$$

If *Kn* > 1, then the flow is considered molecular flow and is governed by gas to wall collisions. If *Kn* < 0.01 and the Reynolds number is less than 1200, then the flow is viscous flow for which gas to gas collisions dominate. The Reynolds number is defined as

$$Re = \frac{U\rho d}{\eta} \tag{1.15}$$

where U is gas velocity, ρ is mass density, and η is the viscosity. If the *Kn* number is between 1 and 0.01, then the flow is neither viscous nor molecular and is otherwise not well understood[38].

Chapter 2. EFFECTS OF CELL GEOMETRY ON CURRENT COLLECTION IN IMPEDANCE MEASUREMENTS OF SOLID-STATE ELECTRODES

2.1 BACKGROUND

Electrolysis and co-electrolysis of CO_2 and H_2O using renewable electricity to produce hydrogen and carbon monoxide (synthesis gas) for fuel and plastics production has been of considerable interest due to the rise in global emission from fossil fuels[13,39–43]. Mixed ionic and electronic conductors, which have greater active surface area than ionically conductive electrolytes, have been investigated for their use in high temperature solid oxide fuel cells and electrolyzers[44–46]. Among the MIECs, doped ceria has been widely characterized and used[29,47–51].

Electrochemical impedance spectroscopy is often used to characterize the electrochemical performance of MIECs, including doped ceria. Typically, MIECs are studied as anodes and cathodes on button cells with a reference electrode of platinum painted at the center of the cell. Workers associate the high frequency intercept often with the electrolyte resistance. The difference between the high and low frequency intercepts is associated with the electrode resistance. The peak frequency and peak resistance are associated with the electrode reaction kinetics. The shape of the Nyquist plot is associated with either a kinetically limited response (semi-circular) or a co-limited response of mass transport and kinetics (Gerischer shaped).

Recently, it has been shown that these interpretations can be convoluted by sheet resistance, the resistance to lateral charge distribution along a planar electrode, because of a poor current collector. Boukamp et al. found that electrode sheet resistance has an unexpected non-linear dependence on thickness of dense $La_{0.6}Sr_{0.4}Co_{0.2}Fe_{0.8}O_{3-\delta}$ (LSCF6428) thin film electrodes. They associated this effect with geometric and electrochemical parameters: electrode thickness, density of contact points of their current collector mesh, electrode conductivity[52]. Boukamp et al. later developed a relation using layer thickness, current collector mesh grid size, electronic sheet resistance and surface exchange to determine whether sheet resistance of the electrode can be ignored[53].

In 2010, Ciucci et al. developed a 2-D, small bias model for the flux of electronic and ionic species in $Sm_{0.15}Ce_{0.85}O_{1.925-\delta}$ with patterned, interconnected metal as current collectors. Using finite element analysis (FEM), they concluded that the surface exchange reaction was rate limiting rather than the sheet resistance. They showed that the pitch between metal interconnects and the ratio of the metal interconnect width to pitch affected measured area specific electrode resistance.

This work contributes a frequency dependent 3D FEM simulation and 2D analytical solution regarding the contributions of geometric parameters (electrolyte thickness, current collector pitch, electrode thickness) and electrochemical parameters (electrode electronic conductivity and electrolyte ionic conductivity) to the measured high frequency intercept, low frequency intercept, peak frequency, and Nyquist plot shape. The analysis indicates under what experimental conditions it is safe to ignore the effects of sheet resistance.

2.2 THEORY

2.2.1 *3D Model*

Figure 2.1 shows the modeled 3D symmetrical slice of the electrochemical cell. The electrode is approximated as a 2D domain, assuming instantaneous equilibrium in the z dimension, with thickness b. A gold wire mesh grid with pitch $2p$ rests on top of the electrode. The wires are approximated as one-dimensional line contacts. Below the electrode is the electrolyte of thickness L, which is modeled as a 3D domain. Below the electrolyte is a negligibly thin counter electrode. The electrode-electrolyte interface is labeled as Γ_1. A wire frame diagram of the modeled slice shows the other interfaces labeled as Γ_i.

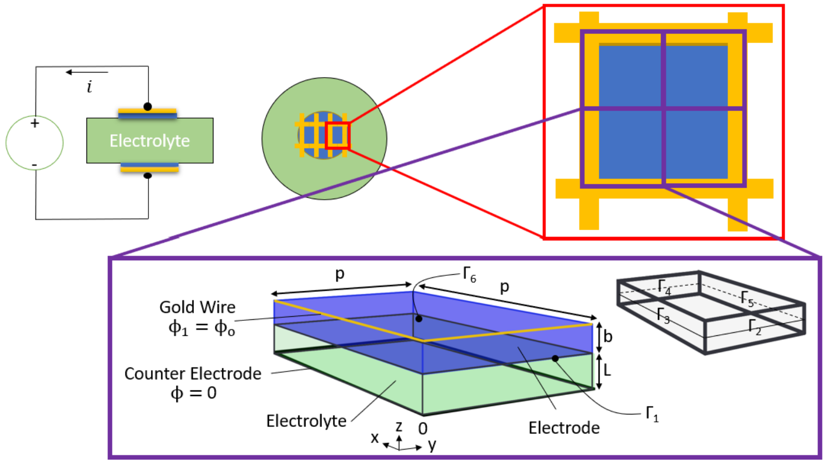

Figure 2.1. Schematic of the 3D modeled section of cell used in COMSOL.

The surface exchange reaction at Γ_6 is modeled as a resistor and capacitor in parallel (i.e., an RC element). The RC element simulates a kinetically limited electrode. The current through Γ_6 is

$$i_{\Gamma_6} = \left(\frac{1}{R_{\mathrm{elc}}} + C_{\mathrm{elc}}\frac{\partial}{\partial t}\right)(\phi_1 - \phi) \tag{2.1}$$

where R_{elc} is the area specific electrode resistance in the absence of sheet resistance, C_{elc} is area specific capacitance in the absence of sheet resistance, t is time, ϕ_1 is potential in the electrode, ϕ is potential in the electrolyte, and the electrode domain is abbreviated as elc. The current through the electrode faces of Γ_3 and Γ_2 is

$$i_{\Gamma_{3,\mathrm{elc}},\Gamma_{2,\mathrm{elc}}} = \sigma_{\mathrm{e}} b\left(\frac{\partial^2\phi_1}{\partial x^2} + \frac{\partial^2\phi_1}{\partial y^2}\right) \tag{2.2}$$

where σ_{e} is the electrode electronic conductivity. The current through interface Γ_1 is

$$i_{\Gamma_1} = -\sigma_i \left(\frac{\partial\phi}{\partial z}\right)\Big|_{z=\Gamma_1} \tag{2.3}$$

where σ_i is the ionic conductivity of the electrolyte. Charge is conserved, therefore the current flux through all these interfaces must be equal

$$i_{\Gamma_1} = i_{\Gamma_{3,\mathrm{elc}},\Gamma_{2,\mathrm{elc}}} = i_{\Gamma_6} \tag{2.4}$$

Laplace's equation governs potential in the electrolyte,

$$\nabla^2\phi = 0 \tag{2.5}$$

2.2.2 *3D Model Boundary Conditions*

The boundary conditions for the 3D model are

$$\phi_1|_{\Gamma_{3,\mathrm{elc}},\Gamma_{2,\mathrm{elc}}} = \phi_\mathrm{o} \tag{2.6}$$

$$\frac{\partial\phi_1}{\partial x}|_{\Gamma_2,\Gamma_4} = \frac{\partial\phi_1}{\partial y}|_{\Gamma_3,\Gamma_5} = \frac{\partial\phi}{\partial x}|_{\Gamma_2,\Gamma_4} = \frac{\partial\phi}{\partial y}|_{\Gamma_3,\Gamma_5} = 0 \tag{2.7}$$

$$\phi|_{\mathrm{z}=0} = 0 \tag{2.8}$$

Due to symmetry, the current flux at all sides is zero. The potential at the wires, $\Gamma_{3,\mathrm{elc}}$ and $\Gamma_{2,\mathrm{elc},}$ is the applied potential ϕ_o. The potential at the counter electrode is zero because this is taken as reference in a two-point electrochemical measurement without a reference electrode.

2.2.3 *3D FEM Implementation in COMSOL*

In COMSOL it is difficult to simulate a 2D domain. Instead, an anisotropic 3D domain with an arbitrary thickness δp, where δ is some fraction of p, is suitable for visualization of the 2D profile. In this case,

$$\sigma_\mathrm{e} b = \sigma_\mathrm{e}^\mathrm{eff}\delta p \tag{2.9}$$

$$\sigma_\mathrm{e}^\mathrm{eff} = \frac{\sigma_\mathrm{e} b}{\delta p} \tag{2.10}$$

where the σ_e^{eff} of Eqn. 2.10 is for a single direction. The *z* direction is artificially made orders of magnitude more conductive by multiplying *z*-axis current flux by a large number (κ):

$$\sigma_{\mathrm{e}}^{\mathrm{eff}} = \frac{\sigma_{\mathrm{e}} b}{\delta p} \begin{Bmatrix} 1 & 0 & 0 \\ 0 & 1 & 0 \\ 0 & 0 & \kappa \end{Bmatrix} \tag{2.11}$$

The governing equation and boundary conditions are non-dimensionalized with the terms found in Table 2.1, which are given in more detail in Appendix C. A notable difference between the COMSOL simulation and 2D model is that the COMSOL simulation was completed with α and γ normalized to R_{elc} rather than to the resistance of the low frequency intercept, herein called α_{elc} and γ_{elc}. Heat flux was analogously used as current flux. The steady state, scaled, and non-dimensionalized current density flux and boundary conditions in each domain and the electrode-electrolyte interface are

$$N_{\mathrm{ely}} = -\frac{\epsilon}{\gamma_{\mathrm{elc}}} \nabla^2 \bar{\psi} \tag{2.12}$$

$$N_{\mathrm{elc}} = \nabla \bar{\psi}_1 \begin{Bmatrix} -\frac{1}{\alpha_{\mathrm{elc}} \delta} & 0 & 0 \\ 0 & -\frac{1}{\alpha_{\mathrm{elc}} \delta} & 0 \\ 0 & 0 & -\frac{\kappa}{\alpha_{\mathrm{elc}} \delta} \end{Bmatrix} \tag{2.13}$$

$$N_{\Gamma_1} = (1 + j\sigma)(\bar{\psi}_1 - \bar{\psi}) \tag{2.14}$$

$$\bar{\psi}_1|_{\xi=0} = 1 \tag{2.15}$$

$$\bar{\psi}|_{\zeta=0} = 0 \tag{2.16}$$

All other sides are insulating. Figure 2.2 shows these boundary conditions mapped onto a 3D modeled section.

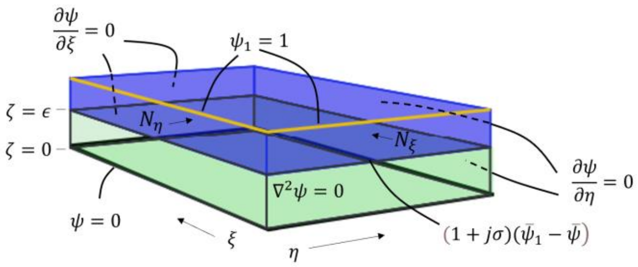

Figure 2.2. Schematic of the 3D model with non-dimensionalized current fluxes, dimensions, and boundary conditions.

2.2.4 *2D Model*

Figure 2.3 shows the geometry used for the 2D model. In this case, the depth of the symmetrical slab in Figure 2.3 is arbitrary.

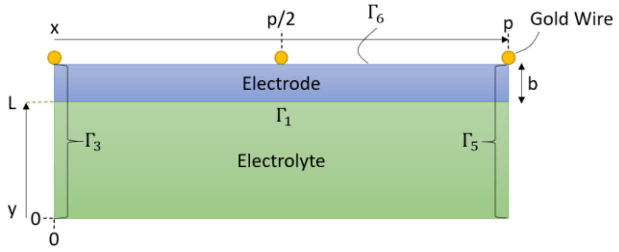

Figure 2.3. Schematic of the 2D model

The governing equations are all the same with fewer interfaces and dimensions to consider. Eqns. 2.2-2.3 become

$$i_{\Gamma_3,\mathrm{elc}} = \sigma_\mathrm{e} b \left(\frac{\partial\phi_1^2}{\partial x^2}\right) \tag{2.17}$$

$$i_{\Gamma_1} = -\sigma_\mathrm{i} \left(\frac{\partial\phi}{\partial y}\right) |_{y=L} \tag{2.18}$$

Thus, Eqn. 2.4 changes to

$$i_{\Gamma_1} = i_{\Gamma_{3,elc}} = i_{\Gamma_6} \tag{2.19}$$

and the boundary conditions become

$$\phi_1|_{x=0} = \phi_\mathrm{o} \tag{2.20}$$

$$\frac{\partial\phi_i}{\partial x}|_{x=0,\ \ x=\frac{p}{2},\ \ x=p} = 0 \tag{2.21}$$

$$-\sigma_i\left(\frac{\partial\phi}{\partial y}\right)|_{y=L} = \sigma_e b\left(\frac{\partial\phi_1^2}{\partial x^2}\right) \tag{2.22}$$

$$\phi|_{y=0} = 0 \tag{2.23}$$

An extra wire at *p*/2 is added in the 2D model to match the length of wires in the 3D model. As a result, the 3D and 2D models share the same area specific scaling at low and high asymptotic limits of sheet resistance. Figure 2.4 displays these asymptotic limits. With no sheet resistance, the current flux is uniform throughout the area and thus area specific resistance scales as p^2. At high sheet resistance the current flux is concentrated at the wires and thus the impedance scales as $2p$ (two wire lengths).

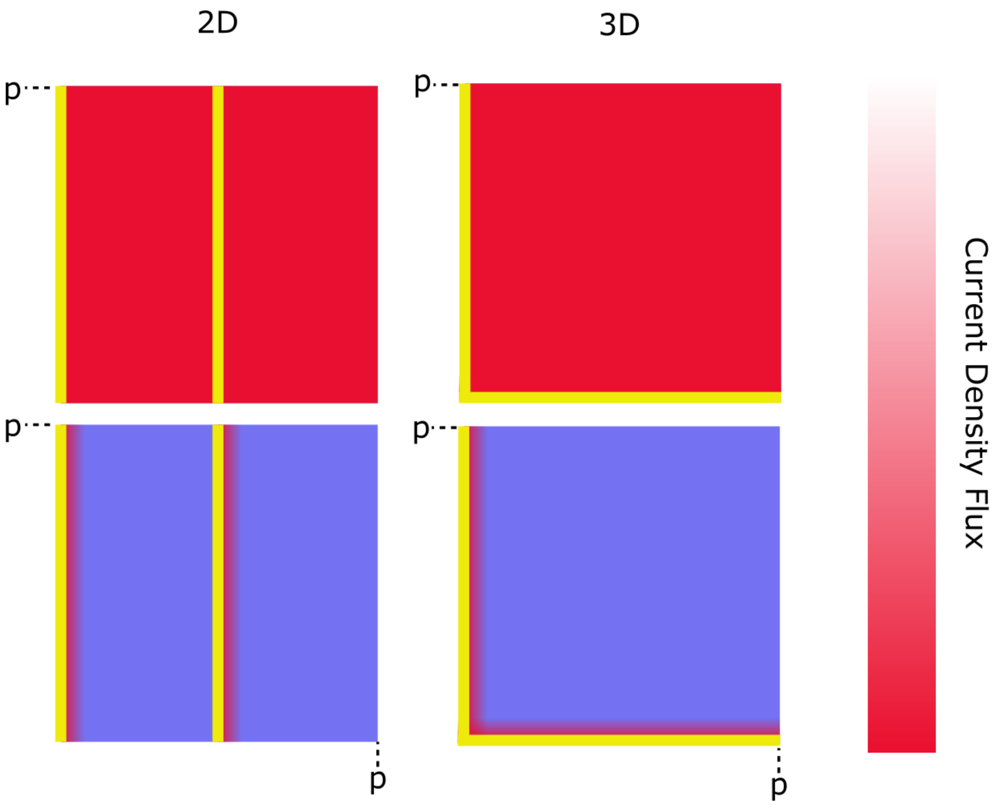

Figure 2.4 Relationship of active area carrying current flux, the red gradient, as a function of sheet resistance. At high sheet resistance (bottom), the active area scales with the gold wire length, while at low sheet resistance (top), the active area used scales with the geometric area.

2.2.5 *Non-dimensionalized 2D model*

The 2D model can be non-dimensionalized using the relationships found in Table 2.1. The ordinary differential equation and partial differential equation are stripped of time dependence and become

$$\frac{\partial^2 \bar{\psi}_1}{\partial \xi^2} = \frac{\alpha(1+j\sigma)}{(1-\gamma)}\left(\bar{\psi}_1 - \bar{\psi}|_{\eta=0}\right) = \frac{\epsilon}{\beta}\left(\frac{\partial \bar{\psi}}{\partial \eta}\right)|_{\eta=0} \tag{2.24}$$

$$\nabla^2 \bar{\psi} = 0 \tag{2.25}$$

The boundary conditions are transformed into the following

$$\frac{\partial\bar{\psi}}{\partial\xi}\Big|_{\xi=0,\frac{1}{2},1}=0 \tag{2.26}$$

$$\bar{\psi}|_{\eta=\epsilon}=0 \tag{2.27}$$

$$\frac{\alpha(1+j\sigma)}{(1-\gamma)}\left(\bar{\psi}_1-\bar{\psi}|_{\eta=0}\right)=\frac{\epsilon}{\beta}\left(\frac{\partial\bar{\psi}}{\partial\eta}\right)\Big|_{\eta=0} \tag{2.28}$$

While the derivation is explained in Appendix A, it is useful to explain the significance of the scaling and non-dimensionalization. Variable α is the ratio of area specific sheet resistance to the area specific low frequency intercept in the absence of sheet resistance ($R_{\mathrm{LF}}^{\mathrm{o}}$). Variable γ is the ratio of area specific electrolyte resistance to $R_{\mathrm{LF}}^{\mathrm{o}}$. β is the ratio of area specific electrolyte resistance to area specific sheet resistance. These three parameters capture the counteracting effects of changing geometric or electrochemical parameters of the current collector mesh, electrode, and electrolyte.

Figure 2.5 maps the scaled geometry and boundary conditions.

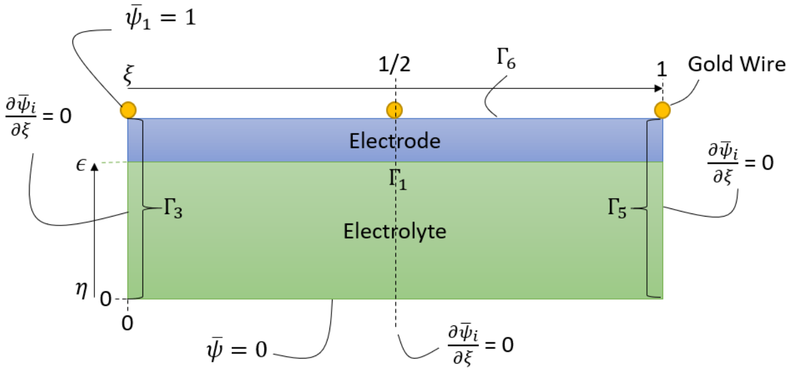

Figure 2.5. Schematic of the 2D geometry with non-dimensionalized boundary conditions.

Once the expressions for potential are solved as shown in Appendix A, *Z*, the frequency dependent impedance, is scaled to $R_{\mathrm{LF}}^{\mathrm{o}}$. This ratio is called *H*, which is found by integrating the current density ($\bar{\iota}$) over either interface $\Gamma_{3,\mathrm{elc}}$, Γ_1, or the counter electrode, followed by

$$H = \frac{Z}{R_{\mathrm{LF}}^{\mathrm{o}}} = \frac{\phi_{\mathrm{o}}}{\bar{\imath} R_{\mathrm{LF}}^{\mathrm{o}}} \tag{2.29}$$

Ultimately, the 2D analytical solution is

$$H = \frac{1}{c_{\mathrm{o}}}\left[\frac{\alpha}{2\sqrt{a}\sinh\left(\frac{\sqrt{a}}{2}\right)}\right] \tag{2.30}$$

$$a = \frac{\alpha}{1-\gamma}(1 + j\sigma) \tag{2.31}$$

$$\frac{1}{c_o} = \cosh\left(\frac{\sqrt{a}}{2}\right) + 2\beta\sqrt{a}\sinh\left(\frac{\sqrt{a}}{2}\right) + \sum_{n=1}^{N} \frac{-a\frac{\tanh(\lambda_n \epsilon)}{\left(\lambda_n^2 + a\right)^2} 4\sqrt{a}\sinh\left(\frac{\sqrt{a}}{2}\right)}{\frac{\tanh(\lambda_n \epsilon)\lambda_n^2}{\lambda_n^2 + a} + \frac{\lambda_n \epsilon}{a\beta}} \tag{2.32}$$

The eigenvalues for the summation are

$$\lambda_n = 2\pi n \tag{2.33}$$

After a sensitivity analysis, an *N* of at least 150 eigenvalues is recommended. The analytical solution can be numerically estimated in a solver such as Python, MATLAB, etc.

Table 2.1. Overview of the non-dimensional parameters

Symbol	Equation	Description
ψ	$\frac{\phi}{\phi_{\mathrm{o}}}$	Non-dimensional potential in electrolyte
ψ_1	$\frac{\phi_1}{\phi_{\mathrm{o}}}$	Non-dimensional potential in electrode
ζ	$\frac{z}{L}$	Scaled *z* coordinate
ξ	$\frac{x}{p}$	Scaled *x* coordinate
η	$\frac{y}{p}$	Scaled *y* coordinate

ϵ	$\frac{L}{p}$	Ratio of characteristic lengths
α	$\frac{p^2}{R_{\mathrm{LF}}^{\mathrm{o}}\sigma_{\mathrm{e}}b}$	Ratio of sheet resistance to low frequency intercept in the absence of sheet resistance.
γ	$\frac{L}{R_{\mathrm{LF}}^{\mathrm{o}}\sigma_{\mathrm{i}}}$	Ratio of electrolyte resistance to the low frequency intercept in the absence of sheet resistance.
τ	$\frac{t}{R_{\mathrm{elc}}C_{\mathrm{elc}}}$	Scaled Time
σ	$\omega R_{\mathrm{elc}}C_{\mathrm{elc}}$	Scaled Angular Frequency
N	$\frac{iR_{\mathrm{LF}}^{\mathrm{o}}}{\phi_{\mathrm{o}}}$	Scaled current density
g	$\frac{(1-\gamma)}{\gamma\epsilon}\tanh(\epsilon)$	Counter Scaling γ
β	$\frac{\gamma}{\alpha}$	Ratio of electrolyte resistance to sheet resistance.

2.3 EXPERIMENTAL

2.3.1 *Experiment*

Porous $Gd_{0.10}Ce_{0.90}O_{1.95-\delta}$ (GDC10) (fuelcellmaterials.com, GDC10-TC, 6.1 m^2/g) electrodes were screen printed on both sides of cylindrical 4.31 mm thick dense 10 wt% doped yttria stabilized zirconia (YSZ10) electrolyte (Zircar Zirconia Type ZYP-30 Powder) discs to make symmetrical cells. YSZ10 discs were made by compressing two grams of YSZ10 powder at 3500 psig for 3 minutes within a stainless-steel die dedicated to YSZ10 powder. Discs were placed into an oven with stagnant air and then sintered at 1500 °C for four hours at a ramp rate of 2 °C/min.

The ink used for screen printing was a 50 wt% organic solution of alpha-terpineol (Alfa Aesar 95% min), ethyl cellulose (Aldrich Chemical Company, Inc – Ethoxy content 48%), and oleic acid (Alfa Aesar Technical Grade) and 50 wt% GDC10. To make the ink, 18.3 g of alpha-terpineol, 1.6 g of ethyl cellulose, and 0.1 g of oleic acid were stirred together for 5-6 hours, then left to sit for two to three days. An equal weight of GDC10 was then added and stirred in with the mixture. The slurry was then roll milled with a spacing of 0.152 mm. The smooth ink collected from the roll mill was then used for screen printing immediately.

After screen printing, the GDC10 electrodes underwent the following sintering protocol: 2 °C/min to 670 °C, hold 1 hour, 2 °C/min to 1151 °C hold 2 hours, then 2 °C/min to room temperature. Based on previous work, the porosity was estimated to be 50% and tortuosity 1.5[48]. SEM images based on previously made cells using the same procedure showed that the electrode thickness was approximately 4 microns. The diameters of the nominally symmetric electrodes were 6.13 mm on one side and 5.32 mm on the other.

Experiments were conducted on the same electrodes before and after using a paint brush to paint a porous current collecting layer of gold on top of the electrode. The gold layer was a mix of the organic ink mix described before and dried gold ink from fuelcellmaterials.com (AU-I). The gold ink from fuelcellmaterials originally contained a minimum of 70 wt% Au and balance terpineol, and the particle size was (D50) < 0.6 microns or APS of 0.5 microns. The ink was sintered onto the disc while it laid sideways (on curved side) within an alumina boat with two aquarium pumps blowing air into the sintering chamber. The sintering protocol was 1 ºC/min to 95 ºC, hold 2 hours, 1 ºC/min to 287 ºC, hold 4 hours, 1 ºC/min to 856 ºC, hold 2 hours, cool 2 ºC/min to room temperature.

Experiments were done inside a ProboStat™ wherein both electrodes are open to the same gas environment. A ceramic screw and nut clamp held a gold wire mesh with nominally a 0.5 mm pitch against the electrodes. The gold meshes had gold wire extensions twisted together with platinum lead wires. The ProboStat™ uses an O-ring at the base to be airtight in addition to hermetic electrical feedthroughs sealed with PETE. EIS data were taken until the they were stable for a given experimental condition. The experiments were conducted at 800 ºC with temperature maintained and monitored by K-type thermocouples encased in alumina tubes below and to the side of the cell, respectively. LabVIEW software monitored the temperature to the side of the cell using a NI 9211 four channel readout attached to the type K thermocouples. The ProboStat™ has a volume of approximately 1 L.

Partial pressures were determined by flow rates and a custom oxygen sensor. Three gas cylinders (Praxair) were used: a tank of 98.5% CO (balance N_2), a tank of pure CO_2, and a tank of pure N_2. Three mass flow controllers were used: MKS 0-10 sccm (Model# 1179A11CS1BV) flowing CO_2, MKS 0-100 sccm (Model# 1179A12CS1BV) flowing CO, and an Aalborg 0-500 sccm GFC17 flowing N_2. The MKS controllers were controlled by an MKS four channel flow controller power supply and readout (MKS Type 247) with gas correction factors set to 0.7 for CO_2 and 1.0 for CO/N_2. The flow rates of the CO/N_2 mixture and CO_2 were maintained nominally at 1.7 sccm and 1.5 sccm, respectively, with the N_2 flow rate set at 0, then 10, and then 100 sccm. The partial pressure of oxygen is determined by the ratio of CO_2 to CO and the temperature. The ratio of CO_2 to CO remained constant, and thus, the partial pressure oxygen remained constant. The electronic and ionic conductivity of GDC10 is a function of oxygen partial pressure and temperature, and therefore, both remained constant throughout the experiment[29].

An oxygen sensor made of two platinum electrodes and a YSZ10 electrolyte tube monitored the voltage between the applied gas environment and air at 700 ºC. A measured 0.88 OCV, using the Nernst equation, means that the partial pressure ratio of CO_2 to CO was 12.98. The ratio expected from the flow rates would be 0.9. However, since the concentrated CO/N_2 gas was set at 1.7 sccm, well below the recommended minimum flow of 5% of total maximum flow rate of the rated 0-100 sccm MKS MFC, any calibration and extrapolation to 1.7 sccm is unreliable. The flow rate of the CO/N_2 gas at a set point of 1.7 sccm was also unmeasurable through a 1 mL bubble flow meter pipette. This was another indication that the flow rate differed from 1.7 sccm for the CO/N_2 flow because the CO_2 flow was measurable using a bubble flow meter down to a 0.5 sccm set point on a 0-10 sccm MKS MFC. After considering the calibrated flow rates of N_2, CO_2, and the OCV of the partial oxygen sensor, the estimated $\log_{10}(p_{O_2})$ was -16.17 and the resulting experimental partial pressures are outlined in Table 2.2.

Table 2.2. Summary of experimental conditions at 800 ºC

Condition	p_{CO} (bar)	p_{CO_2}(bar)	p_{N_2}(bar)
1	0.07	0.94	0
2	0.009	0.11	0.89
3	0.002	0.03	0.98

EIS was done using a Solartron 1260 Frequency Response Analyzer and a SI 1287 Solartron Potentiostat, sweeping between 600 kHz and 10 mHz at a 10 mV RMS amplitude using Scribner ZPlot®. These were two-point measurements with no reference electrode. Within Scribner's ZPlot®, the potential was applied *vs*. reference of zero volts.

2.3.2 *Simulation Methods*

COMSOL 5.5 was used to solve the 3D model with a finite element mesh analysis using package – heat transfer in solids. Two domains, the electrode and electrolyte, were built. Overall, the solid had dimensions of (L, W, H) as (1, 1, ϵ) in the electrolyte and (1, 1, δ) in the electrode. The mesh was free tetrahedral with a maximum element size of 10% of the length and a minimum element size of 0.1% of the length. The maximum element growth rate was 1.32, the curvature factor 0.3 and the resolution of narrow regions 0.85. The interfaces of the electrode and electrolyte within Γ_3 and Γ_2 were given finer meshes of 0.1% of the solid model length after a sensitivity analysis involving the values of computation time, mesh size, κ, and δ. The sensitivity analysis was focused on mitigating error when the gradients should be the shortest, which would be at high frequency (σ = 1000), small g (0.01), and small ϵ (0.01). A κ of 316 and δ of 0.01 was shown to achieve similar error to finer meshes while also allowing the COMSOL simulations to be completed within a reasonable timeframe.

Insulation was applied to all faces but $\Gamma_{3,\mathrm{elc}}$ and $\Gamma_{2,\mathrm{elc}}$. At those two electrode faces, the potential was set to 1. At the counter electrode, the potential was set to 0. Eqns. 2.12–2.16 were entered into the Heat Transfer in Solid Equations. The COMSOL simulations were originally done in terms of a_{COMSOL} and g,

$$a_{\mathrm{COMSOL}} = \frac{\alpha}{(1-\gamma)(1+g)} \tag{2.34}$$

The equations were swept as a function of σ from 10^{-3} to 10^{3}, evenly separated in log space by 10ths, g was simulated from 10^{-1} to 10^{2}, evenly separated in log space by quarters, and a_{COMSOL} was simulated from 10^{-1} to 10^{3}, evenly separated in log space by quarters. Total current flux can be found through the interface of the electrode and electrolyte, $\Gamma_{3,\mathrm{elc}}$ and $\Gamma_{2,\mathrm{elc}}$, or counter electrode face by integrating over those surfaces. Since the normalized applied potential is 1, these double integrals resulted in a value of admittance through those interfaces. Ideally, they should all be equal. The result from the counter electrode was found to be the most numerically stable and was thus chosen as the reported results in this study. The impedance can be found from the admittance using

$$Y = \frac{1}{(Z_{\mathrm{Re}})^2 + (Z_{\mathrm{Im}})^2}(Z_{\mathrm{Re}} - jZ_{\mathrm{Im}}) \tag{2.35}$$

where Z_{Re} (or Z') is real impedance and Z_{Im} (or Z'') is imaginary impedance.

2.4 EXPERIMENTAL RESULTS

Results of CO_2 electrolysis on GDC10 at 800 ºC are shown in Figure 2.6. After adding a layer of gold porous current collector, the arcs transitioned from significantly depressed semi-circular shapes to nearly semicircular. The high frequency intercept decreases by a factor of 17.56 from 686.88 ohms to 39.1 ohms. The high frequency intercept is attributed to the electrolyte resistance, and as expected, the resistance of the electrolyte is not a function of CO_2 or CO partial pressures. Given the temperature and cell dimensions, the estimated expected electrolyte resistance is 69 ohms[14]. When the cell has a porous current collector layer, it registers the right order of magnitude of electrolyte resistance to confidently assume that nearly all the superficial area of the electrode is being used.

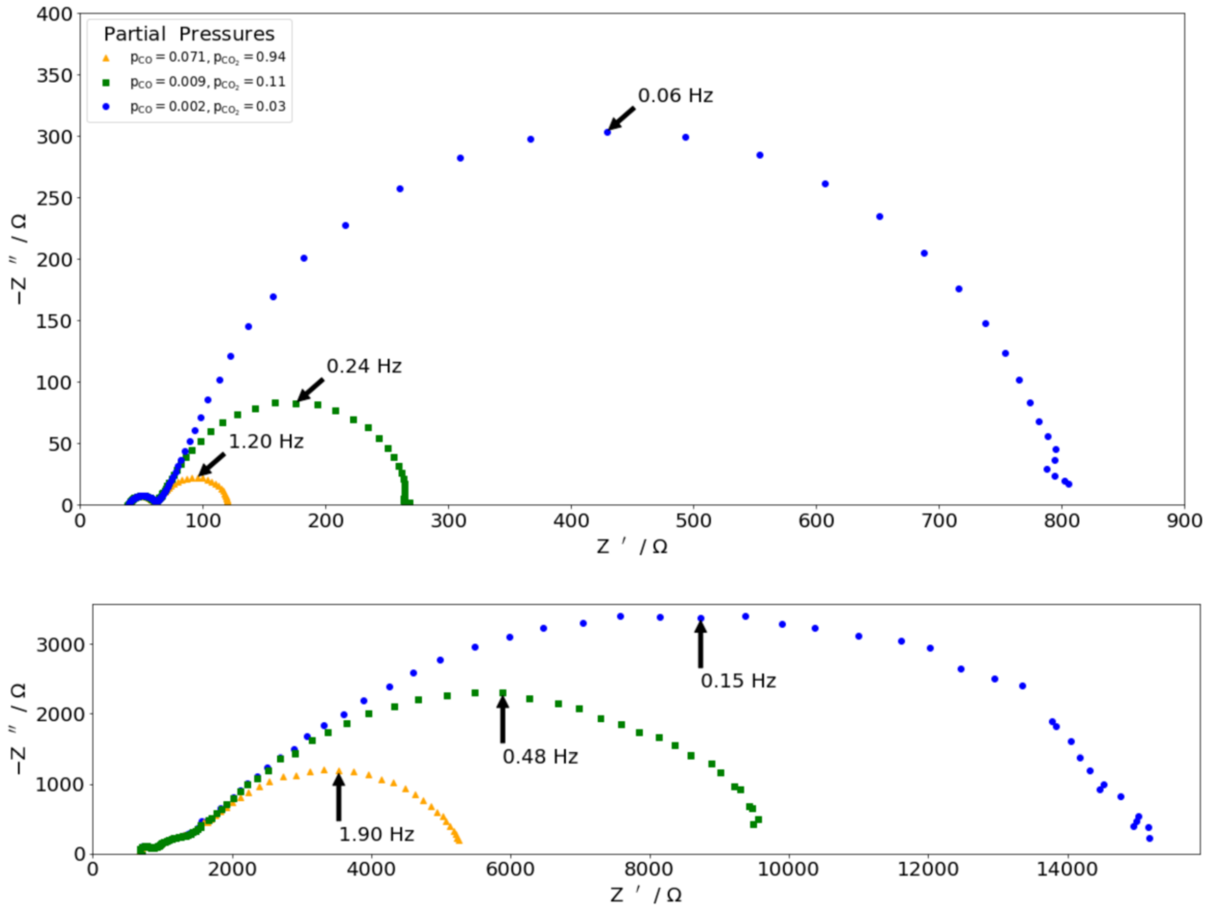

Figure 2.6. EIS results of CO$_2$ electrolysis on GDC10 electrodes at 800 ^{o}C. (bottom) is without a porous gold current collector layer and (top) is with a porous gold current collector layer.

Starting from the lowest nitrogen content to the high nitrogen content, the low frequency intercept transitions by a factor of 43.8 from 5,260 ohms to 120 ohms, a factor of 36.29 from 9,616 to 265 ohms, and a factor of 17.91 from 15,161 ohms to 846.5 ohms. The partial pressures of oxygen were kept constant by varying the amount of nitrogen flowing into the system, thus keeping the electronic conductivity of the electrode constant. As expected, with or without a porous gold current collector layer, when partial pressures of the reactants increase, the total cell resistance decreases. This is because the surface exchange reaction is faster, as indicated by the increase in peak frequency at high partial CO_2 and CO pressures.

The peak frequencies are larger without a porous current collector by a factor of 1.5 to 2.5. This is not intuitive because there should be no difference in capacitance, as electrode thickness also does not change, at any given conditions, but peak resistance appears to increase. Given that peak frequency is the reciprocal of the product of capacitance and resistance, it would be expected that the peak frequencies of the cell without a porous current collector would be smaller than that with one. However, within the COMSOL simulation, it is seen that as sheet resistance increases, the measured peak frequency also increases. This behavior is mimicked in the simulation results.

2.5 SIMULATION RESULTS

Figure 2.7 shows how the ratio of the observed high frequency (R_{HF}) and low frequency intercepts (R_{LF}) to $R^{\mathrm{o}}_{\mathrm{LF}}$ as a function of ϵ, α, and g; i.e.

$$H_{\mathrm{LF}} = \frac{R_{\mathrm{LF}}}{R^{\mathrm{o}}_{\mathrm{LF}}} \tag{2.36}$$

$$H_{\mathrm{HF}} = \frac{R_{\mathrm{HF}}}{R^{o}_{\mathrm{LF}}} \tag{2.37}$$

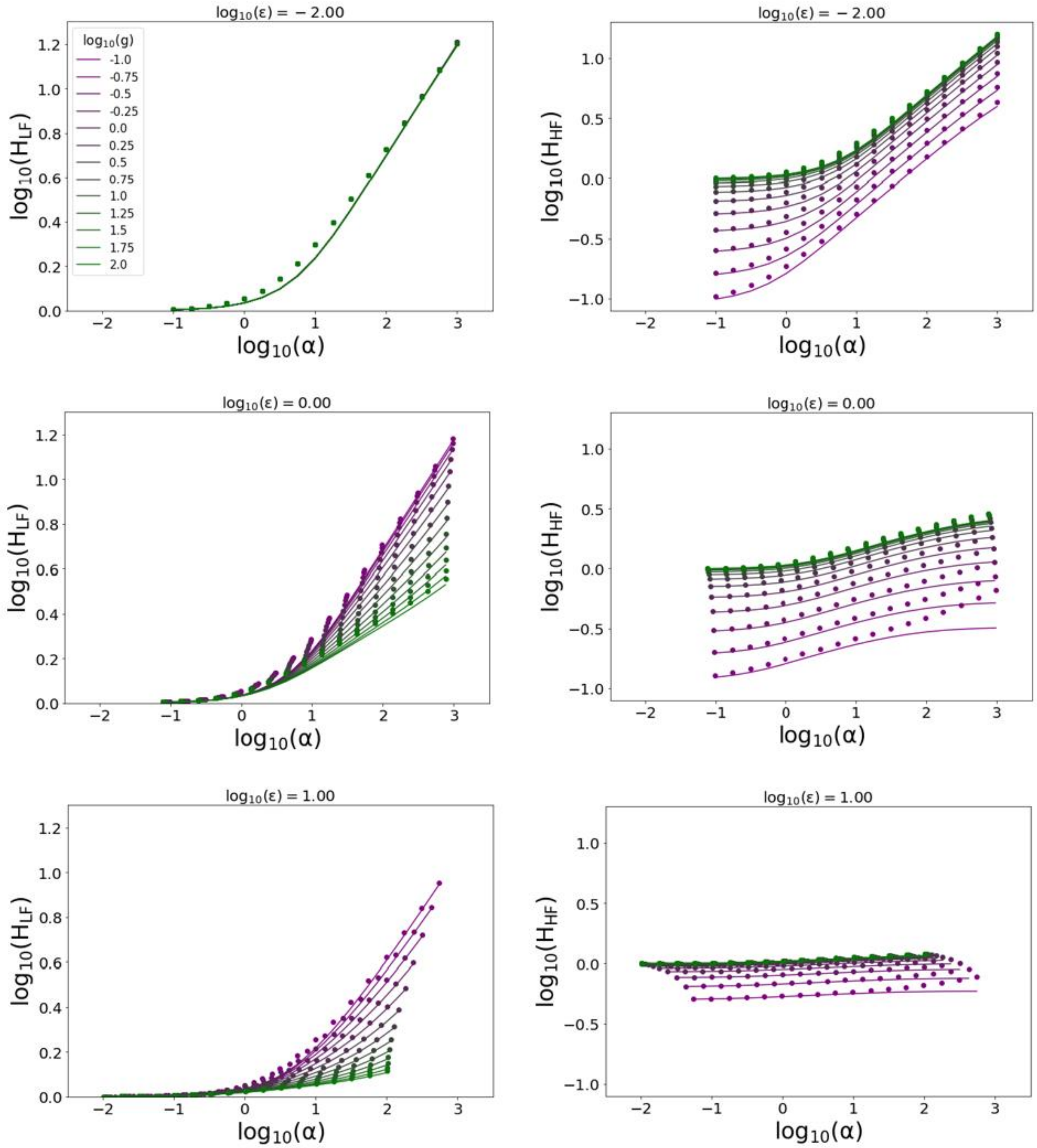

Figure 2.7. Change in H_{LF} and H_{HF} as a function of the ratio of sheet resistance to the low frequency intercept without sheet resistance. Dots represent simulated data points, and the lines represent the 2D model analytical solutions. Each plot is parametric in g.

The ratio of the low frequency intercept with sheet resistance to low frequency intercept without sheet resistance deviates significantly from 1 after an α of 10. There is an asymptotic limit at low α, i.e. low sheet resistance, that is independent of γ or ϵ, however the asymptotic limit at high α is a function of γ and ϵ. These asymptotic limits are well captured by the 2D analytical solution represented as the superimposed lines on Figure 2.7. At low ϵ, for which $L <<$ p, *i.e.* the electrolyte thickness is much smaller than the current collector pitch, a 1D solution approximates the 3D simulation results. This is expected as the y dimension is eliminated by the small magnitude of L compared to p. In the 1D limit as α approaches infinity, the ratio of the low frequency intercept with sheet resistance to low frequency intercept without sheet resistance scales with the $\sqrt{\alpha}$. The 2D model fails to capture the intermediate region between α of 0.1 and 10. Larger values of ϵ and γ, i.e. thicker or more resistive electrolytes, appear to delay the impact of larger values of α.

The α at which the ratio of the high frequency intercept with sheet resistance to low frequency intercept without sheet resistance deviates from its initial value is dependent on γ. As γ increases, the onset of deviation occurs at ever increasing values of α until leveling out at large values of γ. As α approaches zero sheet resistance, the ratio of the high frequency intercept with sheet resistance to low frequency intercept without sheet resistance approaches γ, but only if γ is small. This is because γ is the ratio of $R_{\mathrm{HF}}^{\mathrm{o}}$ to $R_{\mathrm{LF}}^{\mathrm{o}}$. At large γ, electrolyte resistance composes nearly all the cell resistance. Like H_{LF}, at large values of ϵ, in which $L >> p$, the effects of sheet resistance become less significant. This is because at larger values of ϵ, the potential gradients within the electrolyte penetrate a smaller fraction of the total electrolyte thickness, thus becoming significantly smaller contributors to the electrolyte's resistance. The 2D model captures the effects of sheet resistance on the ratio of the high frequency intercept with sheet resistance to low frequency intercept without sheet resistance quite well except once again in the intermediate region. The deviations of the 2D model at large values of sheet resistance, α, and increasing values of the ratio of electrolyte thickness to half pitch, ϵ, is suspected to be the result of numerical simulation limitations at large values of α. At larger values of α, the gradients around the wires in COMSOL model become too fine to accurately model with the finest FEM mesh that accessible computers could support.

The reason that H_{LF} and H_{HF} deviate from their values in the absence of sheet resistance is because at higher values of sheet resistance, α, the current flows through smaller superficial areas of the cell. Sample screenshots of contour plots of potential in Figure 2.8 exemplify this effect. Figure 2.8A and Figure 2.8B share the same γ and ϵ conditions, but Figure 2.8B has negligible sheet resistance and Figure 2.8A has an α of 570. In Figure 2.8B, the entire area (p^2) of the cell is used, whereas in Figure 2.8A, the gradients of potential are so steep that only a fraction of the superficial area carries any current. Effectively, this increases the measured resistance. As expected, there exists little to no gradients in the *xy* plane in either the electrode or electrolyte at low values of α, with most of the potential drop occurring because of the surface reaction. In Figure 2.8A, there are steep potential gradients adjacent to the wires while a gradient in the *xy* plane exists deep into the electrolyte.

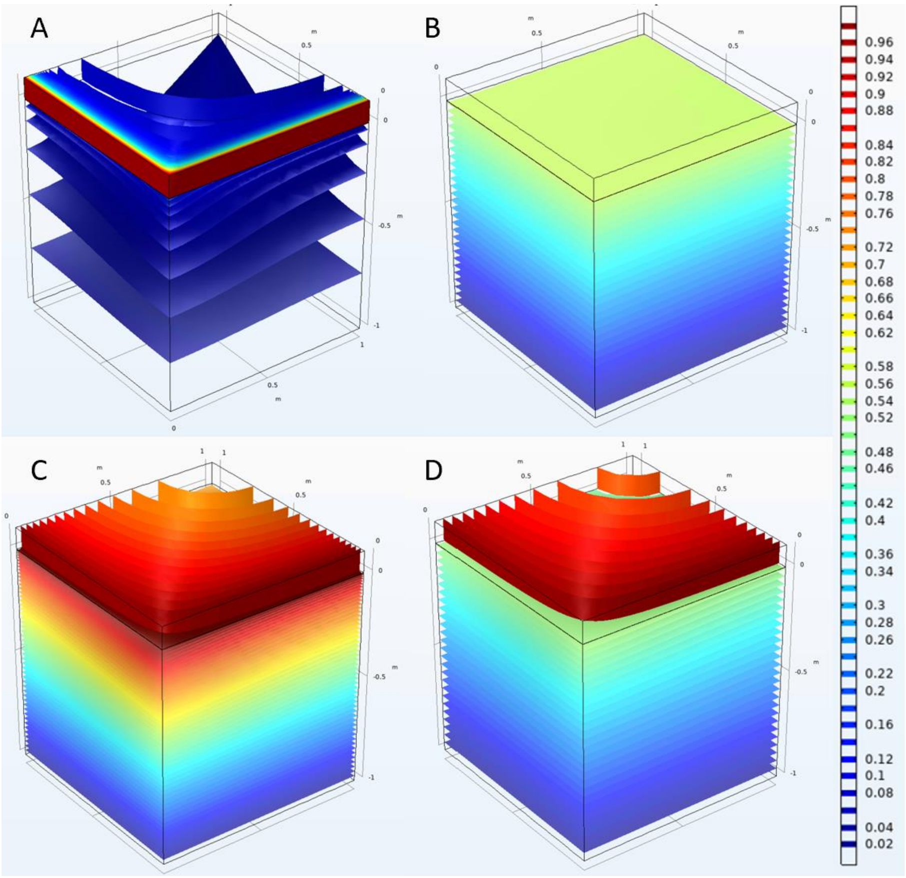

Figure 2.8 Sample screen shots of the contours of potential gradients in the 3D model at a g of 1 and ε of 1. Potential values are shown scaled from 0 to 1 (blue to red). (A) is at an α of 570 and zero frequency. (B) is at an α of 0.57 and zero frequency. (C) is at an α of 1.14 and σ of 0.01. (D) is at an α of 1.14 and σ of 1000.

This effect is also frequency dependent. Figure 2.8C and Figure 2.8D compare the same α (1.14 in this case), γ, and ϵ with Figure 2.8C simulated with a frequency, σ, of 0.01 and Figure 2.8D simulated with a σ of 1000. At higher frequencies, the potential gradients are steeper; the current is constricted through a smaller area and the resistance appears larger. While the plots of Figure 2.8 are in the limits of zero frequency and infinite frequency, the simulation and 2D solution indicate that the Nyquist plots features also have a frequency dependence.

This frequency dependence causes shifts in the shape of the Nyquist plot as shown in Figure 2.9. The shapes of the arcs in the figures are caused by only a difference in sheet resistance. As programmed, the arc with little sheet resistance (blue x's) is a semicircle, however the arc with orders of magnitude more sheet resistance would appear as a Gerischer shape despite combined kinetic and transportation limitations not being the underlying cause.

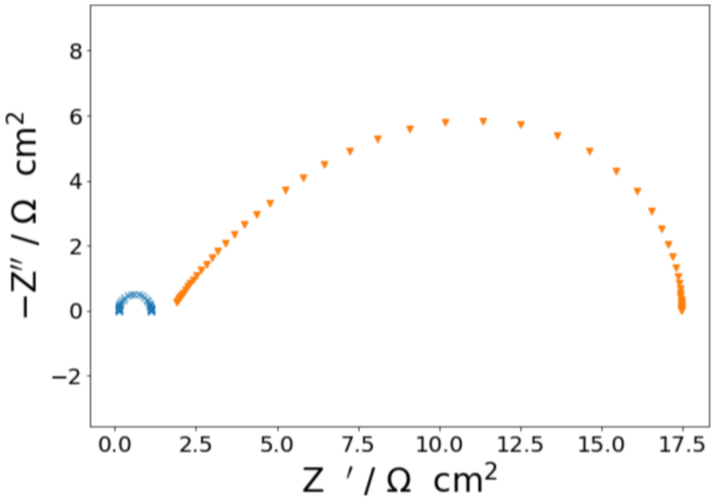

Figure 2.9. The two COMSOL-produced Nyquist plots presented are at the same γ and ε. The difference is that the blue x's are for an α of 0.01 and the orange triangles are for an α of 1000.

One way to display the variation in Nyquist plot shape is to plot the asymmetry of the Nyquist plot as a function of $\alpha, \gamma,$ and ϵ. This asymmetry ratio is defined as

$$R_{\mathrm{asym}} = \frac{(R_{\mathrm{peak}} - R_{\mathrm{HF}})}{(R_{\mathrm{LF}} - R_{\mathrm{peak}})} \quad (2.38)$$

where R_{peak} is the real resistance at the peak frequency. If R_{asym} is equal to one, then the Nyquist plot appears as a semicircle, as would be expected if the electrode were kinetically limited, geometrically uniform, and well defined. An R_{asym} greater than 1 indicates deviation from a semicircle, which occasionally could be mistaken as a Gerischer impedance. Many shapes can result (not shown here), and there is no consistent trend in angle of incidence at high frequency. Sometimes there appears to be two overlapping arc features in the Nyquist plot when there should not be (not shown).

The effects of $\alpha, g,$ and ϵ on the ratio of the peak frequency measured to the peak frequency without sheet resistance, called f_{α}, and on R_{asym} is shown in Figure 2.10. The 2D analytical solution can be numerically solved to find the peak frequency and R_{peak}. The model is superimposed on the 3D COMSOL results in Figure 2.10. As can be seen in the figure, the observed peak frequency can vary by up to 50% depending on the value of $\alpha, \gamma,$ and ϵ. f_{α} varies the least at large γ and small ϵ. Similarly, the value of R_{asym} can vary by up to 50% and is sensitive at values of α above 1. R_{asym} varies the least at large electrolyte resistivity, γ, and small ratio of electrolyte thickness to current collector pitch, ϵ. The 2D analytical solution once again fails within the intermediate range but captures the asymptotic limits.

While solving the solution numerically for f_{α} and R_{asym}, it is suggested to use at least 20,000 eigenvalues and to use scaled frequency steps of about 0.02. It is cumbersome to empirically modify the 2D solution to match that of the 3D solution, and it would not add much value to the underly conclusions. The maximum percent error between the simulation and the 2D model occurs in the intermediate zone and reaches 15% error around an α of 10.

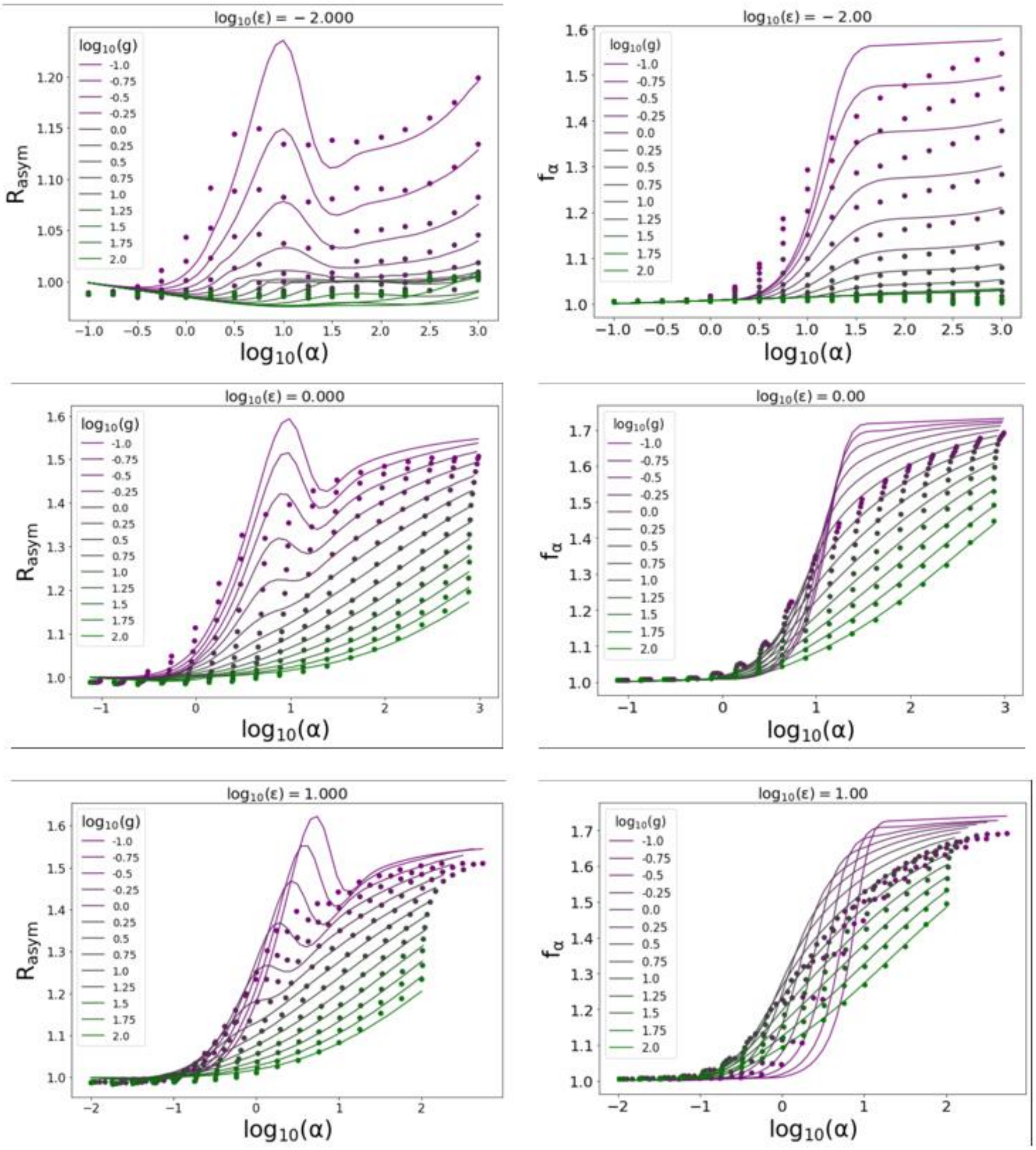

Figure 2.10 The left column shows the effect of α on the asymmetric ratio (R_{asym}) parametric in g while the right column shows the effect of α on f_α parametric in g. Each row represents a different simulation done at a different ϵ.

2.6 DISCUSSION

The sheet resistance of a given electrode is estimated as

$$R_{\mathrm{sheet}} = \frac{p^2}{b\sigma_{\mathrm{e}}}\left(\frac{\tau_{\mathrm{t}}}{1-\lambda}\right) \tag{2.39}$$

where λ and τ_t are porosity and tortuosity. The electronic conductivity of GDC10 at 800 ºC and $p_{\mathrm{O_2}}$ of $10^{-16.16}$ bar is 0.04339 S/cm[51], the estimated thickness (b) is 4 µm, τ_t is estimated as 1.5, λ as 0.5, and the nominal value of p is 0.25 mm. Thus, the sheet resistance is estimated as 108.032 Ω cm^2.

The α_{p} values estimated from this sheet resistance are orders of magnitude smaller than the $\alpha_{2\mathrm{D}}$ values estimated by the 2D model based on experimentally measured values; see Table 2.3. As an example, the low frequency intercept measured with a porous current collector for the lowest $p_{\mathrm{CO_2}}$ condition was 846.5 Ω. Given that the cell is symmetric, the arc resistance measured is twice a single electrode's resistance. Therefore, the resistance of a single electrode is

$$R_{\mathrm{LF_1}} = \left[\frac{(R_{\mathrm{LF_2}} - R_{\mathrm{HF}})}{2} + R_{\mathrm{HF}}\right] A_{\mathrm{elc}} \tag{2.40}$$

where $R_{\mathrm{LF_1}}$ refers to the resistance at the low frequency intercept of one electrode, $R_{\mathrm{LF_2}}$ refers to the resistance at the low frequency intercept of two electrodes (as shown in Figure 2.7), and A_{elc} is the electrode geometric area, estimated as 0.257 cm^2. In this case, $R^{\mathrm{o}}_{\mathrm{LF_1}}$ is 113.99 Ω cm^2. Thus, the α_{p} for this example is predicted to be

$$\alpha_{\mathrm{p}} = \frac{R_{\mathrm{sheet}}}{R^{\mathrm{o}}_{\mathrm{LF_1}}} = \frac{108.032\ \Omega\ \mathrm{cm}^2}{113.99\ \Omega\ \mathrm{cm}^2} = 0.948 \tag{2.41}$$

The $R_{\mathrm{LF_1}}$ for the example condition with sheet resistance is 2,039.77 Ω cm^2. The H_{LF} is 17.91. The $\alpha_{2\mathrm{D}}$ value from the 2D model that achieves this H_{LF} with a γ and ε of 0.088 and 17.240 is 1,391. This is larger than α_{p} by three orders of magnitude. The implication is that the implicit assumption that the gold mesh grid is successfully contacting the GDC10 surface is incorrect. If p^2 were substituted with the average geometric area, then α_p would be within just over half an order of magnitude smaller than that predicted by the 2D model, as shown in Table 2.3. In this situation, the two α values are more comparable, which implies that the entire mesh grid was not successfully contacting the electrode.

Continuing the example, the H_{HF} measured is 1.55, however using the α_{2D} determined by H_{LF}, the H_{HF} estimated by the 2D model is 0.097, around an order of magnitude smaller. This is a consistent trend for the other two conditions measured as shown in Table 2.3. This is similar to the situation just described regarding H_{LF} in which the observed values and 2D model estimated values are separated by an order of magnitude.

The 2D model captures the change in peak frequency as a function of α through the frequency parameter f_{α}. The 2D model overestimates the effect on $\boldsymbol{f_{\alpha}}$ for condition 1 and underestimates it for conditions 2 and 3 based on using the α_{2D} determined using H_{LF}. In all situations, the 2D model predicts an $\boldsymbol{f_{\alpha}}$ of 1.74. What is observed is arguably an estimated $\boldsymbol{f_{\alpha}}$ of 1.65 to 2.5. The fact that the multiplier on the frequency was quite large for all conditions measured means the α value is likely beyond 10^2.

Due to the quality of the data collected, it is hard to say exactly what the asymmetric ratio is for each case, as this is dependent on what point is chosen to be the peak frequency. The choice of experimental peak frequency and associated resistance is somewhat subjective and may not line up exactly with what the experimental peak frequency may have been if more measurements at smaller intervals of frequency were taken. It can, however, be said that for each gas environment, once the porous gold layer was added, the asymmetric ratio decreased, and the Nyquist plots transitioned to more clearly defined semi-circular like shapes. It is likely that the sheet resistance was a major contributor to the Nyquist plot shape distortion.

It is not clear why the 2D model does not precisely explain the experimental results. The lack of well-defined geometry likely plays a role. First, the mesh had been bent and used multiple times resulting in a non-uniform pitch and non-uniform overall shape. The diameters of the electrodes on both sides of the electrolyte were not equal, which makes the area poorly defined. The effect of this deviation in symmetry is unclear. The porosity and tortuosity were not directly measured but were assumed based on past work[48] and SEM images of similar cells made by the same methods. The thickness of the electrodes was designed to be four microns by the screen-printing method; however, it is not guaranteed to be uniformly four microns and can vary, especially around the edges of the screen-printed circle. Lastly, the model assumes all mesh wires make perfect contact with the GDC10 layer. This is not true in the experiment as the wires naturally overlap to form a mesh. Furthermore, depending on the mechanism used to sandwich the gold mesh to the electrode, not all points of contact may be effectively touching the GDC10 surface. In this experimental set up, a ceramic screw and plate clamp was used to hold the cell together, though after a thermal cycle, it was always predictably looser than when it initially entered the furnace.

Table 2.3. Summary of the comparison between the expected effect of sheet resistance and the actual experimental measurements.

	Condition		
Parameter	1	2	3
$R^{\mathrm{o}}_{\mathrm{LF}_1}$ (Ω cm^2)	20.478	39.141	113.985
$R^{\mathrm{o}}_{\mathrm{HF}}$ (Ω cm^2)	10.065	10.065	10.065
γ	0.492	0.257	0.088
R_{sheet} (Ω cm^2)	108.032	108.032	108.032
α_{p}	5.276	2.760	0.948
$\log_{10}(\alpha_{\mathrm{p}})$	0.722	0.441	-0.023
R_{LF_1} (Ω cm^2)	765.42	1326.08	2039.77
H_{LF}	37.38	33.88	17.90
$\log_{10}(H_{\mathrm{LF}})$	1.57	1.53	1.25
α_{2D}	10,688	6,084	1,391
$\log_{10}(\alpha_{\mathrm{2D}})$	4.03	3.78	3.14
$\log_{10}(\alpha_{\mathrm{p}})$*	3.34	3.06	2.59
H_{HF}	8.64	4.52	1.55
H_{HF} using α_{2D}	0.545	0.285	0.098
f_{α}	1.65	2	2.51
$f_{\alpha_{2D}}$	1.74	1.74	1.74

*if the electrode area were used in place of p^2 in Eqn. 2.39.

2.6.1 *Applicability to literature*

In 2011, it was found that the resistance of a thin dense electrode $La_{0.6}Sr_{0.4}Co_{0.2}Fe_{0.8}$ changed with thickness (100 nm, 250 nm, 500 nm, and 1000 nm) when it should not have[**52**]. Sheet resistance was suspected to be the cause. A mesh current collector was used with an unspecified pitch. After correspondence with the author, the pitch is reasonably assumed to be 0.312 mm. The high frequency intercept was only reported for the 1000 nm thick electrode experiment. Thus, the measured high frequency intercept was assumed to remain unchanged as a function of electrode thickness, which enables the calculation of the low frequency intercept at the other thicknesses. Given the value of $\boldsymbol{\epsilon}$ for this cell, estimated to be eight, the high frequency intercept is unlikely to be perturbed by sheet resistance in this case. The well-defined geometric parameters and assumptions correspond to a $\log_{10}(\alpha_p)$ of -1.77 for the 100 nm electrode thickness experiment. The 2D model would predict a $\log_{10}(\alpha_{2D})$ of 2.51, more than four order of magnitudes greater than α_p. Once again this is a stark difference. If p^2 were replaced with the geometric area of the electrode, then $\log_{10}(\alpha_p)$ would be 1.74, within an order of magnitude of α_{2D}. The implication is that perhaps the mesh is not effectively contacting the electrode.

As another example, in 2001 water electrolysis was done on $La_{0.7}Ca_{0.3}Cr_{0.8}Ti_{0.2}O_3$ and it was found that a change in porous electrode thickness from 100 microns to 20 microns resulted in a considerable difference in the high frequency and low frequency intercept resistances[54]. The change in high frequency intercept when geometric area does not change is a key indicator of the presence of sheet resistance, though it is not a required one, as Figure 2.7 shows at large ε and γ. Assuming the 100 micron electrode is thick enough to be considered an ideal electrode without any sheet resistance, then the 20 micron electrode is estimated to have a $\log_{10}(\alpha_{2D})$ of 2.10 for the highest concentration of hydrogen condition. Using the values from the literature, and under the same wire mesh pitch assumptions of the last example, the $\log_{10}(\alpha_p)$ is -0.632, about two and a half orders of magnitude less than α_{2D}. Once again, it appears that perhaps the mesh wires were not making effective contact with the electrode surface. If the electrode geometric area is substituted for p^2, then $\log_{10}(\alpha_p)$ would be estimated to be 2.877 for the 20-micron electrode at the highest hydrogen concentration (2.30% H_2O balance H_2), much closer in magnitude to α_{2D}.

As a final example, in 2015 a similar material under conditions similar to that of the first literature example was shown to have no signs of sheet resistance[53]. Counterintuitively, a dense 2-micron film of LSCF6428 had half the electrode resistance as that of a dense 4-micron LSCF6428 electrode studied under the same conditions. It was concluded that sheet resistance did not play a part. The 2D model presented here would agree, since the pitch is so small, and LSCF6428 has orders of magnitude higher conductivity than GDC10. Perhaps in this case, effective contact of the current collector meshes with the electrode surface was maintained. The LSCF6428 electrode thickness and mesh pitch are comparable to the ones used in the experimental work presented here with GDC10. It is possible that the GDC10 electrode with a slightly larger pitch and greater than four orders smaller conductivity is more sensitive to poor contact between a mesh and electrode than LSCF6428. Even if p^2 were replaced with the electrode geometric area for the LSCF6428 dense films, the $\log_{10}(\alpha_p)$ would be -0.19; small enough to have a negligible impact on the impedance response.

2.6.2 *Recommendations for Making a Cell*

By inspection, the COMSOL and 2D modeling suggests that to mitigate the risk of sheet resistance effects on the high and low frequency intercepts, it is best to have an $\epsilon > 1$ and $\gamma > 10$. To mitigate the effects of sheet resistance on peak frequency and shape distortion, it is best to have an $\epsilon < 1$ and $\gamma > 10$. The reader is guided to Figure 2.7 and Figure 2.10 to recognize that these guidelines will only allow a higher tolerance for sheet resistance, not eliminate sheet resistance effects. Given that using thin films is crucial to research of electrode kinetics, an additional important priority is to decrease the pitch size or use a porous current collector. A thick electrolyte also minimizes the effect of reference electrolyte placement[55].

2.7 CONCLUSIONS

A 2D model and 3D COMSOL simulation were developed to explore the effect of sheet resistance on the measured low frequency intercept, high frequency intercept, peak frequency, and shape of a Nyquist plot. The model showed that significant sheet resistance relative to low frequency intercept resistance in the absence of sheet resistance can have a significant impact on measured quantities. This phenomenon was shown in an experiment where EIS was performed on a GDC10 electrode undergoing CO_2 electrolysis with and without a porous current collector layer. With only the addition of a porous current collecting layer, the expected electrolyte resistance was observed, the peak frequency was smaller, the shapes were more semi-circular, and the low frequency intercept was 1.5 orders of magnitudes less.

Given the pitch used in the experiment presented here and in the cited literature, the 2D model would estimate that the sheet resistance is negligible. This, however, turns out not to be the case, and it is suspected that the current collector mesh does not maintain adequate contact with the electrodes. If electrode geometric area is used to calculate expected sheet resistance, then the 2D models and observations are within about an order to an order and a half magnitude of the estimated sheet resistance impact on low frequency and high frequency intercept behavior.

Regarding shape, a Gerischer-response can appear, but it may result as a function of sheet resistance and not as competition of kinetics and mass transport limitations. To simulate a Gerischer-response in the 2D model, the term $(1 + j\sigma)$ is replaced with $(1 + j\sigma)^{1/2}$. 3D COMSOL simulation with a Gerischer shape remains as future work. Given that only certain parts of the meshes contact the electrode surface, it is suggested that future work develop a physics-based model based on surface contact points per unit area instead of line contacts.

By inspection, the COMSOL and 2D modeling suggests that, to mitigate the risk of sheet resistance effects on the high and low frequency intercepts, it is best to have an $\epsilon > 1$ and $\gamma > 10$. To mitigate the effects of sheet resistance on peak frequency and shape distortion, it is best to have an $\epsilon < 1$ and $\gamma > 10$. Additionally, it is recommended to use a small current collector mesh pitch or porous current collecting layer. Less caution is needed for an electrode with high conductivity. If a porous current collector is not an option, due diligence on ensuring that the mesh is pressed against the electrode surface at all times is required.

2.8 APPENDICES

2.8.1 *Appendix A: Derivation of 2D Model*

Using Figure 2.5 as a reference, the current through interface Γ_6, $\Gamma_{3,\mathrm{elc}}$, and Γ_1 are

$$i_{\Gamma_6} = \frac{1}{R_{\mathrm{elc}}}(\phi_1 - \phi) + C_{\mathrm{elc}}\frac{\partial}{\partial t}(\phi_1 - \phi) \tag{2A.1}$$

$$i_{\Gamma_{3,\mathrm{elc}}} = \sigma_{\mathrm{e}} b\left(\frac{\partial \phi_1^2}{\partial x^2}\right) \tag{2A.2}$$

$$i_{\Gamma_1} = -\sigma_{\mathrm{i}}\left(\frac{\partial \phi}{\partial y}\right)|_{y=L} \tag{2A.3}$$

Since charge is conserved, they should all be equal. An ordinary differential equation (ODE) results

$$-\sigma_{\mathrm{i}}\left(\frac{\partial \phi}{\partial y}\right)|_{y=L} = \frac{1}{R_{\mathrm{elc}}}(\phi_1 - \phi) + C_{\mathrm{elc}}\frac{\partial}{\partial t}(\phi_1 - \phi) = \sigma_{\mathrm{e}} b\left(\frac{\partial \phi_1^2}{\partial x^2}\right) \tag{2A.4}$$

Using the scaling from Table 2.1, the ODE can be rewritten as

$$\frac{\partial^2\psi_1}{\partial\xi^2} = \frac{\alpha Y}{(1-\gamma)}\left(\psi_1 - \psi_{\eta=0}\right) = -\frac{\epsilon}{\beta}\left(\frac{\partial\psi}{\partial\eta}\right)_{\eta=0} \tag{2A.5}$$

Where Y is either (1+jσ) for an RC element or (1+jσ)$^{1/2}$ for a Gerischer impedance.

Within the electrolyte, the partial differential equation to be solved is

$$\nabla^2\phi = 0 \tag{2A.6}$$

Scaling and non-dimensionalizing results in

$$\nabla^2\psi = 0 \tag{2A.7}$$

The boundary conditions are

$$\phi_1|_{x=0} = \phi_\mathrm{o} \tag{2A.8}$$

$$\frac{\partial\phi_i}{\partial x}\Big|_{x=0,\ x=\frac{p}{2},\ x=p} = 0 \tag{2A.9}$$

$$-\sigma_\mathrm{i}\left(\frac{\partial\phi}{\partial y}\right)\Big|_{y=L} = \sigma_\mathrm{e} b\left(\frac{\partial\phi_1^2}{\partial x^2}\right) \tag{2A.10}$$

$$\phi|_{y=0} = 0 \tag{2A.11}$$

and can be scaled and non-dimensionalized to

$$\frac{\partial\psi}{\partial\xi}\Big|_{\xi=0,\frac{1}{2},1} = 0 \tag{2A.12}$$

$$\psi|_{\eta=\epsilon} = 0 \tag{2A.13}$$

$$\psi_1\,|_{\xi=0} = \cos\,(\sigma\tau) \tag{2A.14}$$

Time is removed by

$$\psi = \frac{1}{2}\bar{\psi}e^{j\sigma\tau} + \frac{1}{2}\bar{\psi}^{*}e^{-j\sigma\tau} \tag{2A.15}$$

$$\psi_1 = \frac{1}{2}\bar{\psi}_1 e^{j\sigma\tau} + \frac{1}{2}\bar{\psi}_1^{*}e^{-j\sigma\tau} \tag{2A.16}$$

$$\cos(\sigma\tau) = \frac{1}{2}e^{j\sigma\tau} + \frac{1}{2}e^{-j\sigma\tau} \tag{2A.17}$$

Continuing only with the e$^{j\sigma\tau}$ terms the ODE and PDE to be solved result in

$$\frac{\partial^2 \overline{\psi}_1}{\partial \xi^2} = \frac{\alpha Y}{(1-\gamma)}\left(\overline{\psi}_1 - \overline{\psi}_{\eta=0}\right) = -\frac{\epsilon}{\beta}\left(\frac{\partial \overline{\psi}}{\partial \eta}\right)_{\eta=0} \qquad (2A.18)$$

$$\nabla^2 \bar{\psi} = 0 \qquad (2A.19)$$

and the boundary conditions become

$$\frac{\partial \bar{\psi}}{\partial \xi}\Big|_{\xi=0,\frac{1}{2},1} = 0 \qquad (2A.20)$$

$$\bar{\psi}|_{\eta=\epsilon} = 0 \qquad (2A.21)$$

$$\bar{\psi}_1\,|_{\xi=0} = 1 \qquad (2A.22)$$

Using separation of variables and the boundary conditions for the PDE, we find that

$$\bar{\psi} = A_o(1-\eta) + \sum_{n=1}^{\infty} A_n[\sinh(\mu_n\eta) - \tanh(\mu_n)\cosh(\mu_n\eta)]\cos(\lambda_n\xi) \qquad (2A.23)$$

where $\lambda_n = \frac{n\pi}{2}$, $\mu_n = \lambda_n\epsilon$, and A_o and A_n are yet to be determined.

The ODE is first framed as

$$\frac{\partial^2 \bar{\psi}_1}{\partial \xi^2} - \alpha'\bar{\psi}_1 = -\alpha'\bar{\psi}|_{\eta=0} \qquad (2A.24)$$

$$\alpha' = \frac{\alpha Y}{1-\gamma}. \qquad (2A.25)$$

The general solution is

$$\bar{\psi}_1^{\mathrm{G}} = c_1 e^{\xi\sqrt{\alpha'}} + c_2 e^{-\xi\sqrt{\alpha'}} \qquad (2A.26)$$

and the particular solution must match the form of the inhomogeneous term

$$\bar{\psi}_1^{p} = B_\mathrm{o} + \sum_{n=1}^{\infty} B_n \cos(\lambda_n\xi) \qquad (2A.27)$$

Substituting the particular solution into the ODE finds that

$$B_\mathrm{o} = A_\mathrm{o} \qquad (2A.28)$$

$$B_n = -\frac{\alpha' A_n \tanh(\mu_n)}{\lambda_n^2 + \alpha'} \qquad (2A.29)$$

Therefore,

$$\bar{\psi}_1 = c_{\mathrm{o}} \cosh\left(\sqrt{\alpha'}(1-\xi)\right) + A_{\mathrm{o}} + \sum B_n \cos(\lambda_n \xi) \tag{2A.30}$$

$$\bar{\psi}_1^{\mathrm{G}} = c_{\mathrm{o}} \cosh\left(\sqrt{\alpha'}(1-\xi)\right) \tag{2A.31}$$

Using the boundary conditions Eqn. 2A.22,

$$1 = c_{\mathrm{o}} \cosh\left(\sqrt{\alpha'}\right) + A_{\mathrm{o}} + \sum B_n \tag{2A.32}$$

Focus turns now to the other side of the ODE,

$$\alpha'\left(\psi_1 - \psi_{\eta=0}\right) = -\frac{\epsilon}{\beta}\left(\frac{\partial\psi}{\partial\eta}\right)_{\eta=0} \tag{2A.33}$$

First, $\bar{\psi}^{G}{}_{1}$ needs to be put into the same basis function as $\bar{\psi}$. Let

$$\bar{\psi}_1^{\mathrm{G}} = c_{\mathrm{o}} \cosh\left(\sqrt{\alpha'}(1-\xi)\right) = \left(D_{\mathrm{o}} + \textstyle\sum_n D_n \cos(\lambda_n \xi)\right) c_{\mathrm{o}} \tag{2A.34}$$

In which case, using orthogonality

$$D_{\mathrm{o}} = \int_0^1 \cosh\left(\sqrt{\alpha'}(1-\xi)\right) d\xi = \frac{\sinh\left(\frac{\sqrt{\alpha'}}{2}\right)}{\frac{\sqrt{\alpha'}}{2}} \tag{2A.35}$$

$$D_n = \frac{\int_0^1 \cosh\left[\sqrt{\alpha'}(1-\xi)\right] \cos(\lambda_n \xi) d\xi}{\int_0^1 \cos^2(\lambda_n \xi) d\xi} = \frac{2\sqrt{\alpha'} \sinh\left(\sqrt{\alpha'}\right)}{\alpha' + \lambda_n^2} \tag{2A.36}$$

Substituting the appropriate equations into Eqn. 2A.33,

$$\frac{A_{\mathrm{o}}}{c_{\mathrm{o}}} = \alpha' \beta D_{\mathrm{o}} \tag{2A.37}$$

$$\frac{A_n}{c_{\mathrm{o}}} = -\frac{D_n}{\frac{\lambda_n \epsilon}{\alpha' \beta} + \frac{\lambda_n^2 \tanh(\lambda_n \epsilon)}{\lambda^2 + \alpha'}} \tag{2A.38}$$

$$\frac{B_n}{c_{\mathrm{o}}} = -\frac{\alpha' \tanh(\lambda_n \epsilon)}{\lambda_n^2 + \alpha'}\left(\frac{A_n}{c_{\mathrm{o}}}\right) \tag{2A.39}$$

$$\frac{1}{c_{\mathrm{o}}} = \cosh\left(\sqrt{\alpha'}\right) + \beta\sqrt{\alpha'} \sinh\left(\sqrt{\alpha'}\right) + \sum_n^{\infty} \frac{B_n}{c_{\mathrm{o}}} \tag{2A.40}$$

Therefore, by calculating 1/c$_{\mathrm{o}}$,

$$A_{\mathrm{o}} = c_{\mathrm{o}} * \frac{A_{\mathrm{o}}}{c_{\mathrm{o}}} \tag{2A.41}$$

$$A_n = c_{\mathrm{o}} \left(\frac{A_n}{c_{\mathrm{o}}}\right) \tag{2A.42}$$

$$B_n = c_{\mathrm{o}} \left(\frac{B_n}{c_{\mathrm{o}}}\right) \tag{2A.43}$$

The impedance can then be found by

$$\bar{I} = \int_0^p -\sigma_i \left(\frac{\partial \bar{\phi}}{\partial \eta}\right) |_{y=0} dx \tag{2A.44}$$

which when non-dimensionalized is

$$\bar{I} = \int_0^1 -\sigma_i \phi_{\mathrm{o}} \left(\frac{\partial \bar{\psi}}{\partial \eta}\right) |_{\eta=0} d\xi \tag{2A.45}$$

The integral becomes

$$\int_0^1 \left(\frac{\partial \bar{\psi}}{\partial \eta}\right) |_{\eta=0} d\xi = -\frac{A_{\mathrm{o}}}{\epsilon} + \int_0^1 \sum_n^\infty A_n \mu_n \cos(\lambda_n \xi)\, d\xi = -\frac{A_{\mathrm{o}}}{\epsilon} \tag{2A.46}$$

because

$$\int_0^1 \cos(\lambda_n \xi)\, d\xi = 0 \tag{2A.47}$$

Thus

$$\bar{I} = \frac{\sigma_i \phi_{\mathrm{o}}}{\epsilon} \left(\frac{A_{\mathrm{o}}}{c_{\mathrm{o}}}\right) c_{\mathrm{o}} = \frac{\sigma_i \phi_{\mathrm{o}} \alpha' \beta}{\epsilon} \left(\frac{\sinh\left(\frac{\sqrt{\alpha'}}{2}\right)}{\frac{\sqrt{\alpha'}}{2}}\right) c_{\mathrm{o}} \tag{2A.48}$$

The current density is

$$\bar{\imath} = \frac{\bar{I}}{p} = \frac{c_{\mathrm{o}} \sigma_i \phi_{\mathrm{o}} \frac{\sqrt{\alpha'}}{2} \beta \sinh\left(\frac{\sqrt{\alpha'}}{2}\right)}{L} \tag{2A.49}$$

The impedance normalized to the low frequency intercept is

$$H = \frac{Z}{R_{\mathrm{LF}}} = \frac{\phi_{\mathrm{o}}}{\bar{\imath} R_{\mathrm{LF}}^{\mathrm{ideal}}} = \frac{1}{c_{\mathrm{o}}} \left(\frac{\alpha}{\frac{\sqrt{\alpha'}}{2} \sinh\left(\frac{\sqrt{\alpha'}}{2}\right)}\right) \tag{2A.50}$$

2.8.2 *Appendix B: High Frequency Intercept*

How H_{HF} changes with α, ε, and γ can be found by taking the limit of H as σ approaches infinite:

$$\lim_{\sigma\to\infty}(H) = \alpha\beta\left(1+\sum_{1}^{N}\frac{\tanh(2\pi n\epsilon)}{\pi n\epsilon+2\beta(\pi n)^{2}\tanh(2\pi n\epsilon)}\right) \tag{2B.1}$$

2.8.3 *Appendix C: COMSOL equations*

2.8.3.1 C.1 Electrolyte Current Flux

The current flux within the x direction of the electrolyte is defined as

$$i_x = -\sigma_{\mathrm{i}}\left(\frac{\partial\phi}{\partial x}\right) \tag{2C.1}$$

This can be non-dimensionalized using the following terms

$$\psi = \frac{\phi_{\mathrm{o}}}{\phi} \tag{2C.2}$$

$$\xi = \frac{x}{p} \tag{2C.3}$$

thus becoming

$$i_x = -\sigma_i\frac{\phi_{\mathrm{o}}}{p}\left(\frac{\partial\psi}{\partial\xi}\right) \tag{2C.4}$$

The current density can be scaled by the applied potential (ϕ_{o}) and electrode resistance (R_{elc})

$$N_\xi = \frac{i_x R_{elc}}{\phi_{\mathrm{o}}} \tag{2C.5}$$

Substituting i_x into Eqn 2C.5 and removing time,

$$N_\xi = -\frac{\epsilon}{\gamma}\frac{\partial\overline{\psi}}{\partial\xi} \tag{2C.6}$$

Given that the electrolyte is isotropic and normalizing the *y* and *z* direction according to the following

$$\eta = \frac{y}{p} \tag{2C.7}$$

$$\zeta = \frac{z}{p} \tag{2C.8}$$

the scaled current density in the normalized *z* and *y* directions in the electrolyte are

$$N_\eta = -\frac{\epsilon}{\gamma}\frac{\partial\overline{\psi}}{\partial\eta} \tag{2C.9}$$

$$N_\zeta = -\frac{\epsilon}{\gamma}\frac{\partial\overline{\psi}}{\partial\zeta} \tag{2C.10}$$

2.8.3.2 C.2 Electrode Current Flux

Within the current collector, the current in the *x* direction is defined as

$$i_x = -\sigma_{\mathrm{e}}^{\mathrm{eff}}\left(\frac{\partial\phi_1}{\partial x}\right) \tag{2C.11}$$

After substitution of scaling factors, normalization, removing time, and scaling the current density as before

$$N_\xi = -\frac{1}{\alpha\delta}\left(\frac{\partial\overline{\psi}_1}{\partial\xi}\right) \tag{2C.12}$$

where in this case α is normalized to the electrode resistance

$$\alpha = \frac{p^2}{\sigma_{\mathrm{e}} b R_{\mathrm{elc}}} \tag{2C.13}$$

Similarly

$$N_\eta = -\frac{1}{\alpha\delta}\left(\frac{\partial\overline{\psi}_1}{\partial\eta}\right) \tag{2C.14}$$

$$N_\zeta = -\frac{\kappa}{\alpha\delta}\left(\frac{\partial\overline{\psi}_1}{\partial\zeta}\right) \tag{2C.15}$$

where κ is an anisotropic factor intended to model equilibrium within the z dimension of the electrode.

2.8.3.3 C.3 Interface Current Flux

The current from the electrode reaction can be defined as

$$i_z = \left(\frac{1}{R_{\text{elc}}} + C\,\frac{\partial}{\partial t}\right)(\phi_1 - \phi) \tag{2C.16}$$

which can be non-dimensionalized to

$$i_z = \frac{\phi_o}{R_{\text{elc}}}\left(1 + \frac{\partial}{\partial \tau}\right)(\psi_1 - \psi) \tag{2C.17}$$

Removing time and scaling current density,

$$\overline{N}_\zeta = \left(\overline{\psi}_1 - \overline{\psi}\right)(1 + j\sigma) \tag{2C.18}$$

Chapter 3. DEVELOPMENT OF FREQUENCY RESOLVED MASS SPECTROMETRY

3.1 BACKGROUND

Co-electrolysis of water and CO_2 into CO and H_2 is recognized as a promising tool for storing energy and producing synthetic commodity chemicals via renewable electricity. Many excellent reviews are available on the subject regarding the last decade of progress.[12,13,17,39,56,57] The reviews detail the progress of materials development, balance of plant, stack development, economic feasibility, and multiple methods of water and CO_2 reduction including solar, thermal, and low and high temperature electrolysis. High temperature electrolysis in solid oxide electrolysis cells (SOEC) is one of the most promising technologies for this application because the high temperature helps overcome kinetic limtiations[12,13].

Solid oxide electrolysis cells are usually characterized between operating temperatures of 600 and 900 ºC and consist of an anode, electrolyte, and cathode. These are often $La_{1-x}Sr_xMnO_{3-\delta}$ (LSCM), yttria stabilized zirconia (YSZ), and a cermet of nickel and YSZ (Ni-YSZ)[15], respectively. Air or oxygen flows over the anode, and a reducing gas composition of hydrogen, carbon dioxide, carbon monoxide, and water mixed with a diluent of argon, helium, or nitrogen flows over the cathode. Often these systems are studied as individual cells with geometric areas on the order of tenths to tens of cm^2 or stacks of these cells in either planar or tubular geometry. Under these temperatures and compositions, Ni faces many degradation pathways including carbon deposition, oxidation, poisoning, and particle agglomeration[13,18,19,34]. Each pathway results in loss of active sites. Ni-YSZ's kinetic activity still merits further research, however; challenges with stability spur investigations into alternatives, many of which include metal oxides[56].

Commonly, cell performance is characterized with electrochemical techniques such as electrochemical impedance spectroscopy (EIS), distribution of relaxation times, cyclic voltammetry, and measurements of gas production using mass spectrometry or gas chromatography. The common reactions studied are water electrolysis, CO_2 electrolysis, methane production, and reverse water gas shift (RWGS). The reader is pointed to the previously cited reviews for more information encompassing the many facets of SOEC development.

Within the literature, there lacks a clear understanding of the degree to which CO is produced by CO_2 electrolysis or RWGS during co-electrolysis[56,58]. Multiple studies suggest that CO_2 electrolysis contributes little to the production of CO, which, consequently, is dominated by RWGS[19,31,33,34,59–66]. In many of these studies, the area specific resistance (ASR) of co-electrolysis and water electrolysis are nearly indistinguishable around open circuit voltage in both EIS and voltammograms, whereas the ASR of CO_2 electrolysis is larger than both co-electrolysis and water electrolysis. Some studies suggest that co-electrolysis and RWGS both significantly contribute[32,35,67–70]. In these studies, oftentimes the performance of co-electrolysis during EIS or cyclic voltammetry falls between that of solo water and CO_2 electrolysis. RWGS equilibrium is achieved in nearly all studies that involve gas composition analysis.

The complexity introduced by thermodynamics, geometry, flow rates, inlet gas composition, temperatures, mass transport, and multiple reaction pathways is credited with the discrepancy[35,36,58,59,61,63,71,72]. For example, some studies conclude that RWGS contributes throughout the electrode at different rates depending on temperature and composition as a function of electrode depth; this could result in the consumption of CO from the WGS[36]. A study on a composite electrode of LSCM and gadolinium doped ceria (GDC) found that CO_2, water, and co-electrolysis performed similarly around OCV, but attributed the poor performance of water electrolysis to low water concentrations resulting from resistance from mass transport[67]. At high current densities (requiring higher overpotentials), it is thought that CO_2 electrolysis starts to compete with RWGS in the production of CO. The performance of CO_2 electrolysis is reduced by the slower mass transport of CO_2 and higher activation energy of reaction[33]. Any degradation of the electrode, such as Ni-YSZ, that changes the electrode microstructure could affect the mass transport limitations of water or CO_2.[33]

Ebbesen and co-workers highlight the need to consider mass transport limitations when comparing performance. They conclude that if mass transport limitations are compensated for when comparing water, CO_2, and co-electrolysis, then there is evidence that CO_2 electrolysis significantly contributes to CO production.[35] Bessler dives deeper into highlighting the need to consider mass transport in SOFC and SOEC systems. Bessler uses Butler-Volmer kinetics of H_2O/H_2 redox and a stagnation point flow model to show how the shape, peak frequency, and size of low frequency arcs in impedance spectra can be affected by mass transport, even with constant kinetics[72]. Parameters such as overpotential, mass velocity, AC amplitude, reference electrode placement, inlet tube distance from electrode surface, temperature, and inlet mole fractions can significantly alter the interpretation of impedance spectra. Lastly, Chapter 2 has shown how improper current collection alters the interpretation of impedance spectra. A large enough sheet resistance could result in a Gerischer-like behavior, which implies combined mass transfer and kinetic limitations, when no mass transport limitations exist.

Alternative characterization techniques are needed to address this lack of understanding regarding the mechanism of CO production. Recently, Chueh and co-workers used ambient pressure photoelectron spectroscopy to reveal that the surface of doped ceria is more reduced than the bulk under water and hydrogen atmospheres[73]. Similarly, Feng and co-workers used the same technique to show how surface species and surface ceria oxidation state change as a function of polarization. Their work revealed that electron transfer between carbonate and ceria is likely rate limiting[74]. Hauser and co-workers demonstrated combined Diffuse Reflectance FT-IR spectroscopy and AC and DC electrochemical characterization techniques for understanding the activity of surface species during CO_2 electrolysis[75]. Gerwe and co-workers directly measured the fluctuation in cobalt oxidation state using X-ray absorption spectroscopy under AC perturbations[76]. Here, a novel technique is introduced to further investigate the nature of reactions on SOEC electrodes: Frequency Resolved Mass Spectrometry (FRMS).

In short, FRMS is an operando technique that measures the frequency response of the partial pressures of relevant gas species as a voltage or current perturbation is simultaneously applied to the electrochemical cell. Here, this technique is demonstrated using co-electrolysis on 10% doped gadolinium doped ceria $Gd_{0.10}Ce_{0.90}O_{1.95-\delta}$ (GDC10) as the working electrode because of its superior stability to Ni-YSZ[77] in carbonaceous and reducing environments. To the best of the author's knowledge, this is the first investigation of co-electrolysis on GDC10 as the working electrode. A better understanding of co-electrolysis mechanisms promotes a more focused effort on optimization and discovery of novel electrodes for SOEC development.

3.2 TECHNIQUE OUTLINE

The key aspect of FRMS is the ability to identify gas phase species time correlations with faradaic current and with each other at multiple frequencies of interest as identified by EIS. In this investigation, co-electrolysis of CO_2 and water was used to demonstrate the potential of this technique. Figure 3.1a displays a typical button SOEC comprising a cathode for electroreduction of CO_2 and H_2O, an oxygen ion conducting electrolyte, and an anode where O_2 is produced. As shown in Figure 3.1b, electroreduction of CO_2 and H_2O is thought to occur via three overall reactions at the temperature probed in this study: H_2O electrolysis, direct CO_2 electrolysis, and conversion of CO_2 to CO *via* RWGS.

As illustrated in Figure 3.1c, the FRMS approach involves studying the ***time-correlation*** between current fluctuations and fluctuations in gas phase partial pressures as a function of frequency. For example, consider a scenario in which the electrocatalyst is active for both H_2O and CO_2 electrolysis. As shown in Figure 3.1c, the CO, H_2, H_2O, and CO_2 partial pressures, which are all related to faradaic current, would be expected to be ±90 degrees out of phase with the current fluctuation. As shown with the dotted lines, peak current aligns with peak H_2 and CO production while minimum current aligns with peak CO_2 and H_2O production. If RWGS were very fast and CO_2 electrolysis inactive, the same result would occur because RWGS would instantly consume H_2 and CO_2 to make CO and H_2O. In contrast, if CO_2 electrolysis were uncompetitive with water electrolysis and RWGS and RWGS slower than water electrolysis, the peak CO_2 consumption (dCO_2/dt) would occur at peak H_2 partial pressure. These time correlations at various frequencies and conditions could provide key insights not afforded by EIS alone.

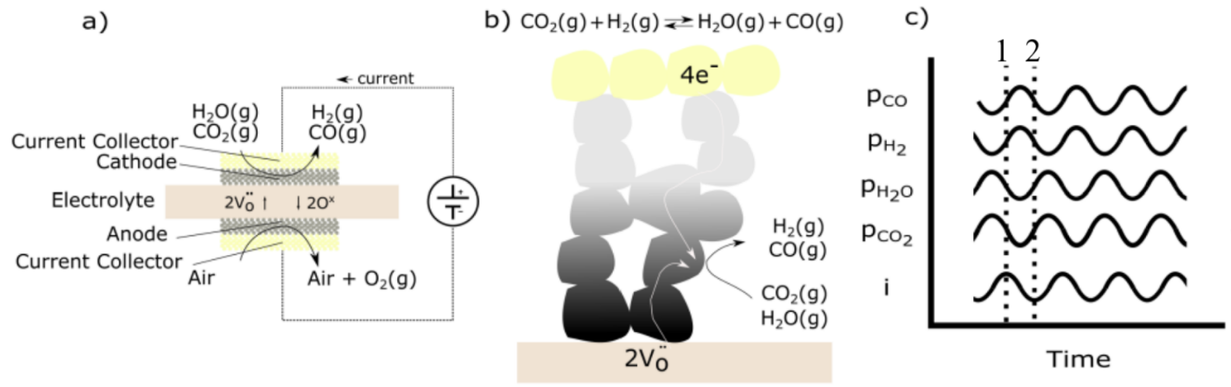

Figure 3.1. (a) Schematic of typical button cell setup with symmetrical porous electrodes and porous current collector; (b) illustration of co-electrolysis with the RWGS; (c) time correlated partial pressures of species. Dotted line 1 shows peak current aligned with maximum production rate of H_2 and CO and with maximum consumption rate of CO_2 and H_2O. Dotted line 2 shows minimum current aligned with maximum consumption of H_2 and CO and with maximum production rate of CO_2 and H_2O.

3.3 DESCRIPTION OF APPARATUS

A diagram of the experimental apparatus is shown in Figure 3.2. The cathode was placed in a moderate vacuum with a base pressure of 0.01 Torr, while the anode was at atmospheric pressure. Vacuum was maintained with a roughing pump (Precision Vacuum Pump Model D25) with a pumping speed at the inlet of 19.8 L/min at 10^{-3} Torr. Pressure and flow rate into the reactor were controlled by either pressure differentials across needle valves (V1–V5) or mass flow controllers (MFC). Valves V6 through V10 were on/off valves used to isolate the feedline. One MFC was used to maintain flow of gas. The MKS MFC controller was controlled by a MKS four-channel flow controller power supply and readout (MKS Type 247) with gas correction factors set to 0.7 for CO_2 and 1.0 for mixture diluted with N_2.

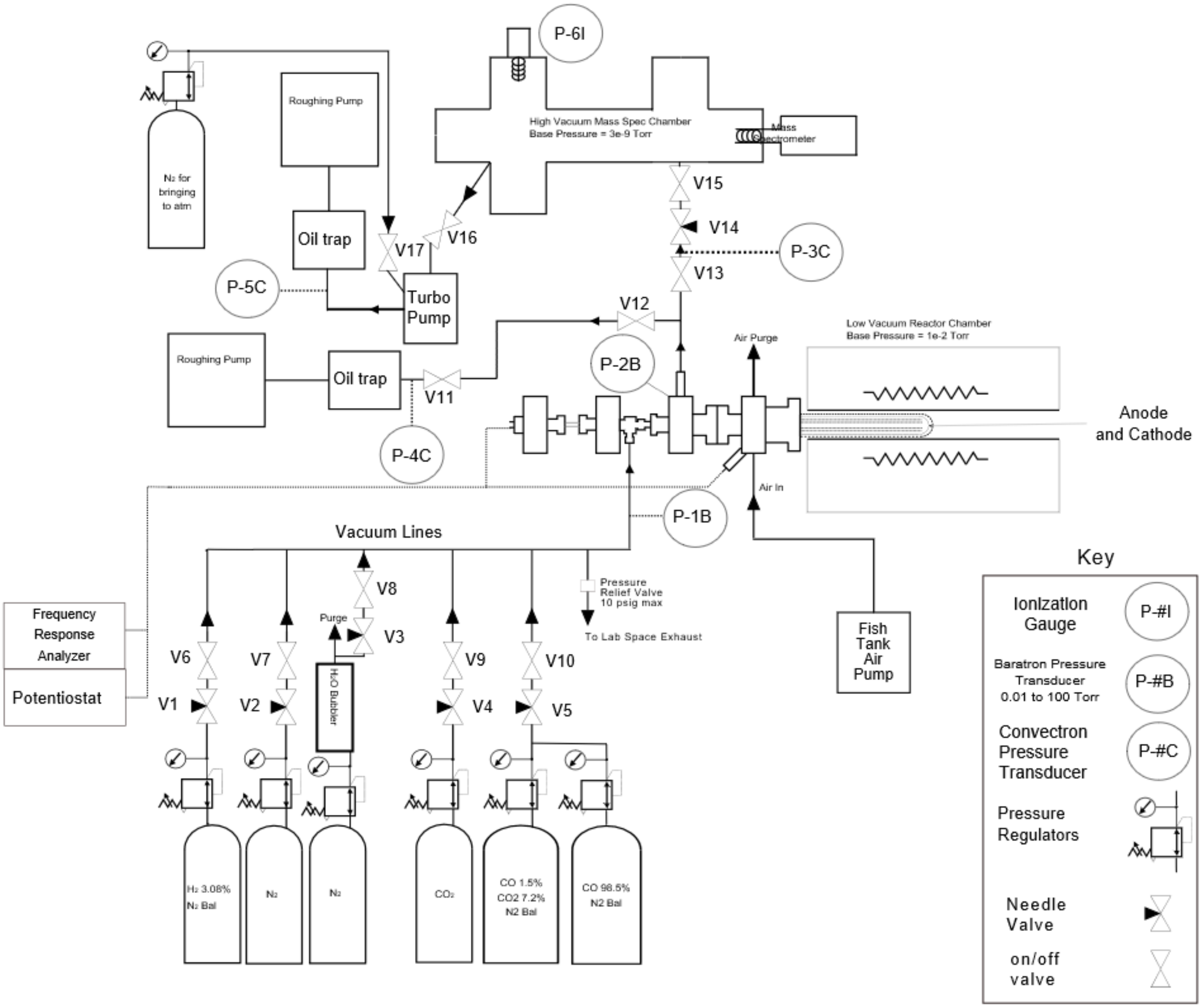

Figure 3.2. Schematic of complete apparatus.

Flow composition was either controlled by needle valves (V1–V5) or by MFCs (not shown). Five gas cylinders (Praxair) were available with the following compositions: 98.5% CO (balance N_2), pure CO_2, 3% H_2 (balance N_2), 100% H_2, and a premix of $CO/CO_2/N_2$ (1.5%, 7.2%, balance N_2). Water content was controlled by flowing any gas through a temperature-controlled bubbler of distilled water. The feed lines were not heated, and thus, the maximum water composition was dependent on room temperature and was determined by the Antoine Equation.

All gas feed lines but the one carrying concentrated CO were under high pressure and consisted of linear low density polyethylene tubes with inside wall thickness of 0.040 inches (Grainger) and metal Swagelok fittings. For safety, the high concentration CO line was quarter-inch stainless steel tubing connected to a needle valve (V5). Half of the needle valves (V1–V5) had VCR fittings and the other half had Swagelok fittings. Valves V6–V10 all either have VCR fittings or adapters to VCR from Swagelok. Downstream of V6–V10, a combination of VCR, Kwik-flanges, Conflat flanges with copper gaskets, Swagelok Ultra-Torr fittings, and MDC Quick-Disconnects were used to connect stainless steel tubing to both roughing pumps.

Needle valve V14 enabled continuous sampling of the vacuum reaction chamber. V15 was a right-angle valve, and V16 was an ultra-high vacuum gate valve. Both were necessary for complete isolation of the mass spectrometer (MS) chamber. A turbo pump operating at 62,000 RPM and a roughing pump (Edwards E2M2) maintained a base pressure of approximately 2×10^{-9} Torr when V15 was closed. This pressure was achieved without baking the chamber. If electricity was lost to the MS chamber's pumps, valve V17 would open and supply nitrogen to the chamber to slow contamination by air. The nitrogen enters midway through the turbopump blades.

The mass spectrometer chamber consisted of eight ports, two of which were used for an inlet and outlet, one for a Granville-Phillips ionization gauge, one for the Stanford Research 100 Systems MS, with the others closed. The ionization gauge monitored the total pressure within the chamber. The MS measured mass-to-charge (m/e) ratios up to 100. The electron current was set to 1.00 mA. Analog measurements were used to characterize a steady state composition of the feed to the high vacuum chamber. Masses 2, 14, 28, 18, 32, and 44 were monitored as a function of time. The mass spectrometer was controlled either by LabView or an accompanying SRS software program.

Figure 3.3 presents the reaction chamber in more detail. Three ceramic tubes telescopically comprised the cathode chamber. Two were alumina and the third was made of YSZ, acting as the electrolyte. The smallest alumina tube was a 60 cm quad-bore tube with 1/8-inch outer diameter (OD) and 0.031-inch inner diameter (ID) (99.8% alumina, McDanel Advanced Ceramic Technologies). The second largest tube, into which the previous one telescopically fit, was 40 cm long with a single bore OD of 0.375 inches and ID 0.250 inches (99.8 % Alumina, Coorstek, material AD-998). The largest ceramic tube, into which the two previous ones telescopically fit, was 35 cm long, 0.5 inches ID, 0.75 inches OD, and made of YSZ (10.5% doped Yttria, McDanel Advanced Ceramic Technologies, part number Z15). The YSZ tube was closed on one end, at which the anode and cathode were painted. The glass tube, made of quartz, was 25 cm long with an ID of 3.70 inches and OD of 4.00 inches for much of its length (Technical Glass Products). It was closed on one end. The open end of the quartz tube had an OD of 4.13 inches to fit into an MDC Quick Disconnect fitting.

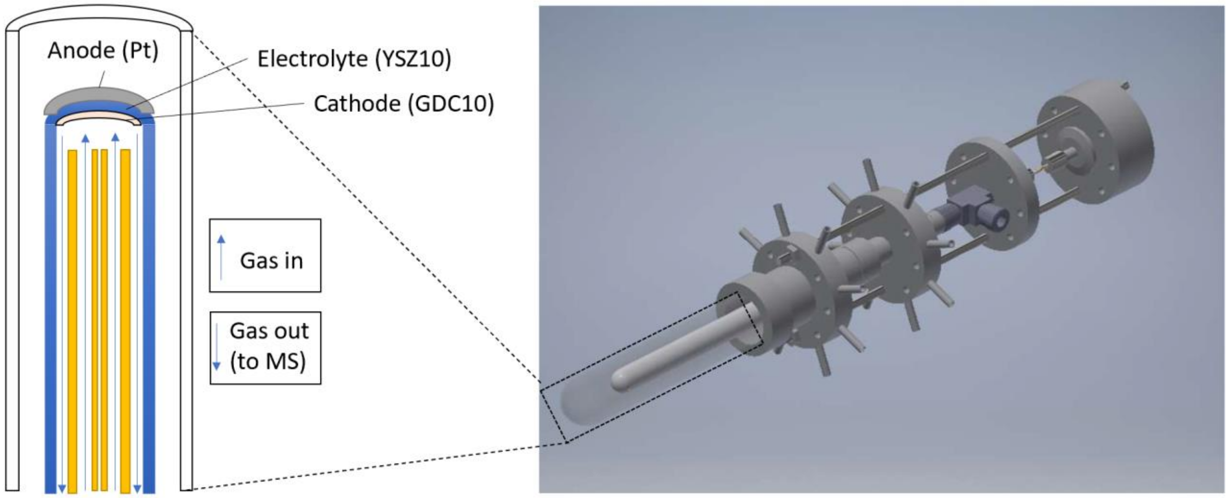

Figure 3.3. Schematic of reaction chamber. A quartz glass tube contains the anode. Within the electrolyte tube (blue) the GDC10 electrode rests. Gas is delivered from alumina tubes.

Figure 3.3 highlights the custom-made stainless-steel spine that holds the ceramic tubes together and separates the flow paths. There are four metal pieces. Each side of each metal piece had an MDC Quick Disconnect or Ultra-Torr fitting that was welded together by the University of Washington Physics Machine Shop. The first fitting sealed the anode atmosphere from that of the cathode atmosphere. The second fitting allowed the largest alumina tube to deliver gas directly to the cathode. Both fittings had multiple inlet and outlet tubes, providing opportunities to use Ultra-Torr fittings to attach pressure gauges, plugs, inlet and outlet tubing, and electric feedthroughs. The third fitting allowed gas to be fed in and provided an opening for an electric and thermocouple feedthrough. The fourth metal piece provided the feedthrough of gold wire through the smallest alumina tube. Two metal support rods extended through all the fittings to reduce stress on the fragile ceramic tubes. For the results presented here, the quartz tube was removed, and the anode was placed in air.

3.3.1 *Electrodes*

A porous GDC10 (fuelcellmaterials.com, GDC10-TC, 6.1 m^2/g) electrode was painted on the inside tip of the YSZ10 tube. A custom-made applicator was used to extend a commercial circular-tipped paint brush to reach the bottom of the tube and paint just the bottom of the tube. The ink was a 50 wt% organic solution of alpha-terpineol (Alfa Aesar 95% min), ethyl cellulose (Aldrich Chemical Company, Inc – Ethoxy content 48%), and oleic acid (Alfa Aesar Technical Grade) and 50 wt% GDC10. To make the ink, 18.3 g of alpha-terpineol, 1.6 g of ethyl cellulose, and 0.1 g of oleic acid were stirred together for 5-6 hours, then left to sit for two to three days. Equal weight of GDC10 was then added and stirred in with the mixture. The slurry was then roll milled with a spacing of 0.152 mm. The smooth ink collected from the roll mill was used immediately for painting.

After drying vertically overnight, the GDC10 electrodes underwent the following sintering protocol: 2 ºC/min to 670 ºC, hold for 1 hour, 2 ºC/min to 1151 ºC, hold for 2 hours, then 2 ºC/min to room temperature. Two aquarium pumps blew air into the tube furnace during sintering for all protocols. Based on previous work done by Green and Adler[48], the porosity was estimated to be 50%, and the tortuosity 1.5. It is difficult to assess the thickness of the electrode after sintering in the YSZ tube. Thus, cylindrical YSZ pellets were painted using the same method and imaged with an SEM. Four cells were imaged, one of which is shown in Figure 3.4. The thickness varied from 2 to 11 microns and was not uniform across the surface in many cases. The thickness likely varied based on brush stroke, amount of ink absorbed into the brush, and geometry. The effective area of the GDC10 electrode was approximately 1.15 cm^2 based on EIS and YSZ10 ionic conductivity at 800 ºC[14].

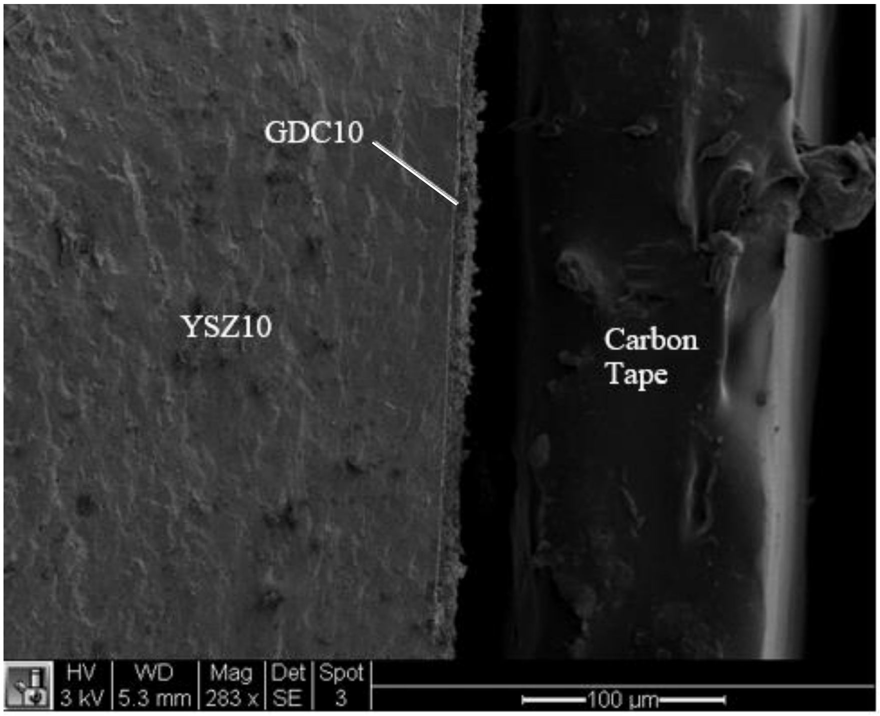

Figure 3.4. SEM of painted porous GDC10 electrode on YSZ10 pellet.

After the GDC10 sintering procedure, the anode was painted with Pt ink from Engelhard, part number A6016XD. The outside tip of the cell was painted to about 1 cm beyond the tip with one coat of Pt ink. The anode was vertically air-dried overnight *via* natural convection. Afterwards, the Pt was sintered. The sintering protocol was 1 ºC/min to 95 ºC, hold 2 hours, 1 ºC/min to 287 ºC, hold 4 hours, 1 ºC/min to 1084 ºC, hold 2 hours, and cool 2 ºC/min to room temperature. A spring-loaded ceramic plate held the gold mesh against the anode.

Gold ink was sintered on top of GDC10 as a current collecting layer. The ink was a mixture of dried gold ink from fuelcellmaterials and the organic ink mix described above. The gold ink from fuelcellmaterials originally contained a minimum of 70 wt% Au and balance terpineol; the particle size was (D50) < 0.6 microns or APS of 0.5 microns. After air drying overnight, the sintering protocol was 1 ºC/min to 95 ºC, hold 2 hours, 1 ºC/min to 287 ºC, hold 4 hours, 1 ºC/min to 856 ºC, hold 2 hours, and cool 2 ºC/min to room temperature.

3.4 DATA ACQUISITION AND ANALYSIS TOOLS

Most tests were performed with 0.5 sccm of $CO/CO_2/N_2$ flow over two weeks. The reactor was set to 800 ºC. Electrochemical impedance spectroscopy was done using a Solartron 1260 Frequency Response Analyzer and a SI 1287 Solartron Potentiostat, sweeping between 300 kHz and 1 mHz at a 10, 70.71, 100, and 106 mV RMS amplitude using Scribner ZPlot®. These were two-point measurements with no reference electrode. Scribner CorrWare® was used to perform a voltage sweep from OCV to 1.6 V at 1 mV/s.

Single perturbations of the cell were conducted at 0.9, 1.05, and 1.41 V with amplitudes of 100, 150, and 137 mV. The Pt electrode was the positive electrode and GDC10 the negative electrode. Positive current is defined in this case as the standard definition: flow of current from the positive to the negative electrode. The Pt electrode was attached to the counter electrode and reference electrode 1 BNC slots of the SI 1287, while the GDC10 electrode was attached to the working electrode and reference electrode 2 BNC slots.

The potentiostat applied DC bias to the cell, while a frequency generator PCI card (NI PCI-5412) was used to generate a frequency and amplitude. The voltage and current across the cell were sampled at 5001 S/s by the digitizer (PCI–5122). The minimum sampling rate of 5001 S/s limited the number of perturbations that could be collected in one scan to a little under 1.85×10^8 samples before the computer faced RAM errors. In post processing, the voltage and current perturbations were down sampled to 100 samples per waveform to reduce memory allocation.

Voltage, current, and collection of masses 2, 18, 32, 44, 14, and 28 were saved to text files using a custom LabView program. The MS sampled a single mass once every 1.24 seconds. Each mass was collection sequentially. Each sample had it owns time stamp. The Nyquist limit for the MS was half the sampling rate, thus any perturbation frequencies above 0.405 Hz would have been aliased. Practically, it is a best practice to sample ten times faster than the maximum frequency of study. The LabView program was partially built using the SRS-provided LabView modules. Python module frXAS.py[78], written by colleague Dr. Brian Gerwe, was used to extract amplitudes and phase relationships of the measured signals.

3.5 RESULTS

3.5.1 *Open Circuit Voltage*

An initial measure of composition was found by measuring the OCV of the steady state flow. The steady state OCV was 0.248 V at a flow condition of 0.5 sccm $CO/CO_2/N_2$ (1.5%/7.2%/balance) which manifested in a 0.68 Torr vacuum within the reaction chamber. The expected open circuit voltage is determined by the Nernst equation,

$$V = \frac{RT}{nF} \ln\left(\frac{p_{\mathrm{O_2}}^{\mathrm{a}}}{K_{\mathrm{eq}}\left(\frac{p_{\mathrm{CO_2}}^{\mathrm{c}}}{p_{\mathrm{CO}}^{\mathrm{c}}}\right)^2} \right) \tag{3.1}$$

where *R* is the gas constant, *T* is temperature, *n* is the stoichiometry of electrons in

$$\mathrm{O_2(g)} + 4\mathrm{e}^- \rightleftharpoons 2\mathrm{O}^{2-} \tag{3.2}$$

F is Faraday's constant, $p_{\mathrm{O_2}}^{\mathrm{a}}$ is the oxygen partial pressure in the anode chamber (0.21 atm), K_{eq} is the equilibrium constant of the following reaction at temperature T,

$$2\mathrm{CO_2(g)} \rightleftharpoons 2\mathrm{CO(g)} + \mathrm{O_2(g)} \tag{3.3}$$

$p_{\mathrm{CO_2}}^{\mathrm{c}}$ is the cathode CO_2 partial pressure, and $p_{\mathrm{CO}}^{\mathrm{c}}$is the partial pressure of CO in the cathode chamber. At 1073 K, *n* of 4, $p_{\mathrm{CO_2}}^{\mathrm{c}}$ of 0.072, $p_{\mathrm{CO}}^{\mathrm{c}}$ of 0.015, and K_{eq} of $3.99995\text{x}10^{-19}$, the expected OCV was 0.871 V.

The measured OCV was far from the theoretical equilibrium open circuit voltage of 0.871 V for this fed gas composition. The effect of pressure on OCV was investigated. Pressure was controlled by increasing flow into the reaction chamber. The OCV at 3.63, 10.77, and 51.67 Torr was 0.871, 0.872, and 0.873 V, respectively. This evidence suggests that there is likely an air leak into the reaction chamber, perhaps either from the upstream high pressure flow pipes or within the vacuum system itself.

3.5.2 *Analog Mass Spectrometry*

An analog mass spectrum, see Figure 3.5, was taken with valve 15 (see Figure 3.2) closed, isolating the low-pressure chamber housing the MS from the rest of the vacuum apparatus. This spectrum characterized the natural contents of the MS chamber. Mass 2 (H_2) and mass 18 (H_2O) dominated, but there were also significant peaks of mass 28 (CO or N_2), 32 (O_2), and 44 (CO_2). Peaks will be referred to as M# for the remainder of the dissertation. The usual constituents of a high vacuum chamber are H_2, H_2O, CO, and CO_2[37]. However, the presence of oxygen indicates a leak into the mass spec chamber itself, however small it may be. The lack of peaks beyond M50 is the evidence for the lack of contamination from pump oil.

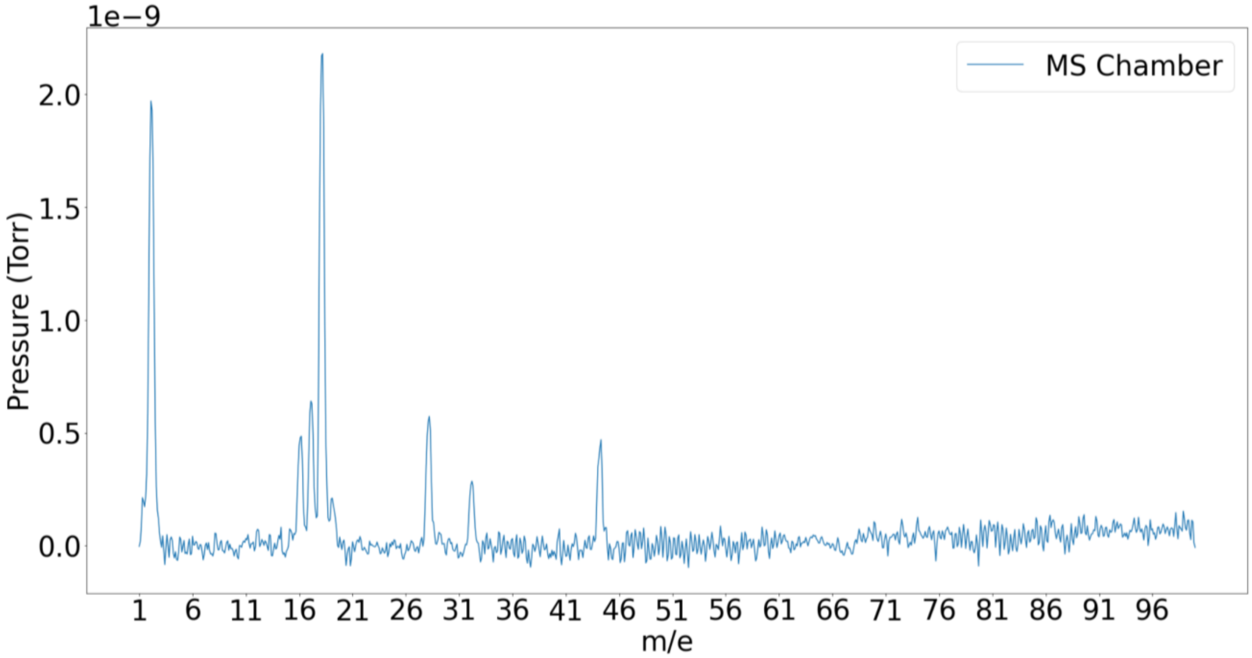

Figure 3.5. Mass spectrum of isolated MS chamber.

A second mass spectrum, see Figure 3.6, was taken with the MS open to the reactor without any intentional flow (V13–V15 open). The analog spectrum is superimposed on the previous spectrum where the MS chamber was isolated. The comparison showed a stark increase in hydrogen, water, nitrogen, oxygen, argon, and carbon dioxide. The large oxygen peak (M32) and argon peak (M40) provide further evidence of an air leak. M28 and M32 indicate a ratio of N_2 to O_2 of 7.31, which is approximately double the ratio of N_2 to O_2 in air. Some of the M28 peak may be from residual CO. Prior to the results presented here, preliminary studies were done with mixtures of water, H_2, N_2, CO_2, and CO. In addition to an air leak, there may have been virtual leaks, i.e., gases in difficult to access dead space, contributing to this second mass spectrum. It was unclear what contributed to the peaks at M39, M41, and M1. Though oil was suspected, the masses above M50 did not provide strong evidence of pump oil presence.

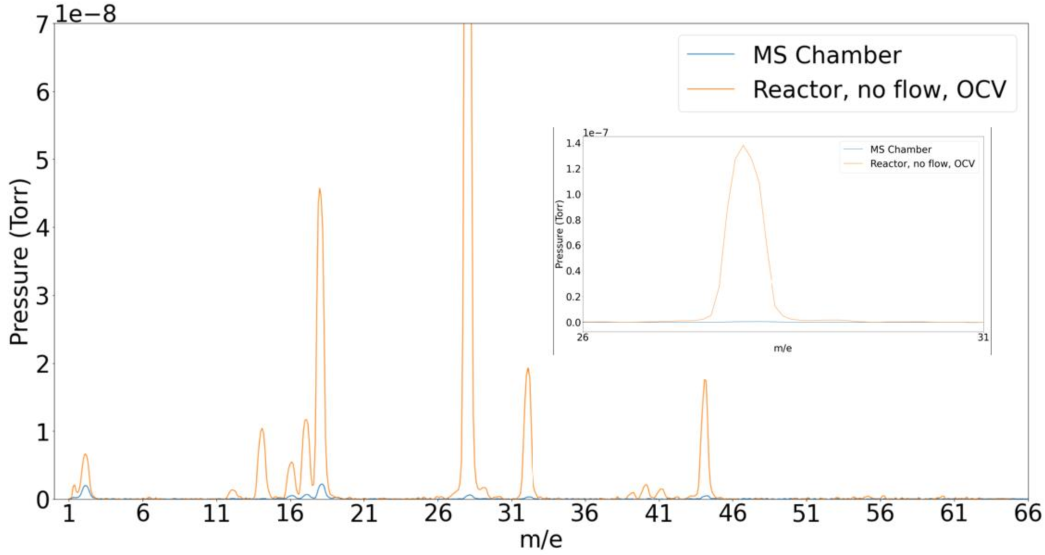

Figure 3.6. Mass spectrum superimposed on that of Figure 3.5 comparing the MS chamber to that of the reactor chamber without any flow at OCV. Inset shows M28.

A third spectrum with the flow of the $CO/CO_2/N_2$ gas superimposed onto the two previous spectra is shown in Figure 3.7. Hydrogen decreased back to nearly the amount that was measurable just within the MS chamber. Water content significantly decreased, oxygen slightly decreased, argon slightly decreased, nitrogen and CO_2 content significantly increased, the shoulder on hydrogen decreased, and M39 and M41 disappeared. The oxygen and argon still indicate a competitive leak. Hydrogen and water may have been flushed from the walls and dead space thanks to the flow. The spectrum was consistent with the composition of the flow since nitrogen content should dominate followed by CO_2.

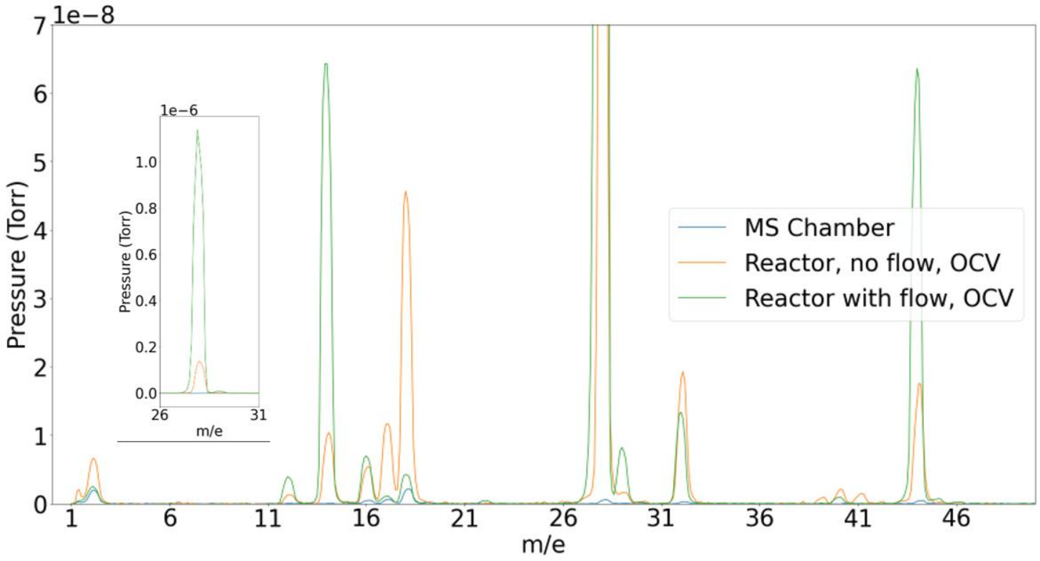

Figure 3.7. Mass spectrum comparing the MS chamber to that of the reactor chamber with and without any flow. Inset shows M28.

The spectrum with flow at OCV and the MS chamber spectrum were subtracted from each other to characterize the contents associated with the flow upstream of V13, see Figure 3.8. The spectrum was analyzed using standard fragmentation patterns, see Appendix A, and the default universal sensitivity factor of the MS. Table I displays the resulting mole fractions depending on the analysis method used to determine CO content. To summarize, the “M12” method uses the contributions of CO_2 and CO to M12 to determine CO content, the “M28 and M14” method uses N_2, CO, and CO_2 contributions to M14 and M28 to determine CO content, and the “M12 and M16” method uses contributions from O_2, H_2O, CO, and CO_2 to M12 and M16 to find the CO content. Other than CO content, the mole fractions appeared consistent with the composition of the inlet flow. All analysis cases yield significantly different CO contents.

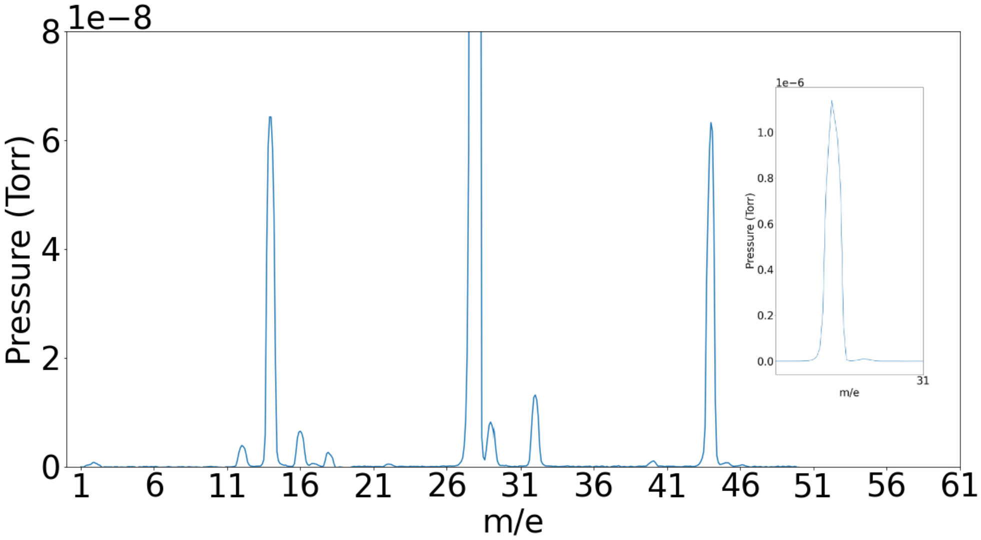

Figure 3.8. Mass spectrum representing the difference between a spectrum of the MS chamber and the spectrum with flow at OCV. Inset shows M28.

Table 3.4. Comparison of quantitative gas analysis from a mass spectrum using three different methods.

Gas	Mole Fraction	Mole Fraction	Mole Fraction
Analysis method	M12	M28 and M14	M12 and M16
N_2	0.904	0.756	0.915
CO_2	0.0756	0.0651	0.0508
O_2	0.0138	0.012	0.012
CO	0.0029	0.163	0.0177
H_2O	0.0029	0.0025	0.0026
H_2	0.00063	0.00054	0.00055
Argon	0.00102	0.00088	0.00089

The difference may stem from the fact that the sensitivity factors and fragmentation patterns specific to this MS have not been determined recently with pure gases in the absence of an oxygen leak. Either the “M12” or “M12 and M16” method seems to have the most reasonable mole fractions when considering the mole fractions of the inlet flow rate. Without this calibration, the MS is best for monitoring relative changes. The CO concentration was overall difficult to determine because all its signals *m*/*e* (28, 16, 12) are diluted by contributions from N_2 and CO_2, which have much larger inlet feed concentrations.

3.5.3 *Current-Voltage Curve*

Figure 3.9 shows the electrolysis mode I-V curve for the cell at 800 ^{0}C. The I-V curve was varied from OCV to 1.6 V, spanning a steady state current range of near 0 to 4.633 mA. Time correlated mass spectra of M2, M18, M32, M44 and M14 are superimposed on the I-V data. The early current appears to be associated with oxygen reduction until about 1.05 V. At 1.05 V, hydrogen starts to be produced. At 1.3 V it appears that CO_2 becomes more activated, and that hydrogen continues to be active as well. At about 1.4 V the hydrogen starts to plateau, and a little before 1.6 V, the mass transport limited current density is reached. The steepest slope, and therefore least resistive portion, occurs between 1.3 and 1.4 V.

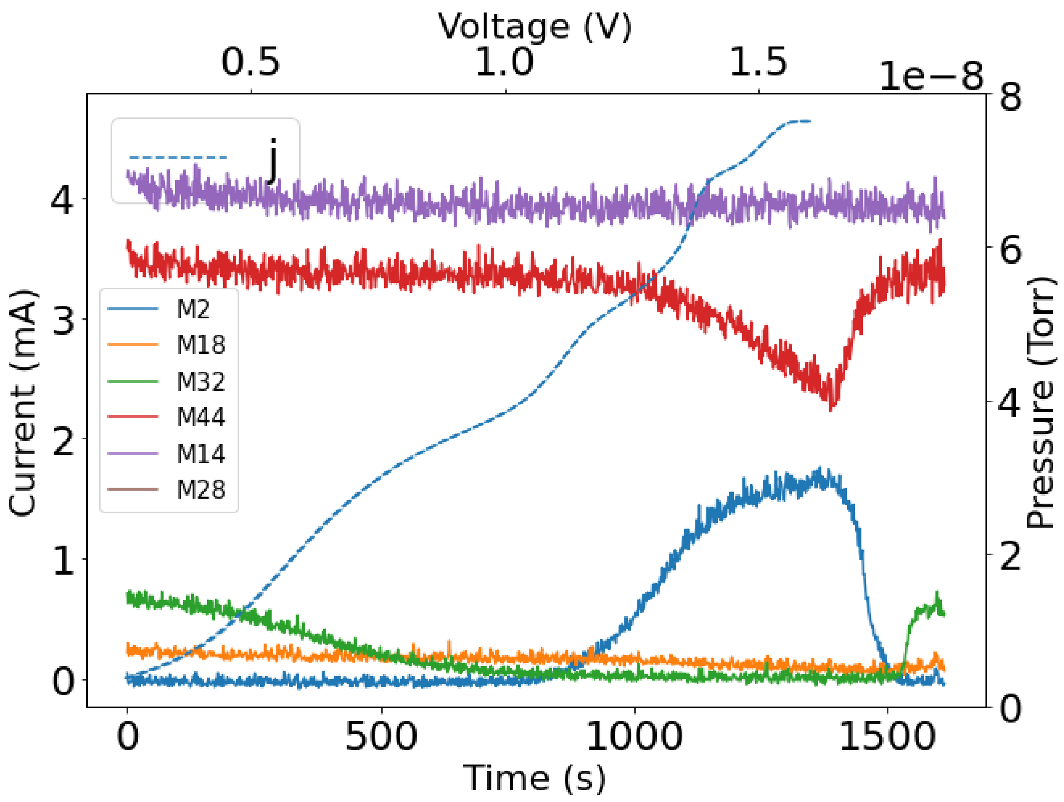

Figure 3.9. I-V curve from polarizing the cell at 1 mV/s. M2, M18, M32, M44, M14, and M28 (not shown) are time correlated with the voltage and current. The top x axis is voltage.

3.5.4 *EIS Results*

Three EIS curves at 0.9 V ± 150 mV, 1.05 V ± 150 mV, and 1.05 ± 100 mV are shown in Figure 3.10. A separate one at 1.41 V ± 137 mV is shown in Figure 3.11. Labeled are the frequencies at which FRMS was done, the peak frequency, and last frequency taken. There are two apparent arcs, a high frequency arc and a near semi-circular low frequency arc. The high frequency arc is common to all four spectra and has an arc width of 13 Ω. The width of the low frequency arc, the peak frequency, and the estimated capacitance for each DC and AC perturbation are presented in Table 3.5. Figure 3.12 shows that the phase angle for the low frequency arcs were similar and around 65-70^{o}.

Table 3.5. Observed EIS curve parameters.

Voltage	Low Frequency Arc Width (Ω)	Peak Frequency for Low Frequency Arc (mHz)	Estimated Capacitance of Low Frequency Arc (F)
0.90 V ± 150 mV	812.9	3.00	0.065
1.05 V ± 100 mV	833.42	0.501	0.381
1.05 V ± 150 mV	812.9	0.501	0.391
1.41 V ± 137 mV	199	1.00	0.800

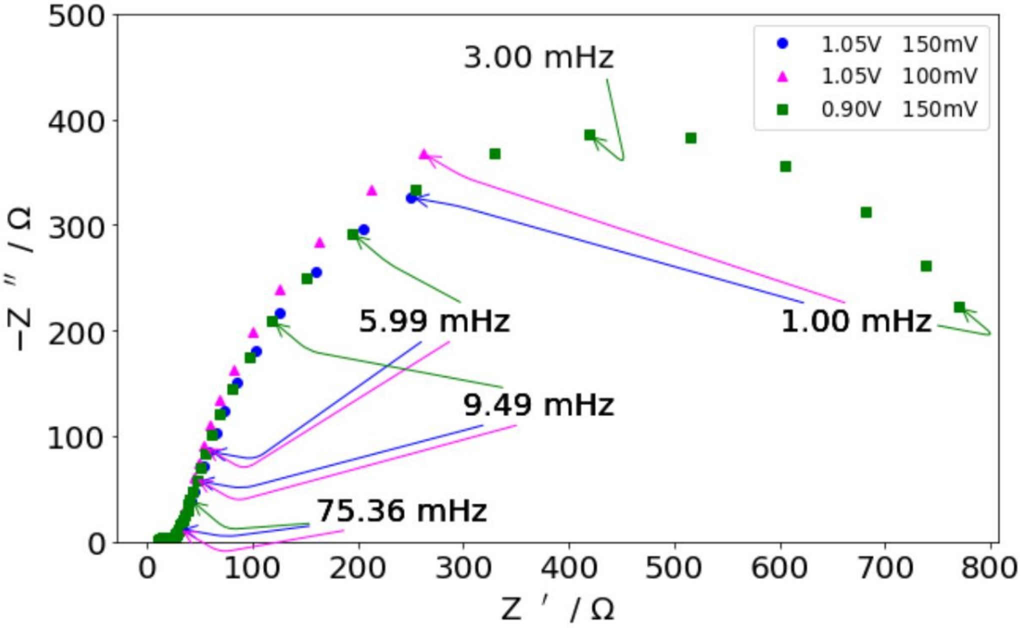

Figure 3.10. EIS spectrum for 0.90 V ± 150 mV, 1.05 V ± 100 mV, and 1.05 V ± 150 mV at 800 ºC.

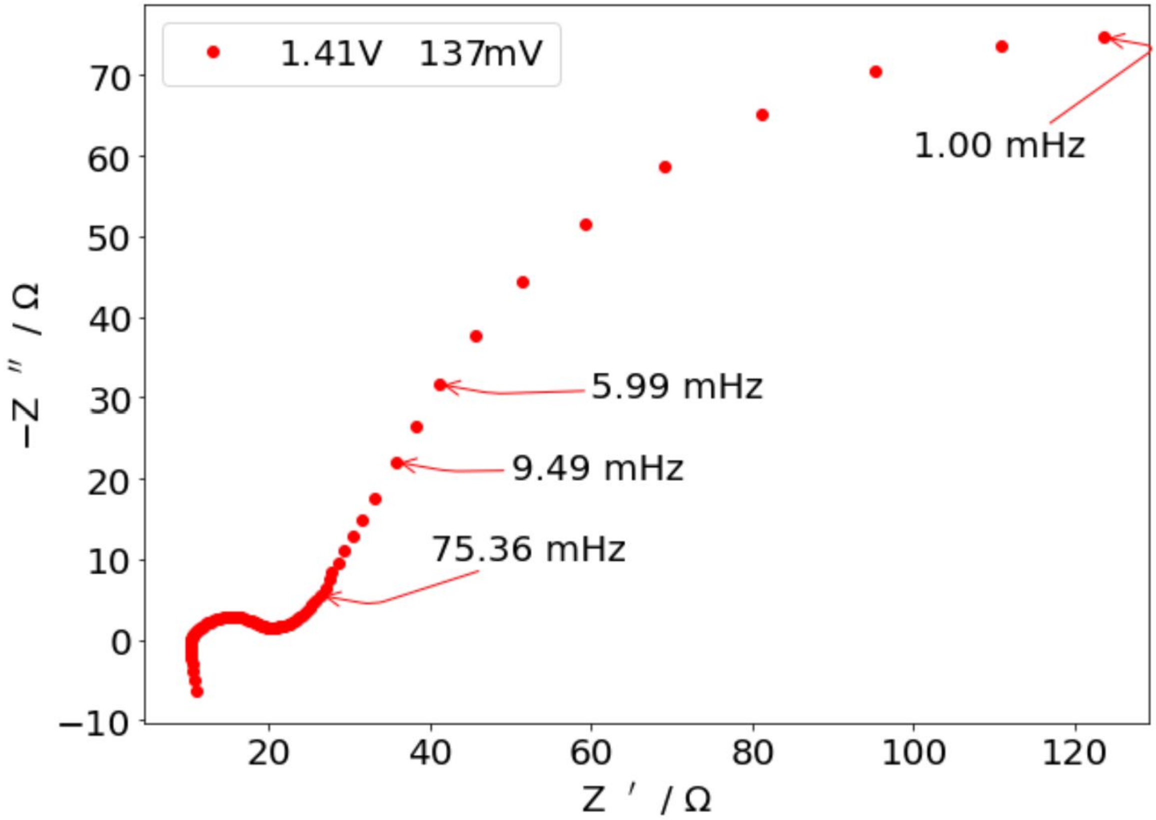

Figure 3.11. EIS spectrum for 1.41 V ± 137 mV at 800 ºC.

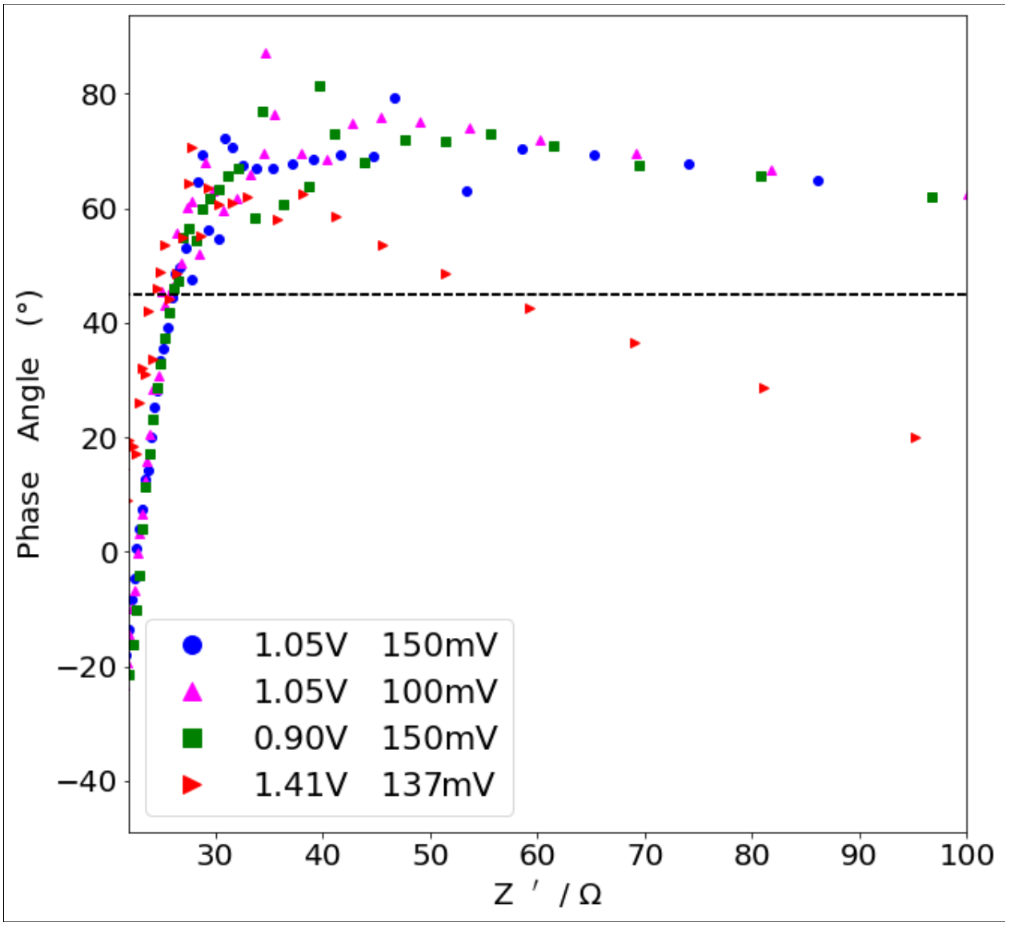

Figure 3.12. Phase angle for each spectrum between the high frequency arc and the beginning of the low frequency arc.

3.6 DISCUSSION OF TECHNIQUE DEVELOPMENT

A strength of this technique, and inherently in the FFT, is that small signals can be extracted from noise. Figure 3.13 shows six waveform time correlated comparisons between M18, M32, M44, M2, M14, and M28 and the current and voltage signal. All signals are from a 1.05 ± 150 mV perturbation collected over 369 waveforms. Among all the masses, it is only apparent that M2 is oscillating.

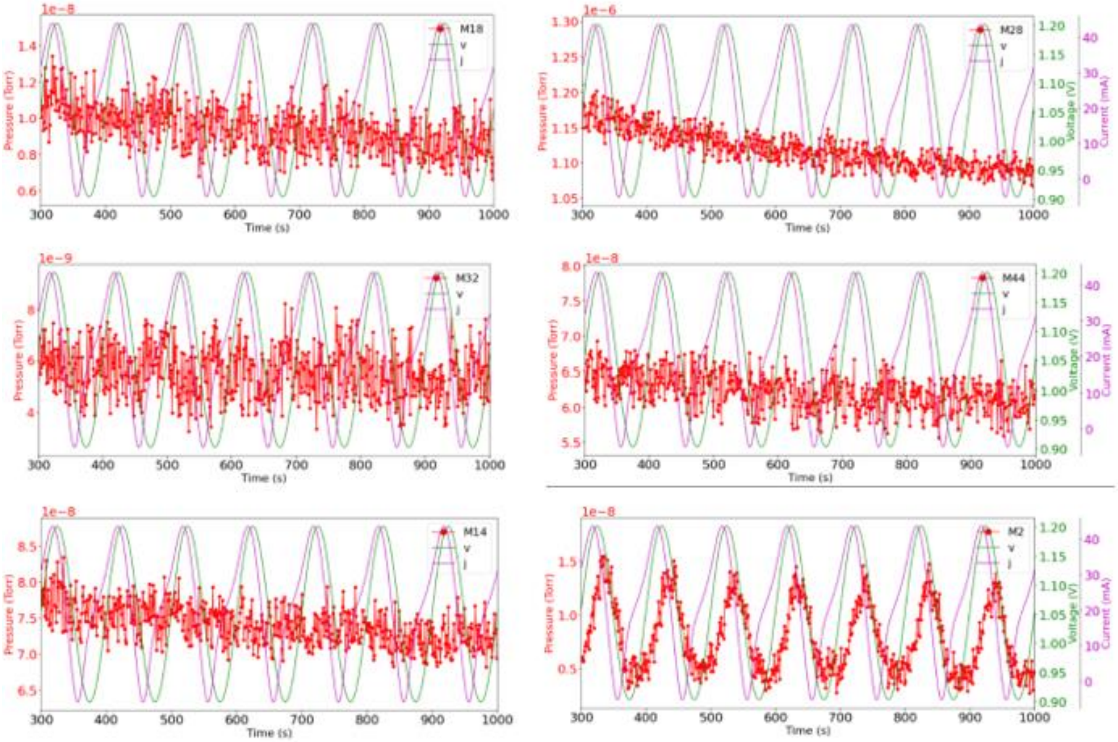

Figure 3.13. Time correlations of M2, M18, M28, M32, M44, M14 with current and voltage at 1.05 V ± 150 mV at 1 mHz.

However, after taking the Fourier transform of this data, it became clear that underneath the noisy signals are oxygen, carbon dioxide, and hydrogen signals at the perturbation frequency of 0.01 Hz. These can be seen in Figure 3.14. As expected, voltage has a single first order harmonic at 10 mHz, while current has up to five measurable harmonics. This exhibits another highlight of this technique: the ability to deconvolute higher order harmonics in the temporal mass data, which is not apparent in the temporal data itself. The 0th order harmonics are a result of a mean variation in the data. Looking at Figure 3.15, this is from a decaying signal for some species after time zero, lasting about 1000 seconds. It is unclear why this occurs; however, it is possibly because of outgassing from the MS filament turning on.

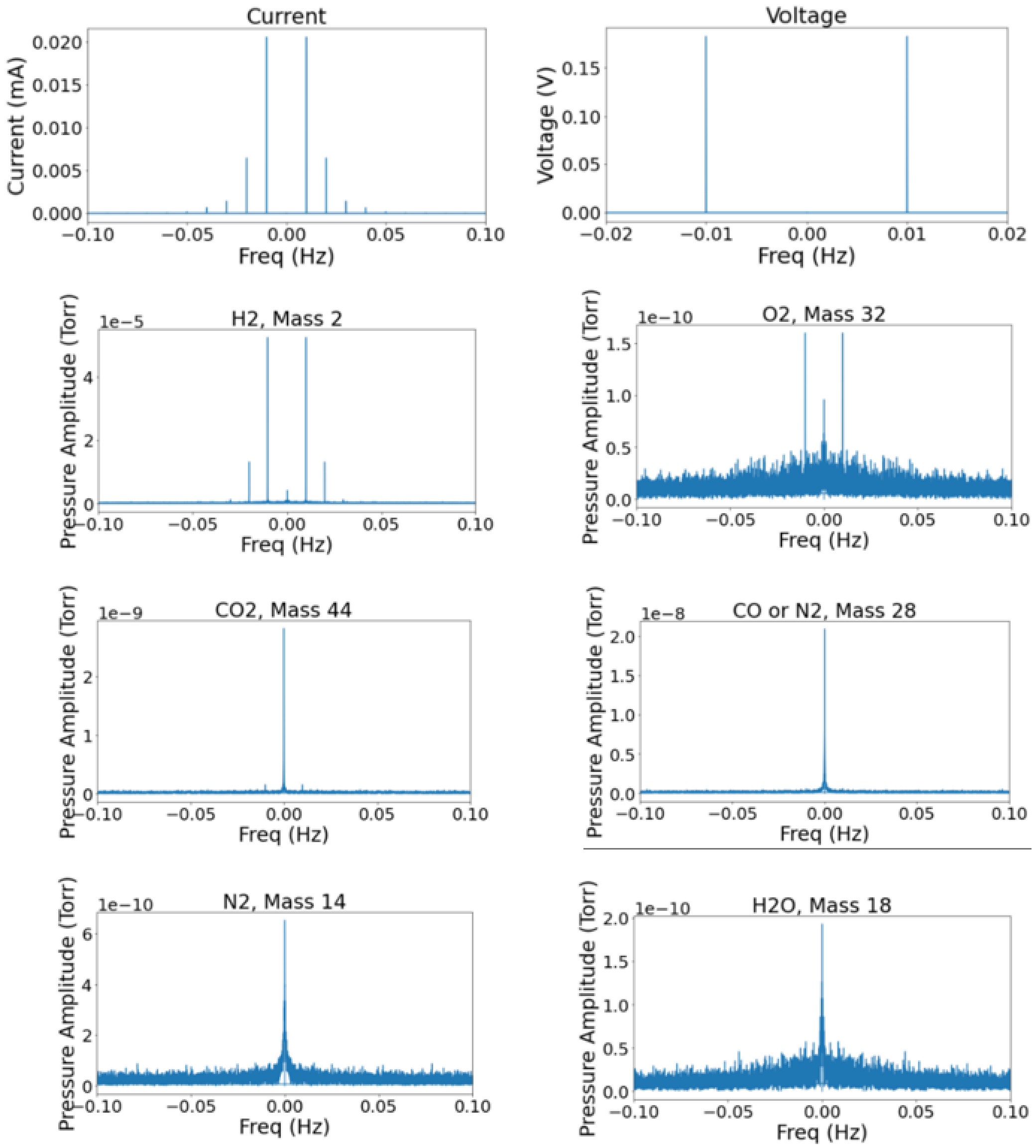

Figure 3.14. FFT of M2, M18, M28, M32, M44, M14 with current and voltage at 1.05 V ± 150 mV at 10 mHz.

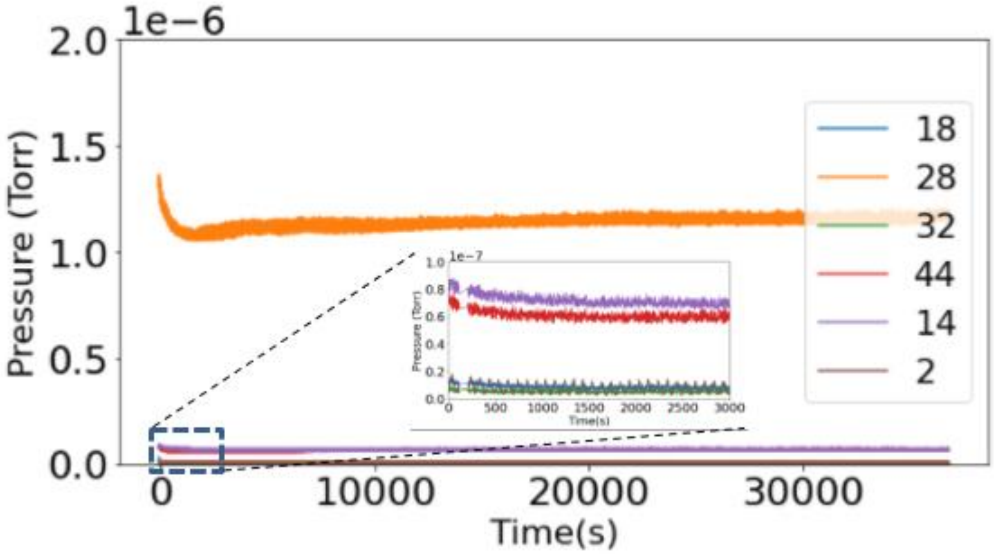

Figure 3.15. Time domain signal of M2, M18, M28, M32, M44, M14 with inset of masses smaller than M28. For 1.05 V ± 150 mV at 10 mHz.

Notably there are no peaks in M28, M14, nor M18. No peaks in M14 suggests no change in total pressure as nearly all M14 represents N_2 content. In all fluctuation experiments (not shown) there was no observable fluctuating signal for M14. M18, which represents water content, did not show any frequency peaks at 10 mHz, nor did it in any experiment. In Figure 3.9, it did, however, appear to slightly decrease after the activation of significant hydrogen production. It is likely that water is difficult to measure because the MS is not in line of sight with the cathode and water adsorbs strongly to walls of the vacuum chamber. The adsorption effect is suspected to have dampened any M18 fluctuations. It is likely that, given the weak signal of CO_2 at 10 mHz, there was not enough fluctuation in the M28 signal from a change in CO composition to register with the MS. This is because M28 is a combination of N_2 and CO of which CO likely contributes less than 1.5%. A 10% change in CO signal would only be a 0.15% change in the M28 signal.

Another strength of this technique is the ability to correlate gas phase observations with positions on an I-V curve and impedance spectrum. Figure 3.9 is reproduced here with guidelines to show where the impedance spectra of Figure 3.10 and Figure 3.11 were taken.

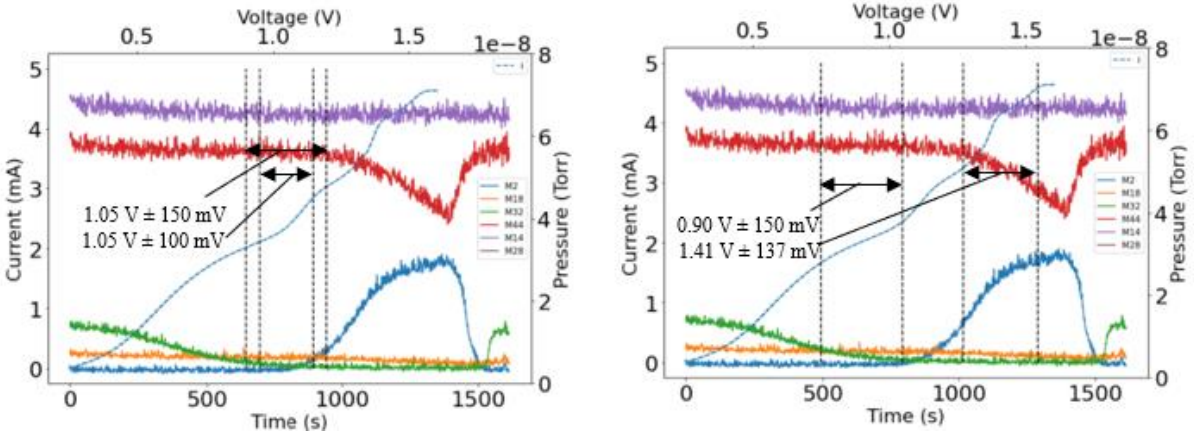

Figure 3.16. I-V curve at 1 mV/s superimposed with M2, M18, M44, M14, M28 (not shown), and M32 signals. Labeled guidelines show where EIS was measured. The figure on the left is the same as the figure on the right, but with different guidelines; done for clarity.

Examining CO_2 as an example, it would be expected for the CO_2 signal in the mass perturbations to grow from 0.9 V DC bias ± 150 mV AC to 1.41 V ± 137 mV AC. The graphs in Figure 3.17 show this to be true at a 6 mHz perturbation. There is no signal M44 signal at 0.9 V, which is dominated by oxygen reduction on the I-V curve. There is a significant increase by about a factor of 30 between 1.05 V ± 150 mV and 1.41 V ± 137 mV for M44.

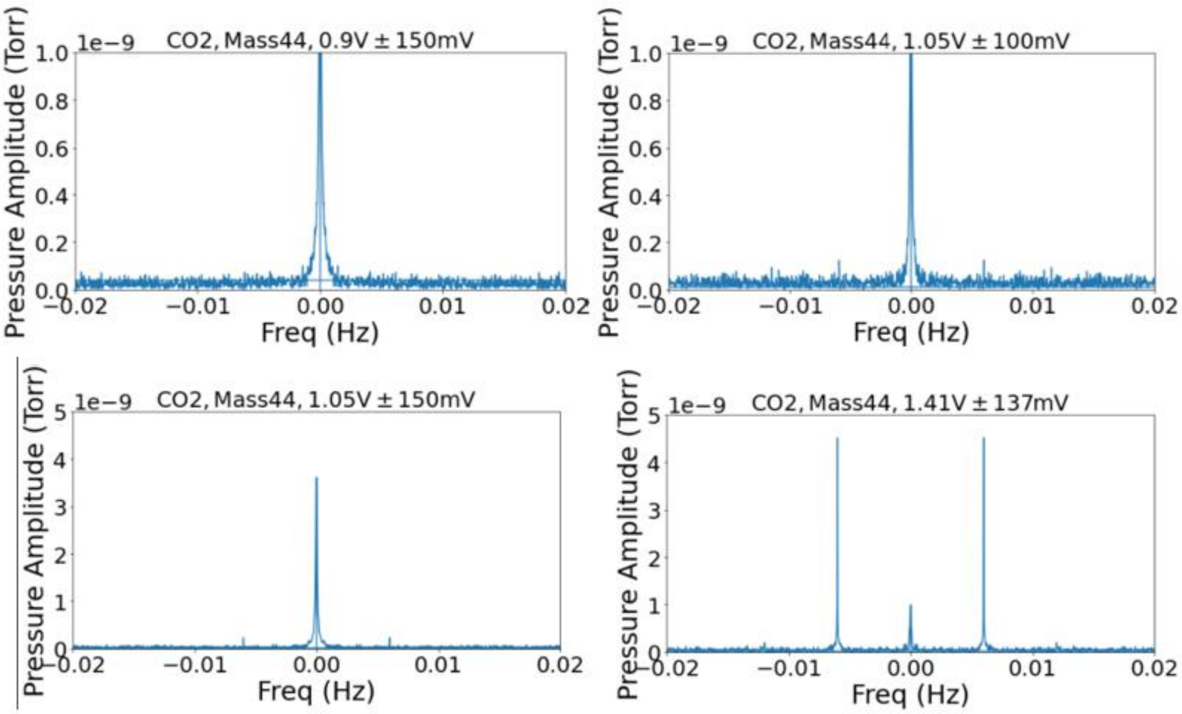

Figure 3.17. FFT of M44 at multiple DC and AC bias for 6 mHz perturbations.

Correlations with the impedance spectra demonstrate frequency dependence of the gas phase perturbations. Reconsider the positions of 6 mHz, 10 mHz, and 80 mHz on Figure 3.10 and Figure 3.11. At 1.05 V ± 150 mV, 6 and 10 mHz are significantly further up the low frequency arc than 80 mHz. Comparisons of the FFT graphs of M44 at these three frequencies are shown in Figure 3.18. 1.05 V ± 150 mV is enough overpotential to activate CO_2 reduction, but the signal is frequency dependent; the peaks at 6 mHz are slightly larger than those of 10 mHz. This is congruent with the difference in distance along the low frequency arc. At 80 mHz, an order of magnitude faster than 6 mHz, the CO_2 signal is erased all together. This evidence suggests the enhanced activation of CO_2 reduction is associated with the low frequency arc. Similar conclusions can be drawn for the comparison of the oxygen signal as shown in Figure 3.18. However, oxygen was still present at 80 mHz, perhaps indicating faster kinetics for oxygen reduction than CO_2 reduction at this condition.

The change in hydrogen from 6 mHz to 80 mHz is different from CO_2 and O_2 in three ways. The signals are roughly an order of magnitude larger than either CO_2 or O_2. Though it is unclear if this was because more was produced or because hydrogen's baseline was much smaller, and therefore, small changes in hydrogen concentration manifest in larger fluctuations. Secondly, hydrogen exhibits higher order harmonics at 10 and 6 mHz, mimicking the behavior of the current, which also has higher order harmonics. The significance of the higher order harmonics in a mass signal is outside the scope of this dissertation. The only time O_2 exhibited higher order was at 0.9 V ± 150 mV at 6 mHz. The only time CO_2 exhibited higher order harmonics was at 6 mHz at 1.41 V ± 137 mV. Thirdly, the hydrogen signal peaks at 10 mHz rather than 6 mHz, suggesting that the low frequency arc may be more associated with CO_2 reduction rather than water reduction at 1.05 V ± 150 mV. An alternative assessment is that, as CO_2 becomes more activated, more hydrogen is consumed in the RWGS reaction, lowering the perturbation amplitudes. Lastly, the hydrogen had a stronger presence at 80 mHz than CO_2. Perhaps this indicates faster kinetics for water reduction under these conditions despite the significantly larger amount of CO_2 present than water.

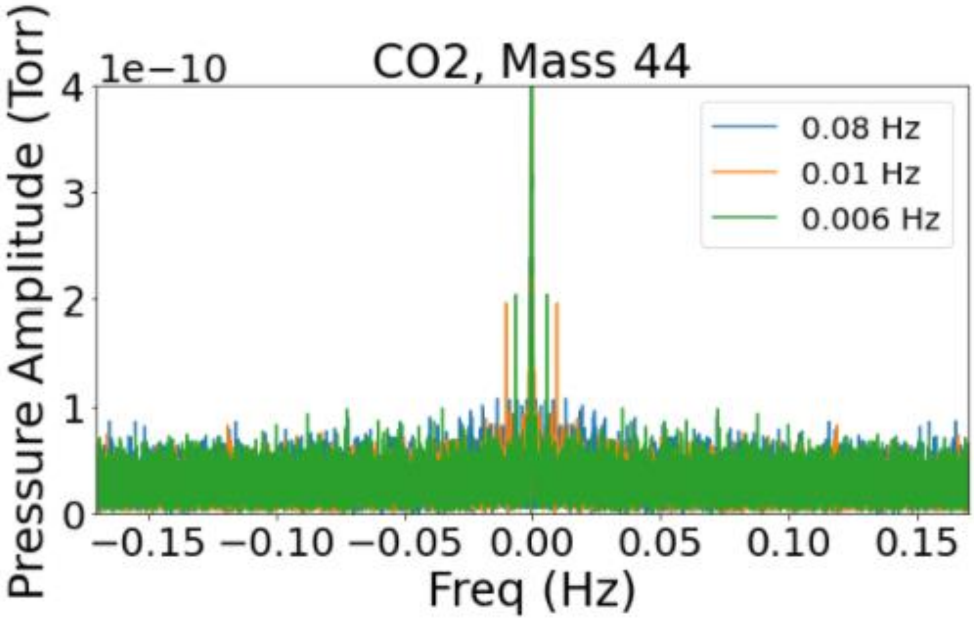
CO2, Mass 44
1e−10
Pressure Amplitude (Torr)
0
1
2
3
4
−0.15
−0.10
−0.05
0.00
0.05
0.10
0.15
Freq (Hz)
0.08 Hz
0.01 Hz
0.006 Hz

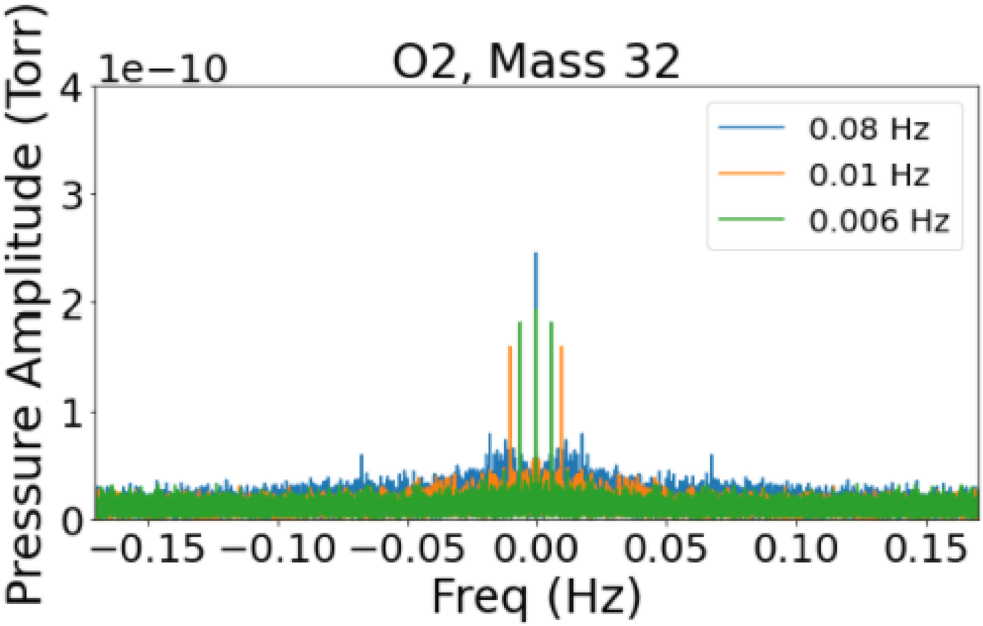
O2, Mass 32
1e−10
Pressure Amplitude (Torr)
0
1
2
3
4
−0.15
−0.10
−0.05
0.00
0.05
0.10
0.15
Freq (Hz)
0.08 Hz
0.01 Hz
0.006 Hz

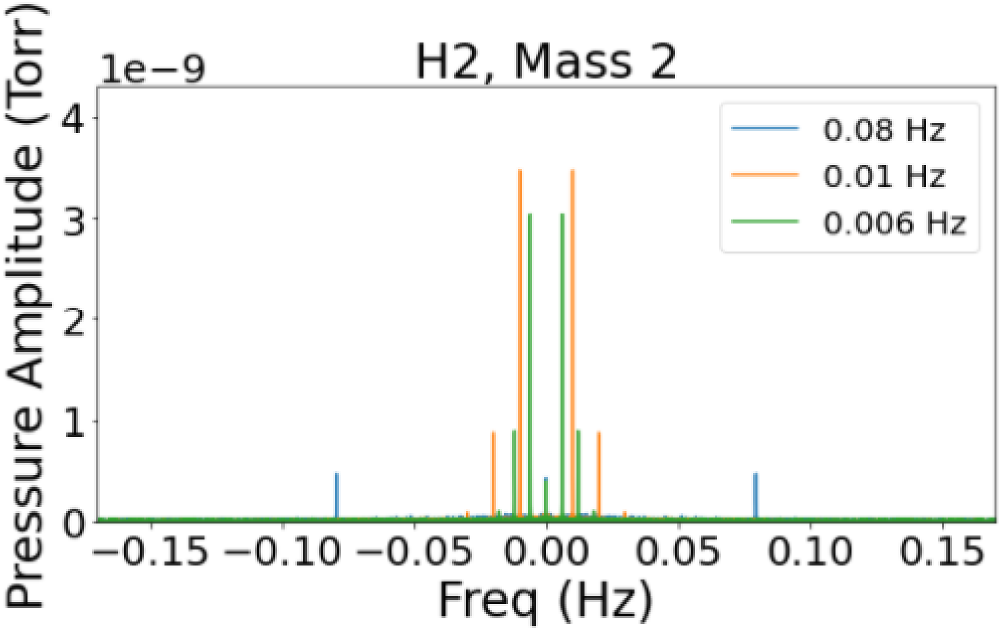

Figure 3.18. FFT of M44, M2, and M32 at multiple frequency perturbations (80, 10, and 6 mHz) at 1.05 V ± 150 mV.

Lastly, the most unique characteristic of FRMS is the ability to phase correlate the voltage, current, and mass signals providing yet another dimension of information. This is important because, from the I-V curve, it is difficult to tell what species the faradaic current is associated with and what species may be reacting chemically with products of that faradaic current. For each experiment, the measured voltage and current first harmonics were extracted, and their phase relationships established. Similarly, if there was a signal in the MS FFT, each mass had its first harmonic amplitude and phase relationship with the current extracted as well. The extraction process involves fitting the real and imaginary components of the signals to a time apodized and Fourier transformed linear superposition of steady periodic harmonics. Fourier coefficients for each harmonic were extracted from the fit and used to reconstruct phase relationships and first harmonic waveforms. A detailed explanation of the fitting procedure is found elsewhere[79]. Quick fitting was executed using the Python frxas.py package found open source on GitHub[78]. Extracted first harmonic amplitudes and phase angles were then used to construct sinusoidal waveforms for visual comparison.

Figure 3.19 shows the phase relationships between M2, M44, and where applicable M28 for different DC and AC potentials at 6 mHz. Table 3.6 presents the phase relationships between the

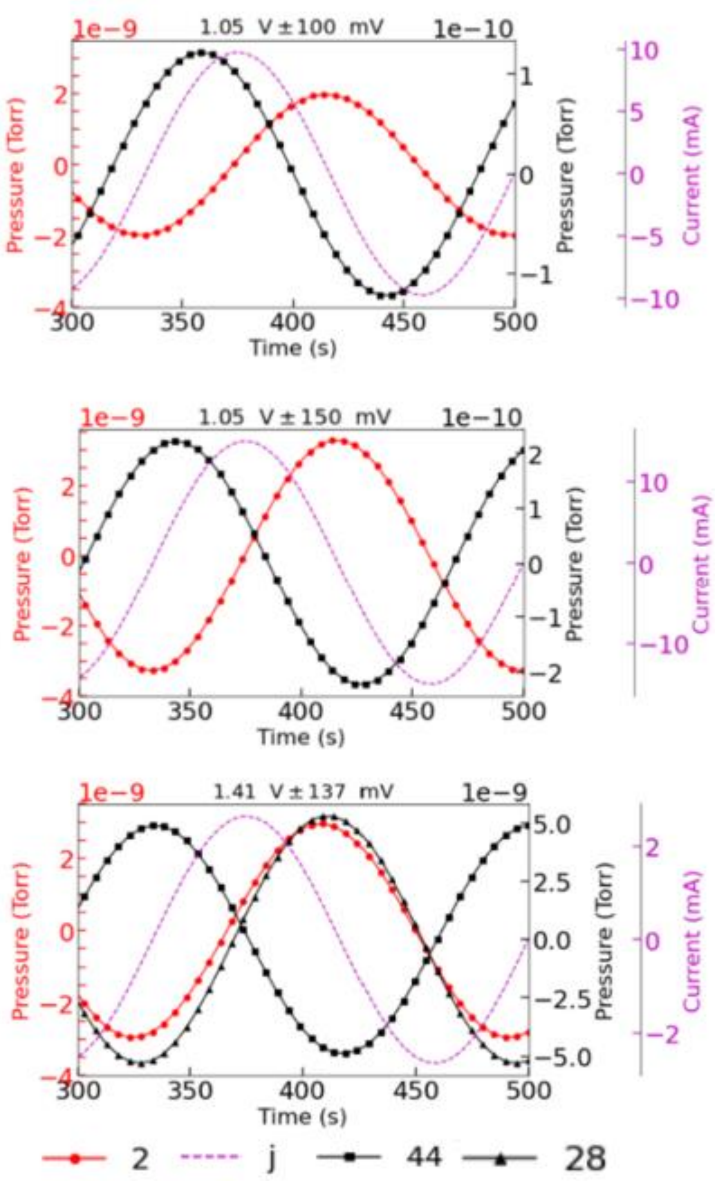

Figure 3.19. Phase relationships between the extracted first harmonics of current (j), M2, M44, and M28 where applicable at 1.05 V ± 100 mV, 1.05 V ± 150 mV, 1.41 V ± 137 mV.

first harmonics for voltage, M2, M32, M44, and M28, where applicable, referenced to the current. As DC voltage and AC voltage increased, the phase angle for CO_2 approached 90 degrees out of phase with the current. The figures show that peak hydrogen production, where dM2/dt is the largest, is associated with peak current (dC/dt) at 1.05 V, *i.e.*, 90 degrees out of phase. At higher voltages, this relationship beings to deviate and perhaps not all H_2 production is associated with the faradaic current. Similarly, for CO_2 at lower voltages the phase angle is far from 90 degrees, but at higher voltages, the peak current lines up at nearly 90 degrees out of phase with peak CO_2 consumption and peak CO production (M28).

This evidence suggests that at higher voltages, more H_2 is being made by the WGS reaction and less by water electrolysis. On the other hand, at lower voltages CO_2 is being mostly consumed by RWGS, but at higher voltages, CO_2 electrolysis is more activated and more directly associated with the fluctuations in current. It is possible that at 1.41 V, the RWGS reaction on the surface is much slower than CO_2 electrolysis, allowing CO to be consumed and some H_2 to be produced by WGS. This shifts their phases away from being 180 degrees out of phase with CO_2 and away from being 90 degrees out of phase with current.

Table 3.6. Phases referenced to current for Figure 3.19

Experiment at 6mHz	M2 Phase Angle	M44 Phase Angle	M32 Phase Angle	M28 Phase Angle	Voltage Phase Angle
1.05 V ± 100 mV	-85.87	35.39	74.28	n/a	-57.63
1.05 V ± 150 mV	-88.85	67.51	55.99	n/a	-54.72
1.41 V ± 137 mV	-71.54	87.49	n/a	-78.08	-36.66

3.7 TECHNICAL DISCUSSION

The mass spectrum deduced mole fractions are difficult to interpret for water and CO; therefore, a quantitative assessment of whether the gases are in RWGS equilibrium could be unreliable. At 800 ºC, the equilibrium constant is 0.96[15] meaning either direction is favorable depending on initial inlet conditions. Despite no intentional introduction of water, it is suspected that some entered with the air leak. Hydrogen was not introduced into the system and has a low natural occurrence in air. Therefore, if the WGS were active, it would likely boost CO_2 production and consume water and CO.

The gas phase kinetics of the RWGS, using the mole fractions from Table 3.4, would indicate a reaction rate of the order of 10^{-14} mol/s in the hemisphere where the electrode sits ($0.54\ cm^3$) of the ceramic reaction chamber, six orders less than the magnitude of the CO_2 molar flow rate of 2.68×10^{-8} mol/s[36,80]. The molar flow rate of CO_2 was calculated using the ideal gas law, a flow rate of 0.5 sccm, CO_2 composition of 7.2 mol %, and standard temperature and pressure (1 atm, 0 ºC). Using Faraday's law for CO_2 electrolysis, the equivalent current to 10^{-14} mol/s is approximately 2 nA, significantly less than measured in this work. Therefore, a significant contribution from gas phase RWGS is unexpected due to the vacuum conditions. A strength of this technique may be the isolation of surface reactions for study.

The I-V and EIS characterization suggests that the GDC10 electrode performance was kinetically limited under conditions tested rather than co-limited by mass transport and kinetics. First, experiments with 0.5 sccm of $CO/CO_2/N_2$ flow all occurred below the voltage associated with limited current density (1.6 V). Secondly, under all conditions the shape of the low frequency arc appeared semicircular with no Warburg or Gerischer-like features (45º high frequency tails). The phase angle at high frequency is greater than 60º. A Gerischer or Warburg high frequency tail would be a key feature of a mass transport limited system, whether gas, surface, or bulk transport.

Wolfgang Bessler has detailed a stagnation point flow geometry model for a fuel cell anode (i.e., an electrolyzer cathode) dominated by coupled convective and diffusive mass transport limitations[72]. Bessler's work has been shown to explain impedance spectra of water electrolysis on Ni-YSZ electrodes by Primdahl and Mogensen[81]. This model describes similar geometry to that used in this work. Bessler's results with the RE in a constant environment are used for comparison. Among other sensitivities discussed, Bessler argues that an increase in overpotential should not influence peak frequency in the limit of significant mass transport limitations. However, 0.9 V, 1.05 V, and 1.4 V all have differences in peak frequency in Figure 3.10 and Figure 3.11. Bessler makes a similar argument for the influence of AC amplitude, though that, too, is not observed for 1.05 V ± 100 mV and ± 150 mV. Finally, at low flow velocity, which corresponds to a low flow rate here, Bessler argued that a semi-circle with a small 45-degree high frequency tail should be observed. While a distorted semicircle was observed here, in no case did any spectra appear to have a 45-degree angled high frequency tail. Even as flow rate, and thus pressure was increased, no Gerischer or Warburg features were present.

The reason this model may not work for this cell configuration is because an assumption of the model is the existence of a stagnation layer above the electrode. A stagnation layer forms because of the assumption of zero-velocity at the surface of the electrode, where diffusion is dominant over convection. Because of the vacuum at total pressure of 0.68 Torr, there likely is no stagnation zero velocity layer at the electrode surface because the Kn number is greater than 0.01. Between 0.01 and 1, the vacuum flow is characterized as neither viscous nor molecular flow, but a transition region between the two where the velocity at the surface is not zero (as assumed by viscous laminar flow) and the reflection of species off surfaces is not diffuse as in molecular flow[38].

For example, the smallest mean free path among the molecules of interest is for water and CO_2. Their mean free paths at 800 ºC and 0.68 Torr are 175 μm. A reasonable characteristic length to choose would be the radius of the hemisphere in which the electrode exists which is 6.35 mm. The Kn number for CO_2 and H_2O is thus 0.027. The other species have higher Kn numbers. Complicating matters further, the alumina pipe that delivers gas presses a gold wire mesh into the gold current collector layer for good electrical contact as shown in Figure 3.20. The characteristic distance between the ceramic feed outlet and the electrode surface is not clear, but may be less than 1 mm. The characteristic length is therefore somewhat uncertain since the gas enters this mesh of twisted wires. The consequence is likely an increase the Kn number as the characteristics dimension would be smaller than the hemisphere radius.

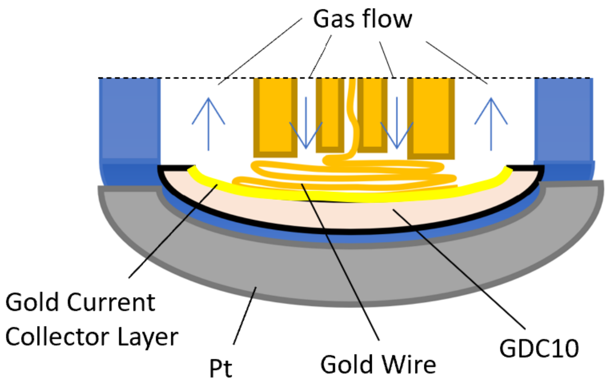

Figure 3.20. Diagram of cathode reaction chamber zoomed in on the reaction volume. A gold wire mesh is shown pressing into a gold current collector layer for good electrical contact.

Lastly, the stagnation point flow model assumes no obstruction between the inlet feed pipe and the electrode surface. In this experimental apparatus, the gold wire mesh is an immediate obstruction to that flow. Perhaps at even higher pressures, a Kn number greater than 0.01 can still be achieved because of the gold mesh layer. Future work must be done to model the flow to account for any pressure gradients created by the mesh.

The I-V curve reached a mass transport limitation around 1.6 V and 4.633 mA. This current is just under the 5.17 mA limit of full consumption of the CO_2 molar flow. It is therefore congruent with the flow rate that the mass transport limitation would be approached as 5.17 mA is approached.

The EIS curves in Figure 3.10 have capacitances of approximately at 65 mF at 0.9 V, 381 mF at 1.05 V ± 100 mV, and 391 mF at 1.05 V ± 150 mV. These capacitances are likely a measure of the capacitance of the bulk ceria for oxygen. This conclusion would be congruent with the thermodynamics. At higher DC potentials and AC potentials, more vacancies are created as shown in Figure 1.4, which shows the nonstoichiometry of GDC10 as a function of p_{O_2}. A voltage of 50 mV corresponds directly to a change in one order of magnitude of p_{O_2}.

Based on a unit cell dimension of 0.54 nm, a difference in a nonstoichiometry from $O_{1.95}$ to $O_{1.77}$ of in GDC10 represents an O_2 capacity change on the order of 2×10^{-7} moles of oxygen. The hemisphere at 0.68 Torr and 1073 K is estimated to have approximately 6×10^{-11} moles of oxygen based on the mole fraction estimated from the MS and the OCV. The GDC10 can absorb about 3000 times more oxygen than there is present in the hemisphere. This is congruent with the observation of oxygen reduction in the I-V curves as potential was swept from OCV to 1.6 V. Given the massive capacitance difference between the bulk ceria and gas phase, it is likely that the capacitance of the low frequency arcs was associated with the capacitance of the ceria bulk. The reason for the change in resistance between 1.05 V and 1.41 V is unclear, however the I-V curve (Figure 3.9) indicates that the window around 1.41 V has steeper slopes indicating less resistance for the mechanism occurring around there, which appears to be significant water and CO_2 reduction. At the lower voltage, it appears that there was a mixture of water reduction and oxygen reduction.

Lastly, the CO production is associated with co-electrolysis rather than RWGS. The I-V curve of Figure 3.9 shows a significant presence and production of hydrogen before 1.3 V. At 1.3 V, CO_2 consumption became measurable. If RWGS were significant under the conditions studied, then as hydrogen presence became significant, there should have been significant CO_2 consumption before 1.3 V to maintain equilibrium, yet there was none. This conclusion is further supported by Figure 3.19. At 1.41 V ± 137 mV the CO production and H_2 production were phase aligned; their peak productions were aligned with peak current. CO_2 peak consumption aligned with peak current as well. If co-electrolysis were dominant, this would be the expected phase relationship between current, H_2, CO, and CO_2. Additionally, as lower DC and AC voltages were used, hydrogen maintained the same relationship with current, yet CO_2 transitioned closer to having peak CO_2 consumption at peak hydrogen presence. This is congruent with the observation of little to no CO_2 consumption under 1.3 V in the I-V curve of Figure 3.9. It also means that the little amount of CO_2 that was consumed was likely from a slow RWGS reaction below 1.3 V.

3.8 CONCLUSION

A new technique for investigating time correlated behavior of gas phase species with electrochemical perturbations was presented, named Frequency Resolved Mass Spectrometry. FRMS has a few unique strengths: detecting small signals, the ability to isolate the behavior of certain gas species at time scales of interest, and the ability to extract phase correlated first harmonic signals. The extraction and correlation of gas phase species provides a deeper level of information, providing insight into gas species association with the faradaic current. More technique development is required to fully characterize the breadth of information this technique can offer.

Better control of gas phase species such as oxygen and water content should be prioritized in future research. With stricter control over composition, analysis can be done around equilibrium potentials instead of requiring high overpotentials to eliminate oxygen content. Furthermore, strict quantitative analysis of gas phase species would be especially helpful and allow determination of whether the gas phase is in RWGS equilibrium.

The high oxygen capacitance of the GDC10 contributed to very low peak frequencies that were inaccessible by the frequency generator. The low frequency arc is the arc most associated with the kinetics of the reaction. The tuning of that arc to be within the max frequency that can be measured by the MS (80 mHz) and the lowest frequency that can be applied by lab hardware (6 mHz) should be prioritized. This perhaps can be done with dense thin films of GDC10, which would also eliminate uncertainty surrounding electrode geometry such as porosity, thickness, and tortuosity.

It is concluded that under the scope of the conditions studied here, RWGS contributed negligibly to the production and consumption of CO and CO_2, respectively. Co-electrolysis dominated above 1.3 V. Below 1.3 V, water electrolysis and a slow RWGS caused fluctuations in the gas phase perturbations. This conclusion is supported by the lack of appropriate CO_2 consumption in the presence of significant H_2 production below 1.3 V, and the phase alignment of peak current with CO and H_2 production and CO_2 consumption above a DC bias of 1.3 V. Below 1.3 V, CO_2 fluctuation amplitude was significantly smaller than above 1.3 V, and CO_2 peak consumption transitioned closer to phase alignment with peak H_2 presence.

Modeling of the gas flow within the vacuum would also provide a better understanding of how to model mass transport in the gas phase and deconvolute any contributions from this. More conditions should be explored in future research including different compositions, temperatures, pressures, electrodes, electrode geometries, and different types of reactions to be studied. FRMS has great potential to provide insight into many reaction mechanisms and may prove a highly useful tool for the electrocatalytic community.

3.9 APPENDIX A

Figure 3.8 is analyzed here in three different ways to find CO content. Table 3.7 shows the standard fragmentation pattern fractions for each species from the SRS RGA software.

Table 3.7. Fragmentation pattern fractions (α) for Ar, CO, CO_2, H_2, H_2O, N_2

Species	Fragmentation Pattern	
	m/e	α (%)
Argon	18	0.0904977
	38	0.0904977
	36	0.271493
	20	9.04977
	40	90.4977
Carbon Dioxide	46	0.392157
	45	0.784314
	12	4.70588
	16	7.05882
	28	8.62745

	44	78.4314
Carbon Monoxide	30	0.18315
	14	0.915751
	29	0.915751
	16	1.8315
	12	4.57875
	28	91.5751
Hydrogen	1	4.76191
	2	95.2381
Nitrogen	29	0.740741
	14	6.66667
	28	92.5926
Oxygen	33	0.0893655
	34	0.357462
	16	10.1877
	32	89.3655
Water	19	0.0744048
	20	0.223214
	16	8.18452
	17	17.1131
	18	74.4048

3.9.1 *Method M12*

Each of the partial pressure is found using the measured pressure at a given m/e (M_i) and the fragmentation pattern fractions.

$$p_{\mathrm{CO_2}} = \frac{M_{44}}{\alpha^{44}{}_{\mathrm{CO_2}}} \tag{3A.1}$$

$$p_{\mathrm{O_2}} = \frac{M_{32}}{\alpha^{32}{}_{\mathrm{O_2}}} \tag{3A.2}$$

$$p_{\mathrm{N_2}} = \frac{M_{14}}{\alpha^{14}{}_{\mathrm{N_2}}} \tag{3A.3}$$

$$p_{\mathrm{H_2O}} = \frac{M_{18}}{\alpha^{18}{}_{\mathrm{H_2O}}} \tag{3A.4}$$

$$p_{\mathrm{H_2}} = \frac{M_{2}}{\alpha^{2}{}_{\mathrm{H_2}}} \tag{3A.5}$$

$$p_{\mathrm{Ar}} = \frac{M_{40}}{\alpha^{40}{}_{\mathrm{Ar}}} \tag{3A.6}$$

$$p_{\mathrm{CO}} = \frac{\left(M_{12} - p_{\mathrm{CO_2}}\alpha^{12}{}_{\mathrm{CO_2}}\right)}{\alpha^{12}{}_{\mathrm{CO}}} \tag{3A.7}$$

Then the mole fractions are found by taking the partial pressures and dividing by the total pressures.

$$y_i = \frac{p_i}{\Sigma p_i} \tag{3A.8}$$

3.9.2 *Method M28 and M14*

In this method, most partial pressures are calculated similar to the M12 method, but a system of two equations is used to solve for p_{CO} and $p_{\mathrm{N_2}}$ using M_{14} and M_{28}.

$$p_{\mathrm{CO_2}} = \frac{M_{44}}{\alpha^{44}{}_{\mathrm{CO_2}}} \tag{3A.9}$$

$$p_{\mathrm{O_2}} = \frac{M_{32}}{\alpha^{32}{}_{\mathrm{O_2}}} \tag{3A.10}$$

$$p_{\mathrm{H_2O}} = \frac{M_{18}}{\alpha^{18}{}_{\mathrm{H_2O}}} \tag{3A.11}$$

$$p_{\mathrm{H_2}} = \frac{M_2}{\alpha^{2}{}_{\mathrm{H_2}}} \tag{3A.12}$$

$$p_{\mathrm{Ar}} = \frac{M_{40}}{\alpha^{40}{}_{\mathrm{Ar}}} \tag{3A.13}$$

$$M_{14} \ = \ p_{\mathrm{N_2}}\alpha^{14}{}_{\mathrm{N_2}} \ + \ p_{\mathrm{CO}}\alpha^{14}{}_{\mathrm{CO}} \tag{3A.14}$$

$$M_{28} = p_{\mathrm{CO_2}}\,\alpha^{28}{}_{\mathrm{CO_2}} \ + \ p_{\mathrm{CO}}\,\alpha^{28}{}_{\mathrm{CO}} \ + \ p_{\mathrm{N_2}}\,\alpha^{28}{}_{\mathrm{N_2}} \tag{3A.15}$$

Then the mole fractions are found by taking the partial pressures and dividing by the total pressures.

$$y_i = \frac{p_i}{\Sigma p_i} \tag{3A.16}$$

3.9.3 *Method M28 and M14*

In this method, most partial pressures are calculated like the M12 method, but a system of two equations is sued to solve for p_{CO} and $p_{\mathrm{CO_2}}$ using M_{16} and M_{12}.

$$p_{\mathrm{O_2}} \ = \frac{M_{32}}{\alpha^{32}{}_{\mathrm{O_2}}} \tag{3A.17}$$

$$p_{\mathrm{H_2O}} = \frac{M_{18}}{\alpha^{18}{}_{\mathrm{H_2O}}} \tag{3A.18}$$

$$p_{\mathrm{H_2}} \ = \frac{M_2}{\alpha^{2}{}_{\mathrm{H_2}}} \tag{3A.19}$$

$$p_{\mathrm{Ar}} = \frac{M_{40}}{\alpha^{40}{}_{\mathrm{Ar}}} \tag{3A.20}$$

$$M_{12} \ = \ p_{\mathrm{CO_2}}\alpha^{12}{}_{\mathrm{CO_2}} \ + \ p_{\mathrm{CO}}\alpha^{16}{}_{\mathrm{CO}} \tag{3A.21}$$

$$M_{16} = p_{\mathrm{CO_2}}\,\alpha^{16}{}_{\mathrm{CO_2}} \ + \ p_{\mathrm{CO}}\,\alpha^{16}{}_{\mathrm{CO}} \ + \ p_{\mathrm{O_2}}\,\alpha^{16}{}_{\mathrm{O_2}} + p_{\mathrm{H_2}O}\,\alpha^{16}{}_{\mathrm{H_2}O} \tag{3A.22}$$

$$p_{\mathrm{N_2}} \ = \frac{\left(M_{28} - p_{\mathrm{CO}}\,\alpha^{28}{}_{\mathrm{CO}} - p_{\mathrm{CO_2}}\alpha^{28}{}_{\mathrm{CO_2}}\right)}{\alpha^{28}{}_{\mathrm{N_2}}} \tag{3A.23}$$

Then the mole fractions are found by taking the partial pressures and dividing by the total pressures.

$$y_i = \frac{p_i}{\Sigma p_i} \tag{3A.24}$$

3.10 APPENDIX B: SUMMARY OF FFT AND EXTRACTION OF FIRST HARMONICS

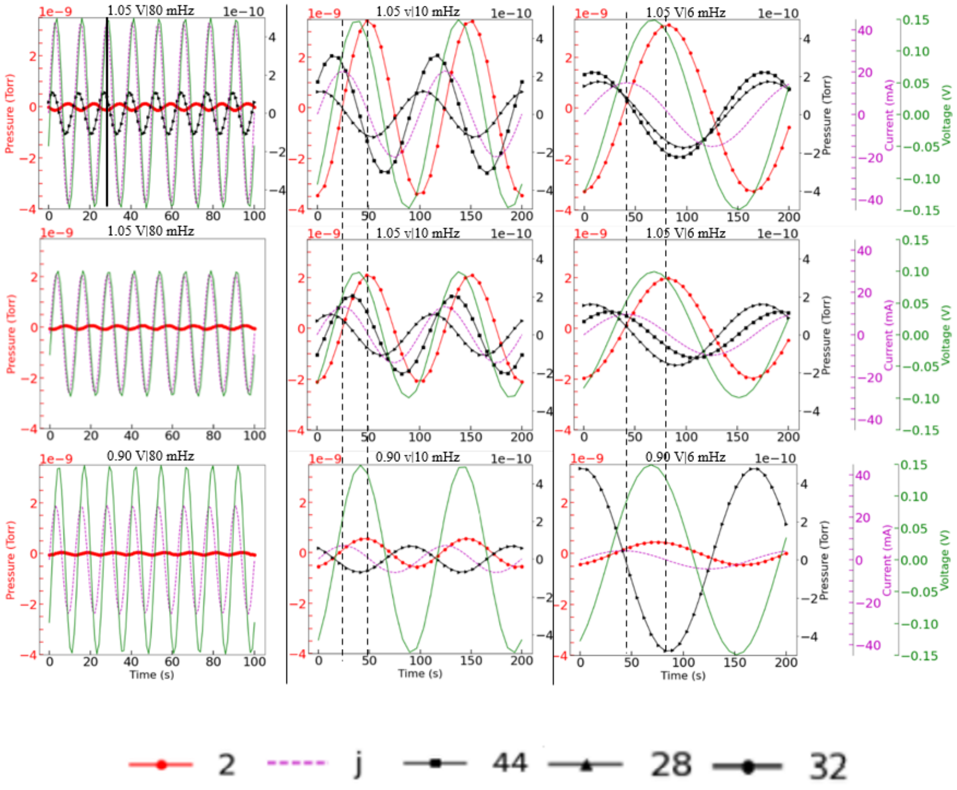

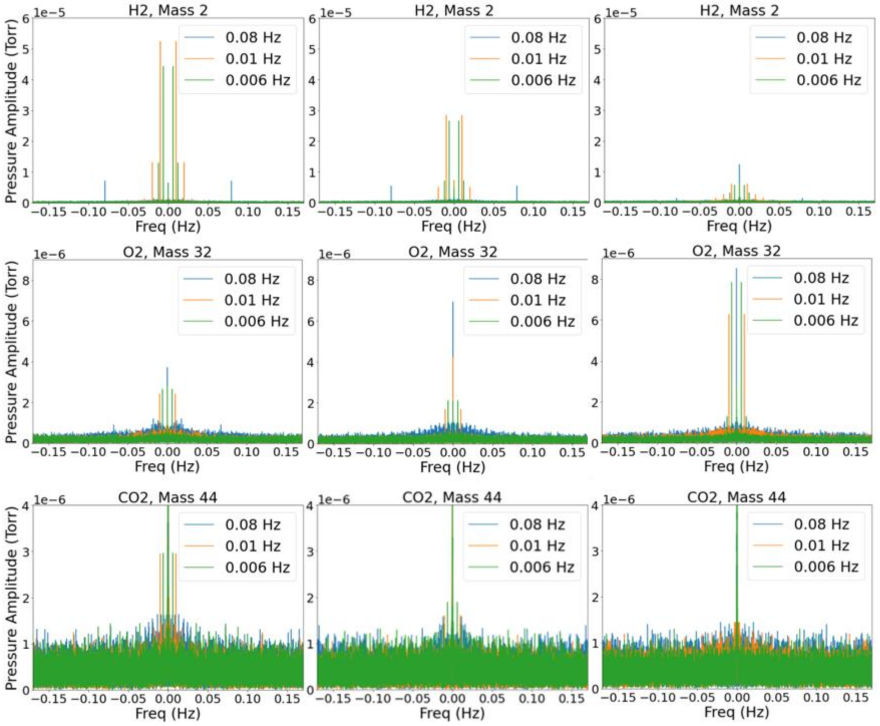

Chapter 4. SUMMARY

4.1 SUMMARY OF RESULTS

This research work details a new method to deconvolute the contributions of RWGS and co-electrolysis to CO_2 consumption and CO production. Within the literature, there is no consensus on the governing rate laws for this combination of reactions. It is complicated by coupling of mass transport on the surface, gas phase, and bulk with thermodynamics and kinetics. It is further convoluted by differences in experimental set up, cell microstructure, and electrode material. Among the materials studied within the literature are MIECs, of which GDC10 is one. GDC10 was chosen as an electrocatalyst here because of its activity, resistance to carbon deposition, resistance to degradation by oxidation, and its extensive characterization within the literature due to its use as an electrolyte[12,21–25,27].

Here, the effects of inadequate current collection were highlighted as a potentially convoluting phenomenon for interpretation of electrochemical characterization of cells. Experiments with a porous current collecting layer and without a porous current collecting layer of gold were completed and showed significant differences in impedance spectra. The low frequency arc resistances were orders of magnitude different, despite being studied under the same conditions. COMSOL modeling revealed how a combination of sheet resistance, electrolyte resistance, pitch of current collector mesh, and electrolyte thickness influence the spread of electrical current throughout the cell. At high sheet resistance, a smaller amount of cell area is used, while at low sheet resistance, the entire expected cell area is used. The amount of cell area used is also frequency dependent. The effect of inadequate current collection can make a reaction appear mass transport limited in shape when it is actually kinetically limited.

A 2D physics-based model was developed that fits well the asymptotic limits of the 3D COMSOL simulation. The 2D model fails to capture an intermediate region, a region in which spread of current in the *x* and *y* dimensions matched the thickness of the electrode. Given the experimental cell parameters, the 2D model determined it was unlikely that sheet resistance should have been influencing the experimental results. The same was indicated from a literature review. The conclusion was that the gold meshes being used in the experiments were not properly contacting the surface of the electrode. This could be the result of a mechanism that prevents good electrical contact between the electrode surface and the mesh. It was recommended that, to mitigate the risk of inadequate current collection, a layer of porous current collector be used on top of the electrode if the electrode is not conductive enough by itself.

The mitigation of uncertainty in current collection allowed more certainty in interpreting the results of all GDC10 cells within the lab. This included the novel technique development of Frequency Resolved Mass Spectrometry (FRMS). A vacuum reaction chamber was developed to enable online mass spectrometry that can be phase-aligned in the time domain with current and voltage perturbations in the electrode. The technique enables a deeper level of understanding of reaction mechanisms.

While still in development, the FRMS technique has been demonstrated to have several strengths. It can correlate steady state change in current and voltage with gas phase data. It uses FFT to deconvolute signals that are unrecognizable with noise. It can detect higher harmonics in gas phase waveforms. Finally, it can reveal which gas phase species are active at different time scales by controlling perturbation frequency. This is information that cannot be retrieved from EIS or I-V curves alone.

It was concluded that co-electrolysis dominated the production of CO and consumption of CO_2 under the conditions studied. The RWGS was deemed negligible based on an I-V curve that showed no significant consumption of CO_2 below 1.3 V despite significant production of H_2, and an FRMS analysis that showed the peak consumption of CO_2 and peak production of H_2 and CO aligned with peak current above 1.3 V DC bias. FRMS phase analysis indicated that below 1.3 V, a faint CO_2 first harmonic signal was likely the result of a slow RWGS compared to water electrolysis. This was indicated by peak hydrogen presence nearly aligning with peak CO_2 consumption.

It was also concluded that water electrolysis is more active than CO_2 reduction because in nearly all frequencies and amplitudes attempted, hydrogen fluctuations were measurable. These fluctuations are typically 90 degrees out of phase with the current. Peak current is attributed to peak hydrogen production. The only time this was not true was at higher voltages (1.41 V) where more CO_2 reduction was active. Estimation of gas phase RWGS rates indicated that gas phase RWGS was unlikely to be competitive in the vacuum chamber at 0.68 Torr.

Based on impedance spectra, the GDC10/YSZ10/Pt cell is likely kinetically limited. This is indicated by the semicircular shape of all low frequency impedance arcs, none of which exhibits high frequency Warburg tails or Gerischer shapes. A stagnation layer mass transport model that couples gas phase diffusion with convection was consulted. It was found that mass transport was unlikely to be an issue because the vacuum created a situation in which the no-slip condition no longer held. The chamber's gas species likely have Kn numbers between 0.01 to 1, in which the flow is no longer considered no-slip at surface.

4.2 FUTURE WORK

Technique development of FRMS needs to continue to better understand its potential. Control of inlet feed composition should be a priority for future research. Because of the oxygen leak, it was impossible to study the reaction mechanism around equilibrium. The source of the oxygen leak has not been determined, despite significant efforts to do so. A more effective process for baking out the vacuum system could have alleviated this problem. Plastic tubing used for gas flow from pressure tanks should be replaced with stainless steel tubing to lower the likelihood of oxygen or water leaking into the gas lines.

Unfortunately, the frequencies of the low frequency arcs were so low that much of them were impossible to study due to equipment limitations. This was likely caused by the high capacitance of the porous GDC10 electrode. It is recommended that thin films of GDC10 be used to eliminate uncertainties in microstructure and to reduce the capacitance so that lower frequencies can be studied.

Quantitative gas analysis should also be pursued by calibrating the MS with pure gases after the MS air leak is resolved. Custom sensitivity factors and fragmentation patters need to be developed and periodically checked as the MS ages. Also, a water collection system should be added to the vacuum system to include water in a mass balance of species. Perhaps a humidity sensor downstream of the reactor could be used for water instead. For a better measure of CO, it is suggested to replace N_2 with Ar as a diluent so that M28 is dominated by CO instead of N_2. Quantitative gas analysis could have determined if the species were in RWGS equilibrium.

Different flow compositions, voltage, AC perturbations, flow rates, total pressures, and temperatures should be investigated to further characterize the cell. Additionally, other electrode materials, such as perovskites, can be painted on the inside or outside of the YSZ tube and studied with the apparatus setup.

Modeling should be done of the coupling of the gas phase and current fluctuations. A micro-kinetic model that assumes a rate law can be coupled with a sinusoidal perturbation of current. This model can explore expected gas phase fluctuations as a function of rate limiting steps or competitiveness between reactions. Modeling of gas flow within the vacuum system may allow further understanding of mass transport limitations.

Finally, it is suggested to pursue an oxygen isotope exchange study. Water can be made by feeding hydrogen and $^{18}O_2$ into a pre-reactor, before being fed into the vacuum reaction chamber. The water will be mixed with CO_2 and CO within the vacuum reaction chamber. If ^{18}O exchanges with CO_2 and CO, then that could be measured by MS. The degree to which ^{18}O is exchanged would be a measure and indicator of the degree to which surface and/or gas phase exchange is occurring for RWGS.

BIBLIOGRAPHY

1. AR5 Synthesis Report: Climate Change 2014 — IPCC. https://www.ipcc.ch/report/ar5/syr/.
2. U.S. energy facts explained - consumption and production - U.S. Energy Information Administration (EIA). https://www.eia.gov/energyexplained/us-energy-facts/.
3. Greenhouse Gas Inventory Data Explorer | US EPA. https://cfpub.epa.gov/ghgdata/inventoryexplorer/.
4. Forster, M. (ECY). Washington State Greenhouse Gas Emissions Inventory: 1990-2018. 25.
5. Alternative Fuels Data Center: Hydrogen Laws and Incentives in California. https://afdc.energy.gov/fuels/laws/HY?state=ca.
6. Fact of the Month #18-01, January 29: There Are 39 Publicly Available Hydrogen Fueling Stations in the United States. *Energy.gov* https://www.energy.gov/eere/fuelcells/fact-month-18-01-january-29-there-are-39-publicly-available-hydrogen-fueling-stations.
7. Alternative Fuels Data Center: Electric Vehicle Charging Station Locations. https://afdc.energy.gov/fuels/electricity_locations.html#/find/nearest?fuel=ELEC.
8. Colbertaldo, P., Agustin, S. B., Campanari, S. & Brouwer, J. Impact of hydrogen energy storage on California electric power system: Towards 100% renewable electricity. *International Journal of Hydrogen Energy* **44**, 9558–9576 (2019).
9. Power-to-Gas: The Case for Hydrogen White Paper. (2015).
10. Microsoft makes a ‘crazy’ bet on fuel cells to feed power-hungry data centers. *The Seattle Times* https://www.seattletimes.com/business/microsoft/microsoft-makes-a-crazy-bet-on-fuel-cells-to-feed-power-hungry-data-centers/ (2017).
11. Pellow, M. A., Emmott, C. J. M., Barnhart, C. J. & Benson, S. M. Hydrogen or batteries for grid storage? A net energy analysis. *Energy Environ. Sci.* **8**, 1938–1952 (2015).

12. Hauch, A. *et al.* Recent advances in solid oxide cell technology for electrolysis. *Science* **370**, (2020).

13. Graves, C., Ebbesen, S. D., Mogensen, M. & Lackner, K. S. Sustainable hydrocarbon fuels by recycling CO2 and H2O with renewable or nuclear energy. *Renewable and Sustainable Energy Reviews* **15**, 1–23 (2011).

14. Goodenough, J. B. Ceramic solid electrolytes. *Solid State Ionics* **94**, 17–25 (1997).

15. Jiang, Y. & Virkar, A. V. Fuel Composition and Diluent Effect on Gas Transport and Performance of Anode-Supported SOFCs. *J. Electrochem. Soc.* **150**, A942 (2003).

16. Isenberg, A. O. & Verostko, C. E. Carbon Dioxide and Water Vapor High Temperature Electrolysis. *SAE Transactions* **98**, 820–835 (1989).

17. Gómez, S. Y. & Hotza, D. Current developments in reversible solid oxide fuel cells. *Renewable and Sustainable Energy Reviews* **61**, 155–174 (2016).

18. Jensen, S. H., Høgh, J. V. T., Barfod, R. & Mogensen, M. B. High temperature electrolysis of steam and carbon dioxide. in *Energy technologies for Post Kyoto targets in the medium term. Proceedings* 204–215 (2003).

19. Schäfer, D., Fang, Q., Blum, L. & Stolten, D. Syngas production performance and degradation analysis of a solid oxide electrolyzer stack. *Journal of Power Sources* **433**, 126666 (2019).

20. Atkinson, A. *et al.* Advanced anodes for high-temperature fuel cells. in *Materials for Sustainable Energy* 213–223 (Co-Published with Macmillan Publishers Ltd, UK, 2010). doi:10.1142/9789814317665_0030.

21. Montini, T., Melchionna, M., Monai, M. & Fornasiero, P. Fundamentals and Catalytic Applications of CeO2-Based Materials. *Chem. Rev.* **116**, 5987–6041 (2016).

22. Wang, J. Electronic structure of gadolinium-doped ceria system: A DFT study. *Mod. Phys. Lett. B* **33**, 1950095 (2019).

23. Yahiro, H., Baba, Y., Eguchi, K. & Arai, H. High Temperature Fuel Cell with Ceria-Yttria Solid Electrolyte. *J. Electrochem. Soc.* **135**, 2077 (1988).

24. Hideaki Inaba & Hiroaki Tagawa. Ceria-based solid electrolytes. *Solid State Ionics* **83**, 1–16 (1996).

25. Hiromichi Arai, Toshiya Kunisaki, Yasuhiro Shimzu, & Tetsuro Seiyama. Electrical properties of calcia-doped ceria with oxygen ion conduction. *Solid State Ionics* **20**, 241–248 (1986).

26. Hidenori Yahiro, Koichi Eguchi, & Hiromichi Arai. Electrical properties and reducibilities of ceria-rare earth oxide systems and their application to solid oxide fuel cell. *Solid State Ionics* **36**, 71–75 (1989).

27. Liying HE, Yumin SU, Jiang Lanhong, & Shikao SHI. Recent advances of cerium oxide nanoparticles in synthesis, luminescence and biomedical studies: a review. *Journal of Rare Earths* **33**, 791–799 (2015).

28. Navarro, L., Marques, F. & Frade, J. n-Type Conductivity in Gadolinia-Doped Ceria. *J. Electrochem. Soc.* **144**, 267–273 (1997).

29. Yashiro, K. *et al.* Mass transport properties of Ce0.9Gd0.1O2−δ at the surface and in the bulk. *Solid State Ionics* **152**, 469–476 (2002).

30. Wang, S., Inaba, H., Tagawa, H., Dokiya, M. & Hashimoto, T. Nonstoichiometry of Ce0.9Gd0.1O1.95−x. *Solid State Ionics* **107**, 73–79 (1998).

31. Stoots, C. M., O'Brien, J. E., Herring, J. S. & Hartvigsen, J. J. Syngas Production via High-Temperature Coelectrolysis of Steam and Carbon Dioxide. *Journal of Fuel Cell Science and Technology* **6**, (2008).

32. Ebbesen, S., Graves, C. & Mogensen, M. Production of Synthetic Fuels by Co-Electrolysis of Steam and Carbon Dioxide. *International Journal of Green Energy* **6**, 646–660 (2009).

33. Zhan, Z. *et al.* Syngas Production By Coelectrolysis of CO2/H2O: The Basis for a Renewable Energy Cycle. *Energy Fuels* **23**, 3089–3096 (2009).

34. Graves, C., Ebbesen, S. D. & Mogensen, M. Co-electrolysis of CO2 and H2O in solid oxide cells: Performance and durability. *Solid State Ionics* **192**, 398–403 (2011).

35. Ebbesen, S. D., Knibbe, R. & Mogensen, M. Co-Electrolysis of Steam and Carbon Dioxide in Solid Oxide Cells. *J. Electrochem. Soc.* **159**, F482 (2012).

36. Ni, M. An electrochemical model for syngas production by co-electrolysis of H2O and CO2. *Journal of Power Sources* **202**, 209–216 (2012).

37. Operating Manual and Programming Reference: Models RGA100, RGA200, and RGA300 Residual Gas Analyzer.

38. O'Hanlon, J. F. *A User's Guide to Vacuum Technology*. (John Wiley & Sons, 2005).

39. Zheng, Y. *et al.* A review of high temperature co-electrolysis of H2O and CO2 to produce sustainable fuels using solid oxide electrolysis cells (SOECs): advanced materials and technology. *Chem. Soc. Rev.* **46**, 1427–1463 (2017).

40. Küngas, R. Review—Electrochemical CO $_2$ Reduction for CO Production: Comparison of Low- and High-Temperature Electrolysis Technologies. *Journal of The Electrochemical Society* **167**, 044508 (2020).

41. Daza, Y. A. & Kuhn, J. N. CO2 conversion by reverse water gas shift catalysis: comparison of catalysts, mechanisms and their consequences for CO2 conversion to liquid fuels. *RSC Adv.* **6**, 49675–49691 (2016).

42. Jones, J.-P., Prakash, G. K. S. & Olah, G. A. Electrochemical CO2 Reduction: Recent Advances and Current Trends. *Isr. J. Chem.* **54**, 1451–1466 (2014).

43. Foit, S. R., Vinke, I. C., de Haart, L. G. J. & Eichel, R.-A. Power-to-Syngas: An Enabling Technology for the Transition of the Energy System? *Angew. Chem. Int. Ed.* **56**, 5402–5411 (2017).

44. Yue, X. & Irvine, J. T. S. Alternative Cathode Material for CO2 Reduction by High Temperature Solid Oxide Electrolysis Cells. *J. Electrochem. Soc.* **159**, F442–F448 (2012).

45. Torrell, M., García-Rodríguez, S., Morata, A., Penelas, G. & Tarancón, A. Co-electrolysis of steam and CO2 in full-ceramic symmetrical SOECs: a strategy for avoiding the use of hydrogen as a safe gas. *Faraday Discuss.* **182**, 241–255 (2015).

46. Adler, S. B. Factors Governing Oxygen Reduction in Solid Oxide Fuel Cell Cathodes. *Chem. Rev.* **104**, 4791–4844 (2004).

47. TROVARELLI, A. Catalytic Properties of Ceria and CeO2-Containing Materials. *Catalysis Reviews* **38**, 439–520 (1996).

48. Green, R. D., Liu, C.-C. & Adler, S. B. Carbon dioxide reduction on gadolinia-doped ceria cathodes. *Solid State Ionics* **179**, 647–660 (2008).

49. Kharton, V. V. *et al.* Ceria-based materials for solid oxide fuel cells. *Journal of Materials Science* **36**, 1105–1117 (2001).

50. Bishop, S. R., Duncan, K. L. & Wachsman, E. D. Surface and bulk oxygen non-stoichiometry and bulk chemical expansion in gadolinium-doped cerium oxide. *Acta Materialia* **57**, 3596–3605 (2009).

51. Wang, S., Kobayashi, T., Dokiya, M. & Hashimoto, T. Electrical and Ionic Conductivity of Gd-Doped Ceria. *J. Electrochem. Soc.* **147**, 3606–3609 (2000).

52. Boukamp, B. A., Hildenbrand, N., Nammensma, P. & Blank, D. H. A. The impedance of thin dense oxide cathodes. *Solid State Ionics* **192**, 404–408 (2011).

53. Boukamp, B. A., Hildenbrand, N., Bouwmeester, H. J. M. & Blank, D. H. A. Impedance of thin film cathodes: Thickness and current collector dependence. *Solid State Ionics* **283**, 81–90 (2015).

54. González-Cuenca, M., Zipprich, W., Boukamp, B. A., Pudmich, G. & Tietz, F. Impedance Studies on Chromite-Titanate Porous Electrodes under Reducing Conditions. *Fuel Cells* **1**, 256–264 (2001).

55. Adler, S. B. Reference Electrode Placement in Thin Solid Electrolytes. *J. Electrochem. Soc.* **149**, E166 (2002).

56. Uhm, S. & Kim, Y. D. Electrochemical conversion of carbon dioxide in a solid oxide electrolysis cell. *Curr. Appl. Phys.* **14**, 672–679 (2014).

57. Laguna-Bercero, M. A. Recent advances in high temperature electrolysis using solid oxide fuel cells: A review. *Journal of Power Sources* **203**, 4–16 (2012).

58. Zhang, W., Zheng, Y., Yu, B., Wang, J. & Chen, J. Electrochemical characterization and mechanism analysis of high temperature Co-electrolysis of CO2 and H2O in a solid oxide electrolysis cell. *International Journal of Hydrogen Energy* **42**, 29911–29920 (2017).

59. Chen, X., Guan, C., Xiao, G., Du, X. & Wang, J.-Q. Syngas production by high temperature steam/CO2 coelectrolysis using solid oxide electrolysis cells. *Faraday Discuss.* **182**, 341–351 (2015).

60. Mahmood, A., Bano, S., Yu, J. H. & Lee, K.-H. Effect of operating conditions on the performance of solid electrolyte membrane reactor for steam and CO2 electrolysis. *Journal of Membrane Science* **473**, 8–15 (2015).

61. Kim, S.-W. *et al.* Reactions and mass transport in high temperature co-electrolysis of steam/CO2 mixtures for syngas production. *J. Power Sources* **280**, 630–639 (2015).

62. Alenazey, F. *et al.* Production of synthesis gas (H2 and CO) by high-temperature Co-electrolysis of H2O and CO2. *International Journal of Hydrogen Energy* **40**, 10274–10280 (2015).

63. Kleiminger, L., Li, T., Li, K. & Kelsall, G. H. Syngas (CO-H2) production using high temperature micro-tubular solid oxide electrolysers. *Electrochimica Acta* **179**, 565–577 (2015).

64. Yu, S.-B. *et al.* Syngas production in high performing tubular solid oxide cells by using high-temperature H2O/CO2 co-electrolysis. *Chemical Engineering Journal* **335**, 41–51 (2018).

65. Li, Q. *et al.* Understanding the occurrence of the individual CO2 electrolysis during H2O-CO2 co-electrolysis in classic planar Ni-YSZ/YSZ/LSM-YSZ solid oxide cells. *Electrochimica Acta* **318**, 440–448 (2019).

66. Aicart, J., Laurencin, J., Petitjean, M. & Dessemond, L. Experimental Validation of Two-Dimensional H2O and CO2 Co-Electrolysis Modeling. *Fuel Cells* **14**, 430–447 (2014).

67. Yue, X. & Irvine, J. T. S. (La,Sr)(Cr,Mn)O3/GDC cathode for high temperature steam electrolysis and steam-carbon dioxide co-electrolysis. *Solid State Ionics* **225**, 131–135 (2012).

68. Li, W., Wang, H., Shi, Y. & Cai, N. Performance and methane production characteristics of H2O–CO2 co-electrolysis in solid oxide electrolysis cells. *International Journal of Hydrogen Energy* **38**, 11104–11109 (2013).

69. Aicart, J., Petitjean, M., Laurencin, J., Tallobre, L. & Dessemond, L. Accurate predictions of H2O and CO2 co-electrolysis outlet compositions in operation. *Int. J. Hydrog. Energy* **40**, 3134–3148 (2015).

70. Lo Faro, M., Trocino, S., Zignani, S. C., Antonucci, V. & Aricò, A. S. Production of syngas by solid oxide electrolysis: A case study. *International Journal of Hydrogen Energy* **42**, 27859–27865 (2017).

71. Ebbesen, S. D., Sun, X. & Mogensen, M. B. Understanding the processes governing performance and durability of solid oxide electrolysis cells. *Faraday Discuss.* **182**, 393–422 (2015).

72. Bessler, W. G. Gas Concentration Impedance of Solid Oxide Fuel Cell Anodes: I. Stagnation Point Flow Geometry. *J. Electrochem. Soc.* **153**, A1492 (2006).

73. Chueh, W. C. *et al.* Highly Enhanced Concentration and Stability of Reactive Ce3+ on Doped CeO2 Surface Revealed In Operando. *Chem. Mater.* **24**, 1876–1882 (2012).

74. Feng, Z. A., Machala, M. L. & Chueh, W. C. Surface electrochemistry of CO2 reduction and CO oxidation on Sm-doped CeO2−x: coupling between Ce3+ and carbonate adsorbates. *Phys. Chem. Chem. Phys.* **17**, 12273–12281 (2015).

75. Hauser, D., Nenning, A., Opitz, A. K., Klötzer, B. & Penner, S. Spectro-electrochemical setup for in situ and operando mechanistic studies on metal oxide electrode surfaces. *Review of Scientific Instruments* **91**, 084104 (2020).

76. B.S. Gerwe *et al.* Revealing timescale-dependent oxygen vacancy distributions in solid oxide fuel cell electrodes using frequnecy-resolved X-ray absorption." In preparation.

77. Duboviks, V. *et al.* A Raman spectroscopic study of the carbon deposition mechanism on Ni/CGO electrodes during CO/CO2 electrolysis. *Phys. Chem. Chem. Phys.* **16**, 13063–13068 (2014).

78. B.S. Gerwe. *frxas.py*.

79. Wilson, J. R., Schwartz, D. T. & Adler, S. B. Nonlinear electrochemical impedance spectroscopy for solid oxide fuel cell cathode materials. *Electrochimica Acta* **51**, 1389–1402 (2006).

80. Lehnert, W., Meusinger, J. & Thom, F. Modelling of gas transport phenomena in SOFC anodes. *Journal of Power Sources* **87**, 57–63 (2000).

81. Primdahl, S. & Mogensen, M. Gas Conversion Impedance: A Test Geometry Effect in Characterization of Solid Oxide Fuel Cell Anodes. *J. Electrochem. Soc.* **145**, 2431 (1998).

VITA

Jonathan Witt is originally from Maryland and attended Lehigh University, PA for his bachelor's degree in chemical engineering and graduated in 2015. While at Lehigh, Jon studied novel materials for solid oxide fuel cells under the guidance of Prof. Steven McIntosh. In Sept. 2015, Jon started as a graduate student at the University of Washington (UW) studying solid oxide electrolyzers in the Adler and Stuve lab, as a co-advised doctoral student. While at UW, Jon was proud to be the head of outreach for the Association of Chemical Engineering graduate Students (ACES) and a lead organizer and elected member of the UAW 4121 Joint Council. Jon has been heavily involved in his local community and is highly interested in the intersection of science, equity, politics, and science communication. He took every advantage of offerings by the UW Clean Energy Institute (CEI) to practice science policy, outreach, science communication, and consulting for start-up investors. He found the Torrance Fellowship with E8 Angel investors to be one of the most rewarding programs offered by UW CEI.

Jon enjoys spending his time in Seattle volunteering for great candidates and policies proposed by local government and organizations, riding public transit, camping, hiking, biking, gardening, and giving his notorious 12-to-16-hour tours of Seattle to his friends and family that visit just for a weekend. Jon absolutely loves every minute he spends in a National Park! Jon is looking forward to joining a local start-up, called Recurrent Automotive, in May. Recurrent uses data science to accelerate the adoption of used electric vehicles by providing a trustworthy diagnostic of the EVs battery health.